

Proper motions and dynamics of the Milky Way globular cluster system from *Gaia* DR2

Eugene Vasiliev^{1,2*}

¹*Institute of Astronomy, Madingley road, Cambridge, CB3 0HA, UK*

²*Lebedev Physical Institute, Leninsky prospekt 53, Moscow, 119991, Russia*

Accepted 2019 January 11. Received 2018 December 4; in original form 2018 August 6

ABSTRACT

We use *Gaia* Data Release 2 to determine the mean proper motions for 150 Milky Way globular clusters (almost the entire known population), with a typical uncertainty of 0.05 mas yr^{-1} limited mainly by systematic errors. Combining them with distance and line-of-sight velocity measurements from the literature, we analyze the distribution of globular clusters in the 6d phase space, using both position/velocity and action/angle coordinates. The population of clusters in the central 10 kpc has a mean rotational velocity reaching $50 - 80 \text{ km s}^{-1}$, and a nearly isotropic velocity dispersion $100 - 120 \text{ km s}^{-1}$, while in the outer galaxy the cluster orbits are strongly radially anisotropic. We confirm a concentration of clusters at high radial action in the outer region of the Galaxy. Finally, we explore a range of equilibrium distribution function-based models for the entire globular cluster system, and the information they provide about the potential of the Milky Way. The dynamics of clusters is best described by models with the circular velocity between 10 and 50 kpc staying in the range $210 - 240 \text{ km s}^{-1}$.

Key words: catalogues – proper motions – globular clusters: general – Galaxy: kinematics and dynamics

1 INTRODUCTION

With the second data release (DR2) of the *Gaia* mission in April 2018 (Brown et al. 2018), a new era in dynamical astronomy has begun. Astrometric data – parallaxes and proper motions (PM) – are now available for $> 10^9$ stars, with a typical parallax uncertainty ranging from 0.1 mas at the bright end to 1 mas for fainter stars down to magnitude $G = 21$, and a similar PM uncertainty in mas yr^{-1} . A few million stars also have measured line-of-sight velocities, mostly within heliocentric distance $1 - 3 \text{ kpc}$, thus providing a full six-dimensional phase-space view on the distribution and kinematics of stars in the Solar neighbourhood.

For more distant stars, the uncertainties in individual parallax and PM measurements are not negligible and translate into larger errors in the distance and the transverse velocity. However, mean PM of compact bound stellar systems such as globular clusters or satellite galaxies may still be computed with high precision by averaging over many stars belonging to each object. These data, together with the distances and line-of-sight velocities obtained by other methods, can be used to study the orbits of clusters and to put constraints on the total potential of the Milky Way.

Ground-based PM measurements are available for a large fraction of the Milky Way globular clusters ($60 - 120$ in various catalogues), but as will be shown later, their accuracy is inferior to the space-based ones, due to intrinsic difficulties in measuring stellar positions accurately in the presence of atmospheric aberrations. *Hubble* space telescope (*HST*) has been used to determine the PM of more than two dozen clusters (Sohn et al. 2018 and other studies). In both cases, the internal (relative) PM are more easily obtained than the absolute PM; they are suitable for membership filtering, but not for the determination of cluster orbits. To measure the absolute PM of a cluster, one needs to anchor the relative PM to some objects with known absolute PM – for instance, distant quasars or stars from the *Hipparcos* catalogue (Perryman et al. 1997); however, these objects are rare, and only a few may be present in each field of view. The first data release of *Gaia* contained a relatively small number of absolute astrometric measurements for stars previously observed by *Hipparcos*, and has been used to determine the mean PM of several closest globular clusters (Watkins & van der Marel 2017); however, with only a few stars per cluster, the uncertainties are large. On the other hand, *Gaia* DR2 provides the PM with much higher precision for a vastly larger number of stars over the entire sky

* E-mail: eugvas@lpi.ru

in the absolute reference frame, although not without systematic errors, which will be discussed further below.

Gaia collaboration (Helmi et al. 2018, hereafter H18) determined the mean PM for 75 galactic globular clusters – roughly a half of the known population listed in the Harris (1996, 2010) catalogue, mostly lying within a heliocentric distance of 15 kpc and having a sufficient number of bright stars with accurate astrometric measurements. However, this does not imply that the remaining ones are unsuitable for analysis. More recently (after the submission of this paper), Baumgardt et al. (2019) published independent measurements of mean PM for almost all Milky Way globular clusters based on *Gaia* DR2 data.

In this paper, we use the *Gaia* data to measure the mean PM for 150 globular clusters – twice larger number than provided by H18. One novel feature compared to the two other *Gaia*-based studies is the treatment of spatially correlated systematic errors, using the approach presented in a companion paper (Vasiliev 2018b). Section 2 presents this new catalogue and compares it with other existing measurements, both ground- and space-based. We then combine the PM with the distances and line-of-sight velocity measurements available in the literature, to obtain the full 6d phase-space distribution of globular clusters. In section 3, we analyze various trends in this distribution (e.g., velocity dispersions, anisotropy and rotation) in the position/velocity phase space. We also examine this distribution in the action/angle space, which makes easier the identification of various sub-populations with different kinematics, and also hints at possible selection biases. Then in Section 4 we model the population of globular clusters by an equilibrium distribution function (DF) in the action space. We determine the range of parameters of both the DF and the gravitational potential which are consistent with the observed dynamics. Section 5 summarizes our results. Technical details about our PM measurement procedure, remarks about individual clusters, and the table containing PM and other parameters, are deferred to the Appendix, while the supplementary material contains the plots of distribution of cluster members and field stars in the sky plane, PM space, and colour-magnitude diagrams for all 150 clusters.

2 PROPER MOTIONS

2.1 Data

We use the following selection criteria on the input sample:

- Select all stars with full astrometric data (position, parallax ϖ and PM μ_α, μ_δ) within a certain angular distance R_{\max} from the cluster centre. The distance is typically chosen to be several times larger than the half-light radius (a few arcminutes for most clusters), to ensure that a sufficient number of likely non-member stars are found in the region. These are needed for our mixture modelling approach: in the absence of a reliable field population, we would be forced to attribute each source to the cluster, even if its PM is grossly inconsistent with the mean value.

- Retain only sources with measured parallax $\varpi < 1/D + 3\epsilon_\varpi$, where D is the distance to the cluster, and ϵ_ϖ is the quoted parallax uncertainty. This removes most nearby stars which lie on the line of sight.

- Remove sources with `astrometric_excess_noise` parameter greater than 1, or with renormalized unit weight error exceeding 1.2 (this parameter is defined in Lindegren 2018). Larger values of these parameters indicate that the astrometric solution might be unreliable (in particular, the formal uncertainties might be underestimated), which happens mostly for unresolved binaries or faints sources in crowded fields (Lindegren et al. 2018).

- For all but a few clusters, we also eliminated stars with significant colour excess: `phot_bp_rp_excess_factor` $> 1.3 + 0.06 \text{ bp_rp}^2$, as suggested by the above paper. This mostly affects fainter stars with strong contamination by nearby brighter sources in denser central regions of clusters, and reduces the number of sources in each cluster by a factor between 2 and 10. *Gaia* DR2 does not have any special treatment for blended or contaminated sources (although such treatment should be implemented in future data releases, see Sections 2 and 3 in Pancino et al. 2017 for a thorough discussion), and their quoted PM uncertainties are also likely underestimated. Even though this cut dramatically reduces the number of available stars, it has only a minor effect on the precision of mean PM measurements (but should improve their reliability), because the omitted sources typically have large uncertainties anyway. However, we decided not to apply this cut in several clusters that would otherwise retain only a few stars: AM 1, Crater, Pal 3, Pal 4, Terzan 6.

We chose not to use the *Gaia* BP and RP colour measurements in the fitting procedure. The current stellar population models, although sophisticated, still do not describe well the population of blue horizontal branch stars. Likewise, the ages, metallicities and extinction coefficients are not well known for some of the clusters, and sometimes the values quoted in the catalogue clearly do not match the reddening-corrected colour-magnitude diagram (CMD) seen in the *Gaia* data. These uncertainties mean that filtering the CMD based on the proximity of observed magnitudes to the theoretical isochrone curve would leave out some, or sometimes even most sources. Instead, we use the *Gaia* colours as an independent consistency check, inspecting the CMD of stars classified as likely cluster members based on their PM and position. In most cases these stars align well with the theoretical isochrone curve, or at least clearly stand out from the field population. Exceptions mostly occur in heavily extincted clusters, where the colour information would not help anyway.

2.2 Method

The distribution of sources in the PM space¹ $\{\mu_\alpha, \mu_\delta\}$ typically has a well-defined clump corresponding to the cluster members, and a broader distribution of field stars. Quite often, though, there is no clear separation between the two, and we employ a probabilistic Gaussian mixture model to select member stars and to infer the intrinsic (error-deconvolved) parameters of the distributions of both member and non-member stars. In doing so, we use a spatially-dependent prior for the membership probability. A detailed description of the procedure is presented in Appendix A.

¹ Throughout the paper, we denote $\mu_\alpha \equiv d\alpha/dt \cos \delta$.

Some of the most massive or nearby clusters contain tens of thousands stars in the *Gaia* catalogue, allowing one to measure not only the average PM for the entire cluster, but also, to some degree, its internal kinematics. The radial profiles of sky-plane rotation have been measured for some clusters by [Bianchini et al. \(2018\)](#), and the PM dispersion profiles – by [Baumgardt et al. \(2019\)](#). In the present study, we use a simplified description of the internal kinematics, ignoring the rotation and assuming that the PM dispersion is isotropic and follows a particular radial profile with an amplitude freely adjusted during the fit. The companion paper ([Vasiliev 2018b](#)) uses the same membership determination procedure, but a more flexible description of the internal kinematics, to measure the PM dispersion and rotation profiles, taking into account the systematic errors.

The fitting procedure produces the estimate of the mean PM $\{\bar{\mu}_\alpha, \bar{\mu}_\delta\}$ and its associated uncertainty covariance matrix, which may equivalently be represented by two standard deviations $\{\epsilon_{\bar{\mu}_\alpha}, \epsilon_{\bar{\mu}_\delta}\}$ and the correlation coefficient $r_{\bar{\mu}_\alpha \bar{\mu}_\delta}$. In doing so, we may consider only the statistical uncertainties, which decrease from $\text{few} \times 10^{-1}$ to $\text{few} \times 10^{-3} \text{ mas yr}^{-1}$ as the number of member stars increases (Figure 1, gray symbols). However, for the majority of clusters, the dominant source of uncertainty are the spatially correlated systematic errors. Our final uncertainty estimates take these systematic errors into account (coloured symbols), as sketched in [Lindegren \(2018\)](#) and explained in more detail in the companion paper and in the [Appendix](#).

2.3 Results

Table C1 lists the derived PM, together with several other parameters, for all 150 clusters in this study. We were not able to measure it only for a few clusters from the [Harris \(2010\)](#) catalogue – either very distant ones with less than a few stars on the red giant branch detectable by *Gaia* (Ko 1, Ko 2 and AM 4), or heavily extinguished clusters in the disc plane that were discovered in infrared surveys (2MASS-GC01, 2MASS-GC02, GLIMPSE1, GLIMPSE2, Liller 1 and UKS1). We added two more clusters not originally present in the Harris catalogue: Crater (Laevens 1), discovered by [Belokurov et al. \(2014\)](#) and [Laevens et al. \(2014\)](#), and FSR 1716, recently confirmed as an old globular cluster by [Minniti et al. \(2017\)](#).

We compared our PM with several existing catalogues (Figure 2). Half of our sample has already been analyzed by the *Gaia* collaboration, using somewhat different approach for membership determination ([H18](#)). For the vast majority of these clusters, our measurements agree with the ones from that paper to better than 0.05 mas yr^{-1} . The two clusters with the largest difference ($\sim 0.15 - 0.25 \text{ mas yr}^{-1}$) are NGC 6626 (M 28) and NGC 6266 (M 62), which are both located in rather dense regions on the sky, and the coordinates of cluster centres used by ([H18](#)) are offset by some 1.5 arcmin from the true values. A visual inspection of PM diagrams confirms the validity of mean values obtained by our Gaussian mixture procedure.

[Baumgardt et al. \(2019\)](#) independently measured PM for all clusters in our catalogue, also using *Gaia* data but a different approach for membership determination. Our measurements agree to better than 0.05 mas yr^{-1} , except for a few clusters: FSR 1735 (0.75 mas yr^{-1}), Ton 2 (0.25),

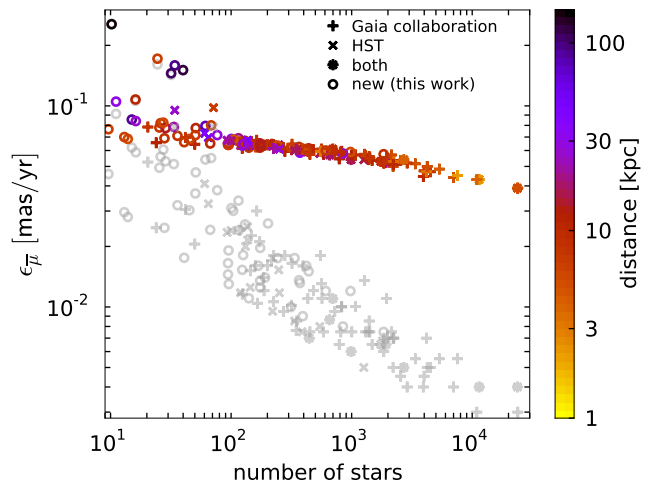


Figure 1. Uncertainty of mean PM (average of $\epsilon_{\bar{\mu}_\alpha}, \epsilon_{\bar{\mu}_\delta}$) as a function of the number of cluster members N_* remaining after applying all quality filters. Gray symbols show the statistical uncertainty alone, which broadly follows the $N^{-1/2}$ trend expected for Poisson noise. Coloured symbols show the combined statistical and systematic uncertainty, which is dominated by the latter for nearly all clusters with more than a few dozen members. The systematic uncertainty is $\sim 0.07 \text{ mas yr}^{-1}$ for very compact clusters and decreases with the angular size of an object, hence is lower for the closest and richest clusters. Different symbols denote the new clusters in this work (circles) or clusters with previously determined PM (from [H18](#), *HST*, or both). Points are coloured according to the distance to the clusters as given in the Harris catalogue.

Terzan 1 (0.2), AM 1 (0.4), Pal 2 (0.35), Eridanus (0.3). The first three are located in heavily extinguished regions close to the disc plane, and the last three are fairly distant clusters with only faint stars. Overall, the agreement between the three catalogues based on *Gaia* data is excellent.

Absolute PM have been obtained with *HST* for 27 clusters in our sample: 20 distant clusters in [Sohn et al. \(2018\)](#), NGC 362 in [Libralato et al. \(2018b\)](#), NGC 5139 (ω Cen) in [Libralato et al. \(2018a\)](#), NGC 6397 in [Milone et al. \(2006\)](#), NGC 6652 in [Sohn et al. \(2015\)](#), NGC 6681 (M 70) in [Massari et al. \(2013\)](#), NGC 6838 (M 71) in [Cadelano et al. \(2017\)](#), and Terzan 5 in [Massari et al. \(2015\)](#). Of these, only Terzan 5 differs from our value by about 2 mas yr^{-1} in μ_α , and the remaining measurements agree to better than 1 mas yr^{-1} . Terzan 5 lies in a dense field within the Galactic bulge, and in order to establish the absolute PM, [Massari et al. \(2015\)](#) used bulge stars as a reference, not distant quasars as typically done for other *HST* clusters, which may explain the offset. The good agreement between two space-based missions is encouraging, and lends further credibility to the *Gaia* results.

On the other hand, a comparison with ground-based PM measurements demonstrates that there are often significant differences, up to a few mas yr^{-1} . The catalogues of [Casetti-Dinescu et al. \(2007, 2010, 2013\)](#) and [Chemel et al. \(2018\)](#) still demonstrate a rather good correlation with the *Gaia* measurements (second and third columns in Figure 2), and an independent Pal 5 measurement by [Fritz & Kallivayalil \(2015\)](#) is only $\sim 0.6 \text{ mas yr}^{-1}$ off. However, the catalogue of [Kharchenko et al. \(2013\)](#) bears almost no resemblance to

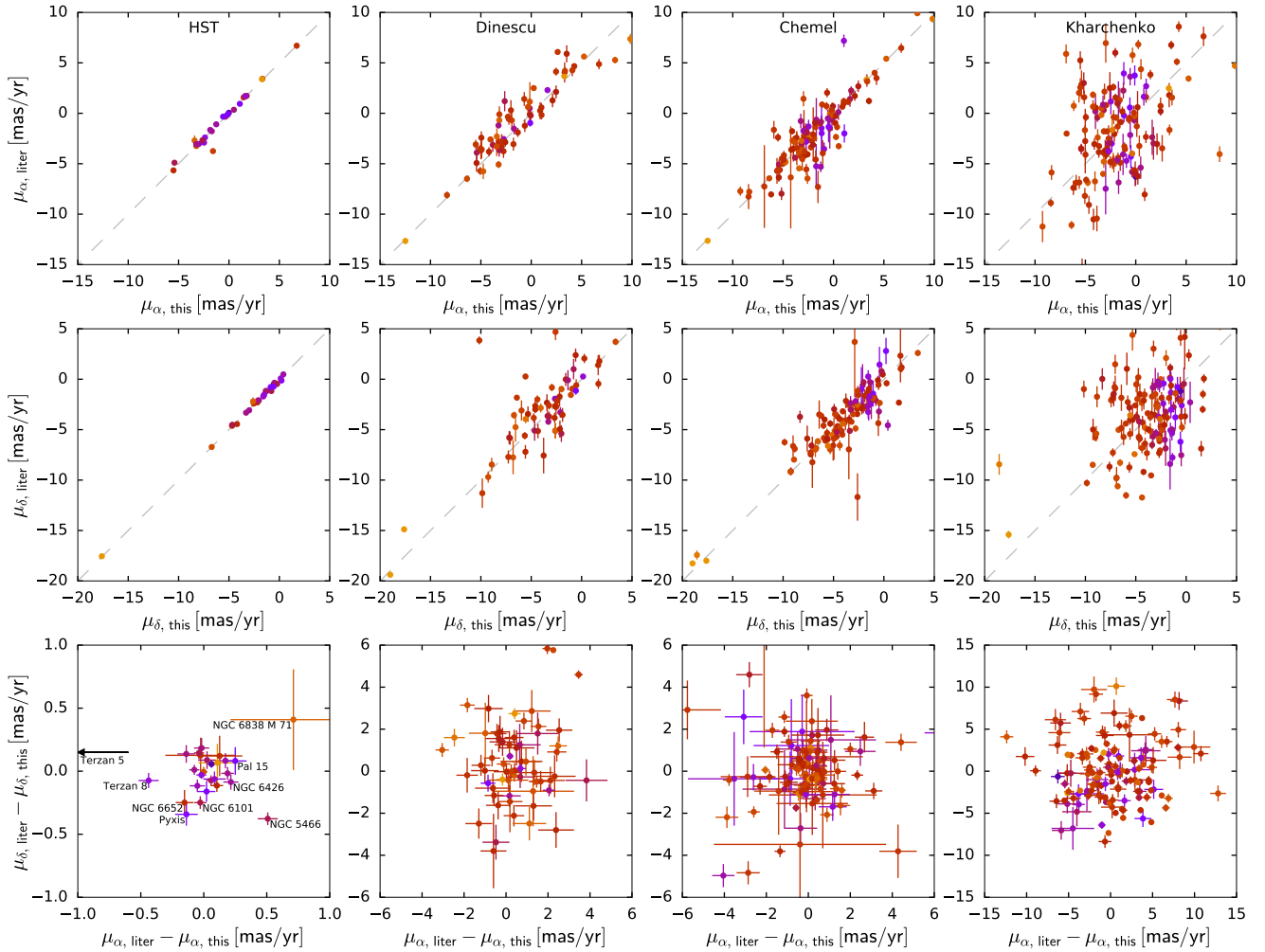


Figure 2. Comparison of PM measurements between different catalogues and this work. First column: *HST* (several studies, primarily [Sohn et al. 2018](#)). Second column: [Dinescu et al. \(1999\)](#) and several later papers. Third column: [Chemel et al. \(2018\)](#). Last column: [Kharchenko et al. \(2013\)](#). Top row: comparison between μ_{α} from the literature and from this work; middle row: same for μ_{δ} ; bottom row: difference between the literature measurements and this work (two PM components plotted against each other, note the different scale for each column). Colours denote the distance to the clusters (same colour scheme as in the previous plot).

the space-based measurements, with differences exceeding 5 mas yr^{-1} (last column). Unfortunately, it is the default source of PM values listed in SIMBAD.

We performed several internal validation procedures, comparing the PM determined from different subsets of stars, or under different assumptions about the internal structure and kinematics (such as more flexible models from the companion paper). For instance, we removed stars with magnitudes $G > 20$ as in [H18](#), or skipped the cut in `phot_bp_rp_excess_factor`, or changed the maximum angular distance from the cluster centre. The results were robust to these changes, with differences typically far smaller than the quoted uncertainty. We also verified that the mean PM values obtained with and without account for systematic errors are compatible (of course, the uncertainties are far smaller in the latter case, but they do not tell the whole story). We therefore believe that the mean cluster PM provided in this study are not only precise (corresponding to transverse velocity errors less than 10 km s^{-1} for most clusters except a few distant ones), but also accurate insofar as the *Gaia* data themselves.

3 KINEMATICS OF THE GLOBULAR CLUSTER SYSTEM

3.1 Velocity distribution

Having precise PM for most of Milky Way globular clusters, we are ready to analyze their distribution in the full 6d phase space, combining the *Gaia* PM with the distances and line-of-sight velocities from the literature. The velocities are taken from the catalogue of [Baumgardt et al. \(2019\)](#), and have typical uncertainties of only $1 - 2 \text{ km s}^{-1}$. We use the distances from the [Harris \(2010\)](#) catalogue, and assume an error of 0.1 in distance modulus, corresponding to a relative error of 0.046 in the distance. This is probably a rather optimistic choice: for some clusters, the variation in several independent distance estimates from the literature could exceed 10%. Even so, the distance appears to be the largest source of uncertainty for the majority of clusters, except a few outermost ones with large PM errors. Unfortunately, *Gaia* parallaxes currently cannot be used to improve the distance uncertainty, due to a substantial and spatially varying systematic offset $\epsilon_{\varpi} \sim -0.03 \pm 0.05 \text{ mas}$ ([Lindgren](#)

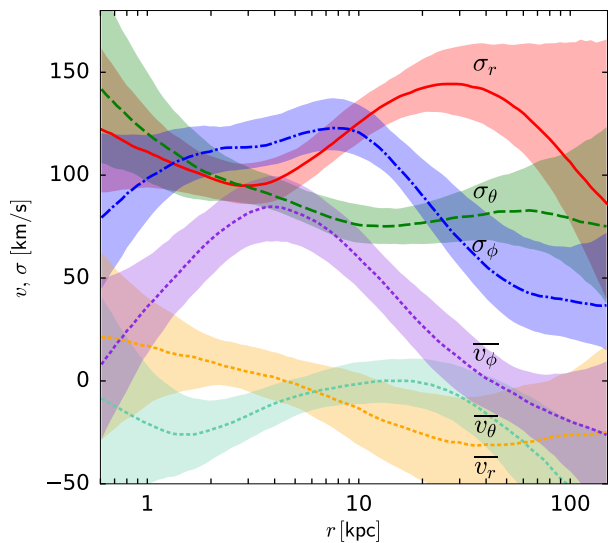


Figure 3. Kinematics of the Milky Way globular cluster system. Plotted are the velocity dispersions σ in spherical coordinates and the mean velocities \bar{v} as functions of spherical radius, with 68% uncertainty bands shaded in respective colour. The significantly non-zero azimuthal velocity \bar{v}_ϕ indicates the overall prograde rotation of the ensemble of clusters, while \bar{v}_r and \bar{v}_θ are consistent with zero, as expected in a dynamical equilibrium. At large radii, the distribution of clusters in velocity space becomes radially anisotropic (σ_r is significantly higher than the other two components of velocity dispersion). Clusters associated with the Sgr galaxy are excluded (they would have inflated σ_θ and shifted \bar{v}_θ around $r = 30$ kpc).

et al. 2018, H18). As most clusters are located at distances $\gtrsim 5$ kpc, corresponding to the true parallax $\lesssim 0.2$ mas, this unknown systematic offset has a very substantial impact on the measurement. Only in some special cases, when a sufficient number of suitable background reference objects are available, this offset could be measured and subtracted (e.g., Chen et al. 2018). By the end of the mission, the parallax and PM uncertainties are expected to reach 1% level for clusters within 15 kpc (Pancino et al. 2017).

The uncertainties in the data are propagated to the subsequent models as follows: for each cluster, we draw $N_{\text{samples}} = 1000$ Monte Carlo samples from the distribution of errors in PM (taking into account their covariance), distance and line-of-sight velocity. We then convert these samples to Galactic coordinates, assuming the solar position within the Galaxy at $R_0 = 8.2 \pm 0.1$ kpc, $z_0 = 25 \pm 5$ pc, and the solar velocity vector $\{v_R, v_\phi, v_z\} = \{-10 \pm 1, 248 \pm 3, 7 \pm 1\}$ km s $^{-1}$ (Bland-Hawthorn & Gerhard 2016). The distribution of Monte Carlo samples for each cluster is often significantly elongated in position/velocity space, and sometimes does not resemble a simple Gaussian at all. By using the full ensemble of samples for each cluster, rather than just their covariance matrix, we ensure a correct convolution with observational errors throughout our modelling procedure.

We excluded some clusters from the subsequent analysis for various reasons. The few clusters for which we were unable to determine the mean PM could be included into the analysis by assigning them a large formal uncertainty (as in

Eadie et al. 2017 or Binney & Wong 2017), however, they add very little information, and omitting them makes no difference to the modelling results. A few clusters listed below are associated with the Sagittarius stream, and hence do not constitute independent samples; we omitted them from the computation of velocity dispersion profiles and the dynamical modelling of Section 4, but kept them in the phase-space plots.

To measure the density and 1d velocity distributions, and the radial profiles of mean velocity and its dispersion, we use a non-parametric penalized spline fitting approach, described in Appendix B, which produces smooth estimates of these quantities and associated confidence intervals.

Figure 3 shows the radial profiles of velocity dispersions and mean velocities of the entire population of clusters excluding the ones associated with the Sagittarius stream (see below). Several trends are apparent:

- Clusters within $r \lesssim 10$ kpc move mostly on prograde orbits, with mean velocity reaching $70 - 80$ km s $^{-1}$ at $4 - 7$ kpc.
- The velocity dispersion tensor is close to isotropic with $\sigma \simeq 100$ km s $^{-1}$ in the inner Galaxy ($r \lesssim 10$ kpc), and becomes radially anisotropic further out. This follows similar patterns observed in the population of halo stars (e.g., Deason et al. 2012), and will be discussed in more detail in the next section.
- Mean radial and polar velocities are consistent with zero within uncertainties, as expected in a steady state. However, if we include the Sagittarius stream clusters, the mean polar velocity becomes somewhat negative around $\sim 20 - 30$ kpc, and its dispersion is increased.

A more detailed illustration is presented in Figure 4, which shows the distribution of clusters in 2d spaces of radius and velocity (separately for each velocity component), coloured by metallicity. It highlights various features in the cluster kinematics, which have been known previously:

- Metal-rich clusters (so-called disc population, Zinn 1985) are predominantly found inside 10 kpc and on preferentially corotating orbits, with typical value of azimuthal velocity $v_\phi \gtrsim 100$ km s $^{-1}$. These are responsible for the peak in \bar{v}_ϕ in the inner Galaxy, seen in the previous plot.
- There are several clusters on significantly retrograde orbits (e.g., NGC 3201 and NGC 6101), which may have been accreted from an infalling satellite galaxy. The now available accurate kinematic information complements the age and metallicity measurements and will assist in distinguishing accreted clusters from those formed in situ (e.g., Forbes & Bridges 2010; Kruijssen et al. 2018).
- Some kinematic structures are readily identified, such as the four clusters in the core of the Sagittarius stream, which all have similar radii (~ 20 kpc) and high $|v_\theta| \gtrsim 250$ km s $^{-1}$: NGC 6715 (M 54), Terzan 7, Terzan 8 and Arp 2. However, this is not at all apparent for two other clusters that are on very similar orbits (Pal 12 and Whiting 1, with the PM of the latter first measured in this study); to see their relation to the stream, one would need to compute the orbits or the integrals of motion. This requires the knowledge of the potential.

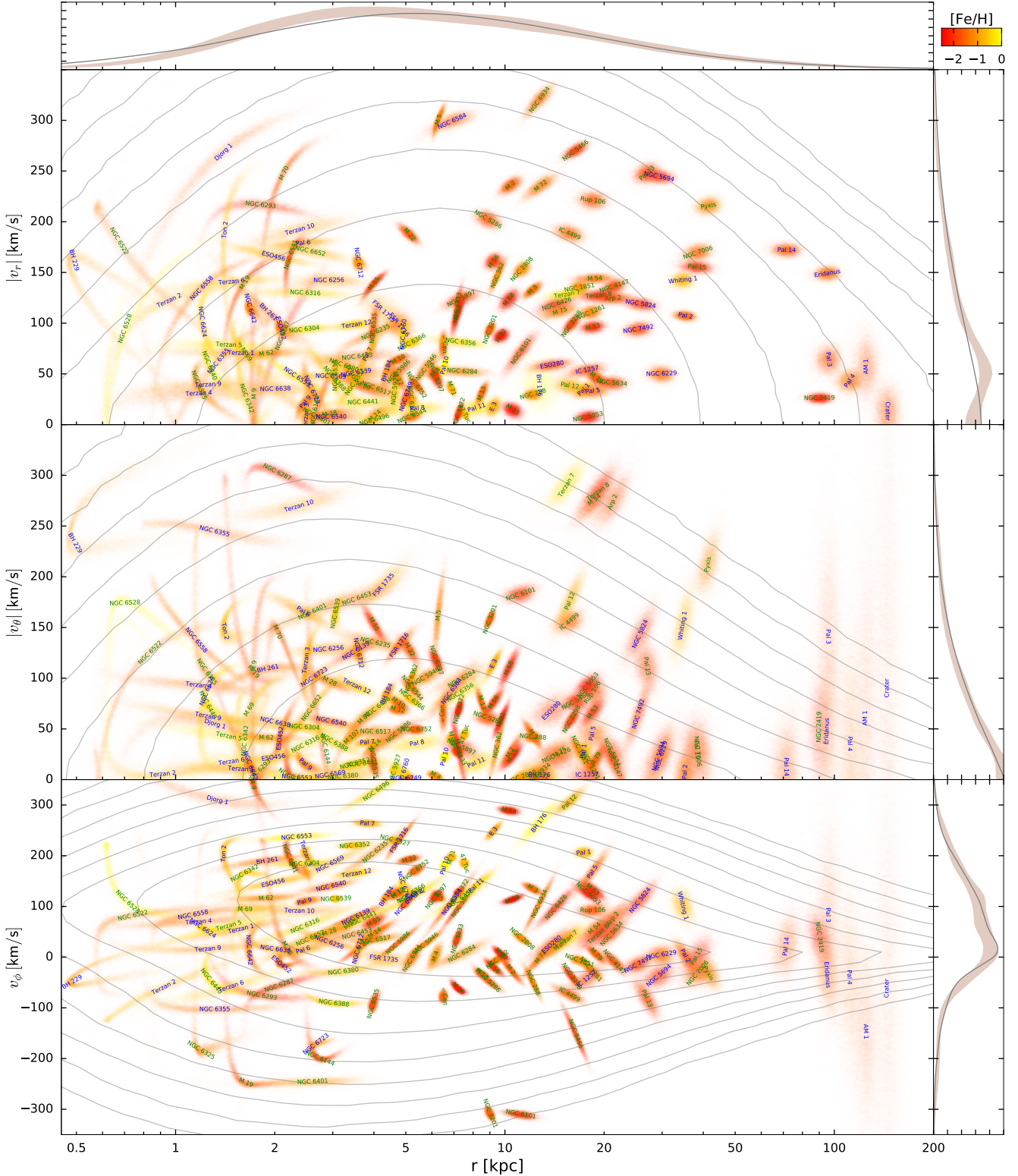


Figure 4. The onion diagram showing the distribution of globular clusters in galactocentric radius and galactocentric velocity in spherical coordinates (one panel per velocity component). Each cluster is shown as a cloud of Monte Carlo samples representing the uncertainties in its position and velocity, coloured according to the metallicity as quoted in the [Harris \(2010\)](#) catalogue. Clusters with previously existing space-based PM measurements (from the *Gaia* collaboration or from various *HST* studies) have their names shown in green; the new measurements in this paper – in blue. Gray contour lines show the projection of the model DF (Section 4.4) into the coordinate/velocity space, averaged over many acceptable models in the MCMC chain, all computed in the [McMillan \(2017\)](#) potential. Contours are spaced logarithmically, each successive line corresponding to a twice lower probability than the previous one. Side panels show the 1d projections of the distributions: shaded bands – actual data with uncertainties, solid gray – model.

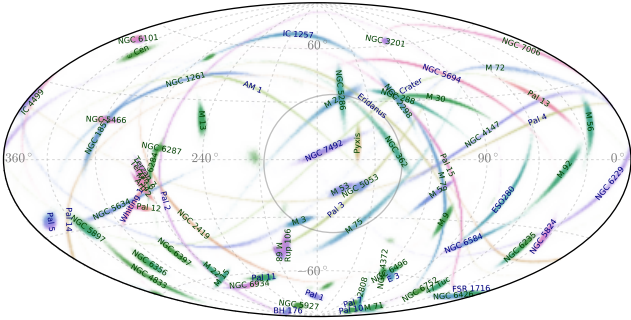


Figure 6. Distribution of orbital poles (directions of angular momentum) in the galactocentric coordinates. Shown are clusters from the outer galaxy, with $R_{\text{circ}} \geq 5$ kpc, coloured by energy as in the bottom panel of the previous figure. The gray circle near the centre of the image denotes the location of the “Vast Plane of Satellites” (VPOS) from Pawlowski et al. (2012), same as in Figure 3 of Fritz et al. (2018). There is no obvious clumping of orbital poles in this direction, although the orbital plane of the Sagittarius stream and associated clusters is clearly seen some 90° to the left of it, coloured in pink.

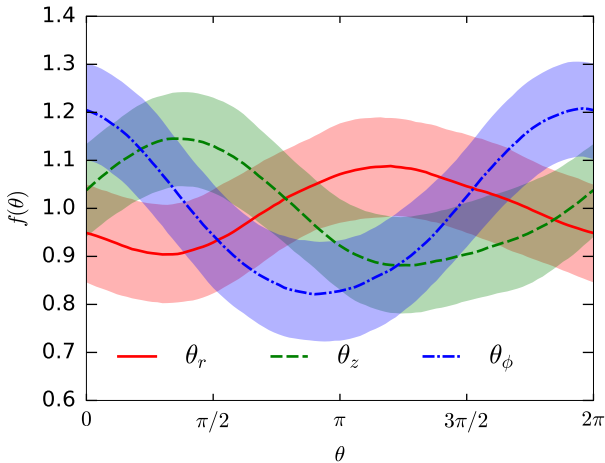


Figure 7. Distribution of observed globular clusters in phase angles (canonically conjugate variables to the actions), evaluated in the McMillan (2017) potential. Only the distribution in θ_ϕ is significantly non-uniform, possibly indicating incompleteness of the catalogue at the more distant side of the Galaxy (behind the bulge/disc).

3.2 Action-angle space distribution

To get further insight into the observed distribution of globular clusters, we convert their positions and velocities into actions and angles. For this, one needs to specify the potential, and we use the best-fit model of McMillan (2017) as our default choice. The actions and angles are estimated using the Stäckel fudge approach (Binney 2012, see also Sanders & Binney 2016 for an overview of action computation methods), as implemented in the AGAMA galaxy modelling framework (Vasiliev 2019).

Figure 5 illustrates the distribution of clusters in the action space: two coordinates on the plot specify the relative weight of each of the three actions, and the third dimension

– the total energy E , expressed equivalently as the radius of a circular orbit $R_{\text{circ}}(E)$ – is shown by colour. To avoid clutter, we split the entire population into two roughly equal halves, with $R_{\text{circ}} = 5$ kpc as the boundary (a few clusters appear in both panels because of uncertainties in their energy). This plot shows various sub-populations more clearly than the velocity-space diagram. For instance, all six Sagittarius stream clusters are grouped together in the upper half of the right panel (pink colours), indicating that they are on nearly polar orbits. A few more pairs of clusters are on similar orbits: NGC 7078 (M 15) and NGC 6656 (M 22), NGC 6838 (M 71) and Pal 10, and with a stretch of imagination, NGC 5024 (M 53) and NGC 5053. The latter pair happens to be very close in physical space at present, suggesting a possible link between them (Chun et al. 2010); their metallicities, PM and orbital planes are also similar, but the line-of-sight velocities differ by 100 km s^{-1} .

Another interesting feature is the clumping of several clusters in the bottom part of the right panel, indicating that they have rather eccentric orbits with large radial actions. This population was identified by Myeong et al. (2018) and associated with a similar radially-biased population in the stellar halo. The eight clusters listed in that paper are NGC 1851, NGC 1904 (M 79), NGC 2298, NGC 2808, NGC 5286, NGC 6779 (M 56), NGC 6864 (M 75) and NGC 7089 (M 2). Possible other candidates in the same region with newly measured PM include NGC 6584 and IC 1257, although no two of the entire sample of high- J_r clusters appear to be on similar orbits in physical space.

Figure 6 shows the distribution of orbital poles (instantaneous directions of angular momenta) for the outer galaxy clusters; the coordinates are the same as in Figure 3 of Fritz et al. (2018). The clumping of Sagittarius clusters is obvious in the left side of this plot, but the orbital planes of clusters from Myeong et al. (2018) are scattered across the sky. Some of them and a few other clusters (e.g., the outermost ones: Pyxis, Eridanus, AM 1, Crater, Pal 3, Pal 4) lie close to the direction of the “Vast Plane of Satellites” (Pawlowski et al. 2012), which was recently confirmed to contain a large fraction of Milky Way satellite galaxies (Fritz et al. 2018); however, most globular clusters do not appear to be associated with this structure. On the other hand, the angular momentum vector is not an integral of motion, as the orbital planes precess and nutate in a non-spherical potential, thus a single progenitor cannot be excluded even for clusters whose orbital planes do not align at present. A more detailed classification of the cluster population, its relation to the stellar halo and to the accretion history of the Milky Way would need to take into account chemical composition and star formation history (e.g., Kruijssen et al. 2018), in addition to the now available kinematic information.

The use of actions, as opposed to any other integrals of motion, also allows one to examine the distribution of clusters in phase angles, which are canonically conjugate variables to actions. We expect a uniform distribution in angles for a well phase-mixed population. Figure 7 shows the distribution of observed clusters (taking into account the errors) in three phase angles, computed using an amount of smoothing calibrated by cross-validation (suppressing likely insignificant fluctuations), as explained in Appendix B. The phase angle of azimuthal motion θ_ϕ , which describes the location with respect to the solar position, is distributed

significantly non-uniformly: the higher probability of finding clusters around 0 or 2π suggests that the catalogue is deficient in clusters located at the other side of the Galaxy, which may have escaped detection because of dust obscuration. A similar asymmetry is observed in the distribution of azimuthal angle ϕ itself – see Figure 7 in Binney & Wong (2017), who propose that it could arise either from missing clusters hidden by dust, or from systematic underestimation of cluster distances (which would place them preferentially on the near side of the Galaxy). The other two phase angles are consistent with being uniformly distributed.

4 DYNAMICAL MODELLING

4.1 Method

We now explore the dynamical properties of the globular cluster system, and the information it provides about the Milky Way potential, following the standard assumption that this is a steady-state equilibrium configuration. The population of clusters is described by a certain distribution function (DF) $f(\mathbf{w})$, which specifies the probability of observing a particular combination of position and velocity $\mathbf{w} \equiv \{\mathbf{x}, \mathbf{v}\}$ for any cluster. According to Jeans’ theorem, in a steady state the DF must be a function of integrals of motion $\mathbf{I}(\mathbf{w}; \Phi)$, which themselves depend on the potential Φ . The best-fit parameters of the DF, and possibly the potential, are found by maximizing the likelihood of drawing the observed positions and velocities of clusters from this DF – the same approach was used in Binney & Wong (2017) and Posti & Helmi (2019).

The log-likelihood of the model is given by the sum of log-likelihoods for each cluster, convolved with their respective error distributions:

$$\ln \mathcal{L} = \sum_{i=1}^{N_{\text{clusters}}} \ln \frac{S(\mathbf{w}_i) \int d\mathbf{w}' E(\mathbf{w}_i | \mathbf{w}') f(\mathbf{I}[\mathbf{w}'; \Phi])}{\int d\mathbf{w}' S(\mathbf{w}') f(\mathbf{I}[\mathbf{w}'; \Phi])}. \quad (1)$$

Here $E(\mathbf{w}_i | \mathbf{w}')$ is the probability of measuring the phase-space coordinates of i -th cluster as \mathbf{w}_i given the true values \mathbf{w}' . This is not the same as the multivariate normal distribution for the observable quantities \mathbf{u} (sky coordinates α, δ , heliocentric distance D , PM μ_α, μ_δ , and line-of-sight velocity v_{los}), but includes a Jacobian factor for transformation from \mathbf{u} to \mathbf{w} , equal to $D^4 \cos \delta$. However, for relatively small adopted distance uncertainty, its role is negligible (apart from shifting the total likelihood by an unimportant constant).

$S(\mathbf{w})$ is the selection function, which specifies the probability of observing a cluster at a given position (and possibly velocity) in the survey. For clusters, this function is close to unity, except in some regions in the central Galaxy or beyond, where the strong extinction along the line of sight might have prevented their discovery or observation, or in the very distant outer regions, where the clusters are too faint. Empirically, we could not locate 6% (9 out of 157) clusters from the Harris (2010) catalogue in the Gaia data, which suggests that the incompleteness of our sample with respect to known cluster population is rather minor. However, the non-uniformity of cluster distribution in phase angles, identified in the previous section, hints at a possible existence of yet undiscovered clusters. Despite this, in the remaining

analysis we assume $S = 1$. Binney & Wong (2017) found that inclusion of an extinction-dependent selection function had little effect on their results.

The integral in the numerator of Equation 1 is the convolution of the DF with the error distribution for each cluster. We replace this integral by a sum over the Monte Carlo samples $\mathbf{w}'_{i,k}$, $k = 1..N_{\text{samples}}$, defined in the previous section. Note that this sum is inside the argument of the logarithm, so that even if some of the samples lie in a physically inaccessible region (e.g., have positive energy) and hence have zero probability, this only moderately affects the likelihood of the given cluster, provided that there are enough samples for which $f(\mathbf{w}'_{i,k})$ has a non-negligible value. Of course, the set of Monte Carlo samples must remain the same for all models, to compensate the Poisson fluctuations in the likelihood (McMillan & Binney 2013).

The integral in the denominator is the overall normalization factor, identical for all clusters. In the absence of a non-trivial selection function, it can be computed directly in the \mathbf{I} space, and gives the total number of clusters.

In addition, the posterior likelihood of a model with the given parameters of the DF and the potential may have a contribution from a prior probability of these parameters. In practice, we specify non-trivial priors for a couple of parameters, and simply restrict other parameters to lie in some finite intervals, to ensure that the prior probability is normalizable. For dimensional parameters such as scale radius, we adopt uninformative priors in their logarithms.

4.2 Ingredients

Similarly to Binney & Wong (2017) and Posti & Helmi (2019), we express the DF as a function of actions: the radial action J_r , the vertical action J_z , and the azimuthal action J_ϕ , equivalent to the z -component of angular momentum if the potential is axisymmetric. The Stäckel fudge in the current implementation only works for oblate axisymmetric potentials, hence we have to neglect the dynamical effect of the bar and possibly other non-axisymmetric features in the inner Galaxy, and restrict our halo shape to be spherical or oblate. For this reason, we do not expect the model to offer an accurate description of the dynamics of clusters in the innermost few kpc.

We assume that the entire population of globular clusters is described by a single DF, i.e., do not make any distinction between metal-poor halo and metal-rich disk populations. It is possible to generalize this approach by considering a mixture of two DFs and attribute each cluster to either of them probabilistically, just as we did to distinguish cluster members from field stars in the PM space. This would add a few more free parameters to the model without changing the overall procedure. However, our choice for the functional form of the single DF is already quite flexible, and it can simultaneously describe both populations reasonably well. It is similar to the double-power-law DF families used by Posti et al. (2015), Binney & Wong (2017), or Williams & Evans (2015):

$$f(\mathbf{J}) = \frac{M}{(2\pi J_0)^3} \left[1 + \left(\frac{J_0}{h(\mathbf{J})} \right)^\eta \right]^{\Gamma/\eta} \left[1 + \left(\frac{g(\mathbf{J})}{J_0} \right)^\eta \right]^{-B/\eta} \times \left(1 + \tanh \frac{\varkappa J_\phi}{J_r + J_z + |J_\phi|} \right). \quad (2)$$

Here

$$g(\mathbf{J}) \equiv g_r J_r + g_z J_z + (3 - g_r - g_z) |J_\phi|,$$

$$h(\mathbf{J}) \equiv h_r J_r + h_z J_z + (3 - h_r - h_z) |J_\phi|$$

are linear combinations of actions, with dimensionless coefficients controlling the spatial flattening and velocity anisotropy of the model in the outer region (above the break action J_0) and the inner region (below J_0), respectively. The power-law indices B and Γ control the outer and inner slopes of the density profile (although the relation between these the slopes of the DF and the density also depends on the potential). The parameter η determines the steepness of the transition between the two regimes. The rotation is introduced by the parameter \varkappa in a way that is roughly constant across all energies, since we normalize J_ϕ by the sum of all three actions. This is different from the convention used, e.g., in Binney (2014), Binney & Wong (2017) or Posti & Helmi (2019), which had a non-rotating core because J_ϕ in the argument of \tanh was normalized by a fixed constant. Overall, there are 9 free parameters in the DF (the total mass is fixed by the normalization constraint), which are restricted to physically acceptable ranges ($B > 3$, $0 < \Gamma < 3$, $0.5 \leq \eta \leq 2$, and positive coefficients in the linear combinations of actions).

The DF determines both the density profile and the velocity distribution of the tracer population of clusters. Of course, if the functional form of the DF and its parameters are adequate, the resulting density profile would match the actual spatial distribution of clusters, but we do not fit for it independently.

For the potential, we use the following three components: a central bulge with a truncated power-law profile, an exponential disc, and a rather flexible functional form for the halo density profile. The bulge profile is identical to that of McMillan (2017), and for simplicity, we replace four separate disc components from that study by a single exponential disc with a scale radius 3 kpc and scale height 0.3 kpc. The rotation curve produced by such a disc is very similar to the combination of four separate ones. The halo density profile follows the Zhao (1996) $\alpha\beta\gamma$ model:

$$\rho(r) = \rho_h \left(\frac{r}{r_h}\right)^{-\gamma} \left[1 + \left(\frac{r}{r_h}\right)^\alpha\right]^{(\gamma-\beta)/\alpha}. \quad (3)$$

The case $\alpha = 1, \beta = 3, \gamma = 1$ corresponds to the NFW profile, often used in other studies. However, we wish to avoid possible biases resulting from a restricted functional form of the halo potential, hence our model is very flexible – the inner density slope is controlled by γ , the outer by β , and α determines the steepness of transition between two asymptotic regimes. We experimented with non-spherical (oblate) shapes of the halo, but the fit always preferred the axis ratio close to 1, hence we assume the halo to be spherical. Overall, the potential has seven free parameters: the density normalization ρ_h and scale radius r_h of the halo, its three dimensionless slope parameters, and masses of the bulge and the disc. We allow the latter two to vary in a rather limited range, inspired by the best-fit potential suggested in McMillan (2017): $M_{\text{bulge}} = 9 \times 10^9 M_\odot$, $M_{\text{disc}} = 5.5 \times 10^{10} M_\odot$, both with relative uncertainty of 10%. The distribution of posterior values closely follows the prior, but the added flexibility allows us to propagate the uncertainty into the halo component. In addition, we put a

prior on the amplitude of circular velocity at the solar radius: $v_{\text{circ}}(R_0) = 235 \pm 10 \text{ km s}^{-1}$. This value is consistent with both the best-fit potential of McMillan (2017) and the observed total azimuthal solar velocity of $248 \pm 3 \text{ km s}^{-1}$ after subtracting the peculiar motion of $11 \pm 2 \text{ km s}^{-1}$ (Bland-Hawthorn & Gerhard 2016). We neglect the contribution of globular clusters to the total mass of the Galaxy.

4.3 Monte Carlo simulations

We explore the parameter space with the Monte Carlo Markov Chain (MCMC) method, implemented in the `emcee` package (Foreman-Mackey et al. 2013). We run 50 walkers for several thousand steps, monitoring the convergence of the posterior distribution, and use the median, 68% and 95% percentiles to display the results and their 1σ and 2σ confidence intervals.

We first run the fitting procedure, fixing the parameters of the potential to the values of McMillan (2017) best-fit model, and only varying the DF parameters. The resulting models successfully reproduce the cluster density profile and principal features in their velocity distribution (Figures 8 and 9, discussed in the next section). As it turns out, the range of acceptable DF parameters is rather insensitive to whether we vary the potential or not, so we discuss the properties of the DF later, after describing the entire simulation suite.

We then tested the ability of our machinery to recover the gravitational potential, if we let it free. For this purpose, we took one of the DFs from the MCMC chain, and created two types of mock datasets by drawing 150 samples from the DF in the known potential. In the first case, we use the measured positions of the observed clusters \mathbf{x}_i and randomly assign the velocities from the conditional velocity distribution $f(\mathbf{x} = \mathbf{x}_i, \mathbf{v})$. By using the measured positions, we test the possible biases arising from a mismatch between the actual density profile and the one generated by the DF. In the other case, we draw both \mathbf{x} and \mathbf{v} from the DF. We then converted the position and velocity of each cluster to the observable coordinates (sky position, distance, PM and line-of-sight velocity) and added a normally distributed random error to these values, drawn from the actual error estimates for each cluster. These mock datasets were then analyzed by the same pipeline, but this time the parameters of the potential are also allowed to vary. By repeating this experiment several times with different choices of DF, we found that the potential is well recovered, with a typical uncertainty on the rotation curve in the range $15 - 25 \text{ km s}^{-1}$ at large radii. The median circular velocity drops somewhat faster with radius at large distances than the true one, but the 1σ confidence interval encloses the true curve.

Finally, we proceed with modelling the original dataset with both the DF and potential parameters varied in the fitting process. The posterior distributions do not show any significant correlation between the DF and potential parameters, and only a few parameters in each of these two groups are substantially interdependent (e.g., the outer slope B of the DF and its scale action J_0). Several parameters are not well constrained, such as the outer slope of the halo density profile β and the steepness of the transition between inner and outer halo density slopes α . We let them vary in the fit to avoid possible biases due to a more constrained

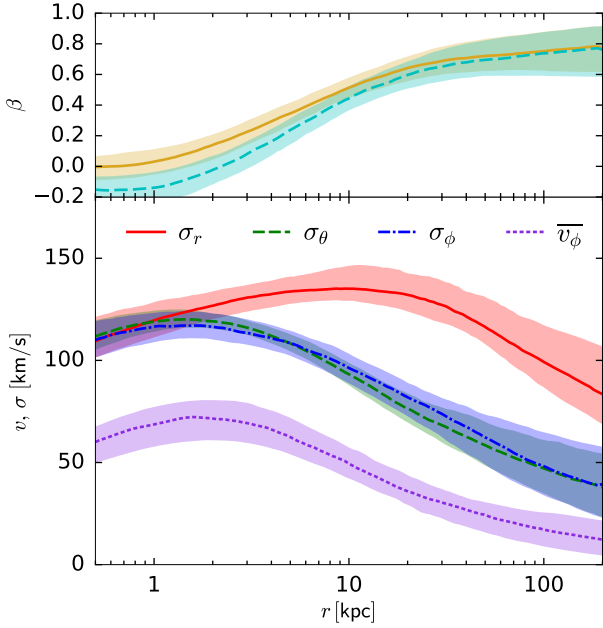


Figure 8. Bottom panel: velocity dispersion and mean azimuthal velocity profiles for an ensemble of models from the MCMC run. Colour coding is the same as in Figure 3, and 68% uncertainty bands are shaded. Top panel: velocity anisotropy coefficient $\beta_a = 1 - (\sigma_\theta^2 + \sigma_\phi^2)/(2\sigma_r^2)$ (solid yellow), and a modified version with σ_ϕ^2 replaced by $\sigma_\phi^2 + \bar{v}_\phi^2$, taking into account the kinetic energy of rotation (dashed cyan).

functional form of our models, but in this case the results become more dependent on the prior. We choose flat priors in $\ln \alpha$, $\ln \beta$ within the ranges $0.3 \leq \alpha \leq 2$ and $2.5 \leq \beta \leq 5$, which favour smaller values of these parameters (closer to the NFW profile).

We explored the robustness of our results to various changes in the input data, for instance, keeping the PM data only for the 91 clusters previously measured by *Gaia* collaboration and *HST* (the sample used in [Posti & Helmi 2019](#) and [Watkins et al. 2018](#)). The range of acceptable models was slightly wider for the more restricted input sample, but the general trends remained the same. We also checked the influence of Sagittarius stream clusters, which are excluded from our main sample: their inclusion increases the inferred circular velocity by $10 - 15 \text{ km s}^{-1}$ outside 20 kpc, which is well within the 1σ confidence interval.

4.4 Results for the DF

The chosen functional form of the DF proves to be flexible enough to reproduce the main trends in the observed velocity distribution (Figure 8). The velocity dispersion is close to isotropic in the central few kpc and radially biased further out, with the anisotropy coefficient $\beta_a \equiv 1 - (\sigma_\theta^2 + \sigma_\phi^2)/(2\sigma_r^2)$ reaching the range $0.6 - 0.8$ at large radii (not to be confused with the outer slope of the halo density profile β). The mean rotation velocity in the central few kpc peaks at a similar amplitude as the data, although at a somewhat smaller galactocentric distance. The marginalized 1d velocity distri-

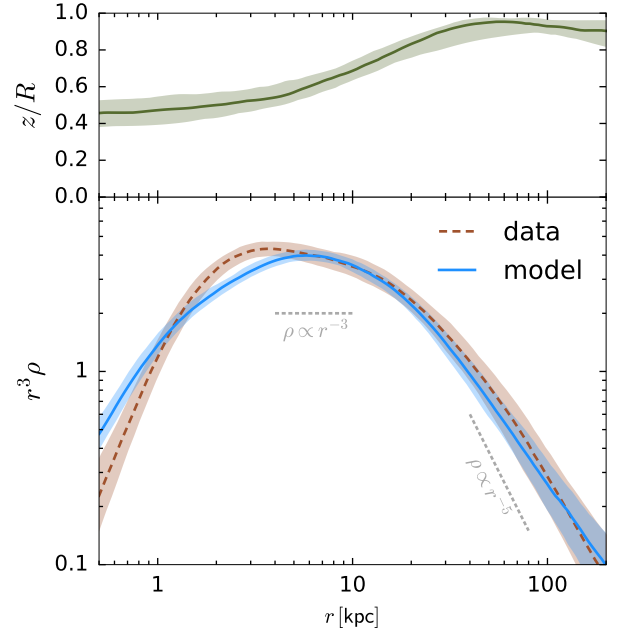


Figure 9. Bottom panel: spatial density profile of the clusters averaged over many models from the MCMC run (solid blue), and estimated from the input data (brown dashed). To compress the dynamical range, the plotted quantity is $r^3 \rho(r)$, in arbitrary units. Top panel: vertical flattening (axis ratio) of the density profile from models.

butions and the density profile matches the data fairly well, as shown on the side panels of Figure 4.

The density profile is also well reproduced, as shown in Figure 9, except in the very centre, where both the input catalogue is likely incomplete, and the model is not expected to be very accurate. The spherically-averaged cluster density produced by the DF does not have an explicit expression, but is well approximated by the $\alpha\beta\gamma$ profile (3) with $\alpha = 0.5$, $\beta = 6$, $\gamma = 0$, and scale radius 6 kpc. The logarithmic slope $d \log \rho / d \log r$ gradually changes from close to -3 around the solar radius to -5 around 100 kpc. The density is significantly flattened in the central few kpc, with axis ratio $z/x \simeq 0.4 - 0.6$.

[Binney & Wong \(2017\)](#) and [Posti & Helmi \(2019\)](#) used a similar DF-based approach as in our study, but divided the entire population into a disc-like and halo-like subset, with two separate DFs. The functional form of their halo DF was also somewhat different from the one in the present study, preventing a direct comparison between parameters. Instead, we focus on more directly observable features, such as the anisotropy and rotation. [Binney & Wong \(2017\)](#) report a similar amount of radial anisotropy in the outer halo as we find, and a weak prograde rotation of the halo component. Their disc component had a much higher mean azimuthal velocity \bar{v}_ϕ , reaching 185 km s^{-1} at 5 kpc, but with a much lower dispersion $\sigma_\phi \lesssim 50 \text{ km s}^{-1}$, whereas σ_z was around 100 km s^{-1} . When combining both components, they find $\bar{v}_\phi \simeq 70 \pm 30 \text{ km s}^{-1}$, consistent with our values. The azimuthal velocity dispersion σ_ϕ then must necessarily increase, and is likely in the same range as we have. The cluster density at large radii declined as r^{-5} or even steeper, and

was quite flattened in the central part - the axis ratio z/R is $\sim 1/3$ for the disc component and $\sim 2/3$ for the halo component, although they do not quote it for the entire population. This is also similar to our results for the overall density profile. [Posti & Helmi \(2019\)](#), on the other hand, find the halo component to be only mildly radially anisotropic ($\beta_a \simeq 0.2$), and the density profile to roughly follow a power law with slope -3.3 , although this probably refers to a smaller range of radii than our (steeper) asymptotic slope.

[Sohn et al. \(2018\)](#) examined the distribution and kinematics of 20 globular clusters with galactocentric distances ranging from 10 to 40 kpc, for which the PM is measured by *HST*. They find a density profile $\rho \propto r^{-3.5}$, and anisotropy $\beta_a \sim 0.4 - 0.7$, similar to our estimates for this range of radii. [Watkins et al. \(2018\)](#) augmented this sample with *Gaia*-derived PM for 34 clusters with apocentre distances greater than 6 kpc. They find their density to be well approximated by a broken power law with inner slope -2 , outer slope -3.5 , and break radius around 4 kpc. Their estimate for velocity anisotropy for the entire *Gaia*+*HST* sample is $\beta_a \sim 0.5 \pm 0.15$. These results are compatible with ours.

Interestingly, the radial velocity anisotropy of the globular cluster population at large radii parallels that of the stellar halo found in some recent studies. [Deason et al. \(2012\)](#) determined $\beta_a \simeq 0.5^{+0.1}_{-0.2}$ at $16 \leq r \leq 50$ kpc from the kinematics blue horizontal branch (BHB) stars, and [Kafle et al. \(2014\)](#) inferred $\beta_a = 0.4 \pm 0.2$ beyond 25 kpc from the kinematics of K-giants and BHB stars in the SDSS survey. On the other hand, [Das et al. \(2016\)](#) find only mild radial anisotropy ($\beta_a \lesssim 0.3$) from these data. The above studies used only the line-of-sight velocities, but [Hattori et al. \(2017\)](#) demonstrated that this could lead to substantial biases in the anisotropy coefficient, and more recent studies used full 3d velocity information. [Bird et al. \(2018\)](#) combined the line-of-sight velocities of K-giants from the LAMOST survey with their PM from *Gaia* DR2, and found $\beta_a = 0.3 - 0.8$ at $25 \leq r \leq 100$ kpc. [Cunningham et al. \(2018\)](#) measured $\beta_a \sim 0.6$ around 25 kpc from the *HST*-based PM and Keck spectroscopy of main-sequence turnoff stars. [Wegg et al. \(2018\)](#) deduced $\beta_a \gtrsim 0.7$ for RR Lyrae stars at $5 \leq r \leq 20$ kpc from *Gaia* DR2 PM (without line-of-sight velocity information). The radially-anisotropic velocity distribution in the halo is also observed in cosmological galaxy formation simulations (e.g., [Fattahi et al. 2018](#); [Mackereth et al. 2019](#)), and has been associated with an ancient major accretion event ([Belokurov et al. 2018](#); [Helmi et al. 2018b](#)). The connection between the kinematics, chemistry and age for both the halo stars and the globular clusters, and its implications for the ‘galactic archeology’, will certainly remain a hot topic for future studies.

4.5 Results for the potential

We now discuss the constraints on the potential obtained by allowing its parameters (mainly the halo) to vary during the fit, together with the DF parameters. When we consider the properties of the potential alone, this implies a marginalization over the DF parameters (cf. [Magorrian 2014](#) for a motivation, although, of course, our DF comes from a restricted family of models and does not explore all possibilities).

Rather than showing the posterior distribution for each parameter, we plot the median value and $1\sigma/2\sigma$ confidence

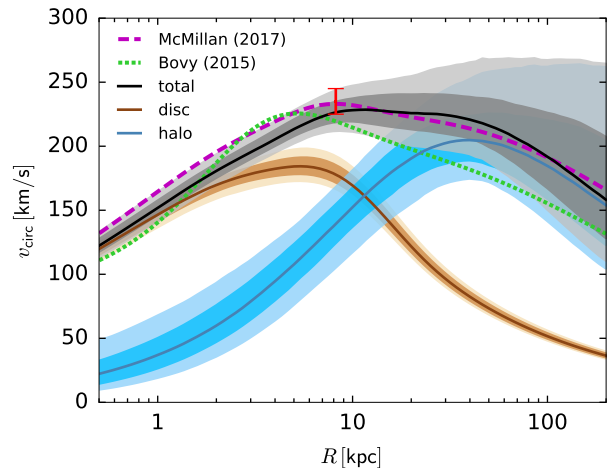


Figure 10. Rotation curves of the ensemble of models from the MCMC run. Solid lines show the median values of circular velocity at a given radius, shaded regions – 68% (darker) and 95% (lighter) confidence regions. Orange is the contribution of disc and bulge, cyan is the halo, and gray is the total. For comparison, the rotation curves of the best-fit potential of [McMillan \(2017\)](#) is shown in dashed magenta line, and the one from [Bovy \(2015\)](#) – in dotted green. The red error bar shows our prior on the circular velocity at $R = 8.2$ kpc (235 ± 10 km s $^{-1}$). The radial distribution of tracers covers roughly the range 1 – 100 kpc.

intervals on the rotation curve in Figure 10. For comparison, we also show the circular velocity of our default potential, taken from [McMillan \(2017\)](#), and the one from [Bovy \(2015\)](#) (*MWPotential2014*). The former potential is within one–two σ from the most-likely models in our chain, but the latter one is clearly inconsistent with the rotation curve beyond 10 kpc. However, the potential at large radii is not well constrained by our models.

The density profile of the halo preferred by the fitting routine is shallower than $\rho \propto r^{-1}$ in the inner part of the Galaxy. The outer slope β is not well constrained, and almost the entire range $2.5 \leq \beta \leq 5$ allowed by our prior is equally likely. Therefore, the formally defined virial mass and radius² have large uncertainties: $M_{\text{virial}} = 1.2^{+1.5}_{-0.5} \times 10^{12} M_{\odot}$, $r_{\text{virial}} = 280^{+80}_{-50}$ kpc. However, it makes little sense to compare these extrapolated values, and more meaningful is the total enclosed mass (including $6.5 \times 10^{10} M_{\odot}$ in baryons) within a given radius probed by the tracer population ($\lesssim 100$ kpc). For our models, the mass within 50 kpc is $0.54^{+0.11}_{-0.08} \times 10^{12} M_{\odot}$, and within 100 kpc is $0.85^{+0.33}_{-0.20} \times 10^{12} M_{\odot}$. As mentioned above, the inclusion of Sagittarius clusters increases these values by 10 – 15%, within the confidence intervals. The enclosed mass profile agrees rather comfortably with most estimates in the literature (see Table 8 in [Bland-Hawthorn & Gerhard 2016](#) or Figure 6 in [Eadie & Juric 2018](#) for a compilation of results).

We restrict the scope of comparison of potential estimates to papers using the kinematics of globular clusters

² We define r_{virial} such that the mean density within this radius is 100 times higher than the cosmic density of matter: $r_{\text{virial}} = (M_{\text{virial}}/10^{12} M_{\odot})^{1/3} \times 260$ kpc (cf. Equation 3 in [Bland-Hawthorn & Gerhard 2016](#)).

only. Our DF-based approach is most similar to that of [Posti & Helmi \(2019\)](#), but their assumptions about the form of gravitational potential make a direct comparison rather difficult. We put a strong prior on the local circular velocity, but a very broad prior on the outer halo density profile, which is not well constrained in our models. They assumed an NFW profile for the halo with a fixed concentration, varying its mass and radius simultaneously, and also allowed it to be non-spherical. However, it should be noted that the prolate shape of their best-fit potential is not compatible with the Stäckel fudge method for action computation, possibly leading to a biased inference on the shape. As mentioned above, we restrict the halo to be either oblate or spherical, and find that a spherical shape is always preferred by the fit. Nevertheless, our median values for the virial mass and radius are close to theirs, but have much larger uncertainties.

From the analysis of *HST*-derived PM for 20 outer globular clusters, [Sohn et al. \(2018\)](#) find the circular velocity at 40 kpc to be 259^{+35}_{-26} km s⁻¹, corresponding to the enclosed mass $0.61^{+0.18}_{-0.12} \times 10^{12} M_{\odot}$. [Watkins et al. \(2018\)](#), with an expanded *Gaia*+*HST* sample, determined the mass enclosed within 40 kpc to be $0.44^{+0.07}_{-0.06} \times 10^{12} M_{\odot}$, or $v_{\text{circ}} = 220^{+17}_{-16}$ km s⁻¹. Our estimate of circular velocity is roughly constant within 50 kpc (225 ± 15 km s⁻¹), closer to the latter study but consistent with both. As discussed in Section 2.3, our PM agree well with the *HST* data (and, of course, with the previously derived *Gaia* PM), hence the agreement with the results obtained by a rather different modelling method is reassuring.

[Eadie et al. \(2017\)](#) also used kinematics of the cluster population, although relying on the older, ground-based PM measurements, and obtained a substantially lower enclosed mass – $(0.34 \pm 0.04) \times 10^{12} M_{\odot}$ within 50 kpc, see Figure 1 in the erratum of that paper. More recently, [Eadie & Juric \(2018\)](#) used our PM catalogue, and obtained the enclosed mass profile that is still considerably lower than ours: $(0.38 \pm 0.05) \times 10^{12} M_{\odot}$ within 50 kpc, and $(0.54 \pm 0.08) \times 10^{12} M_{\odot}$ within 100 kpc. Hence the difference is unlikely to be attributed to the data, but rather to a different method: they assumed a power-law profile for both the tracer DF and the total potential, and in the latter study, only used clusters with galactocentric radii > 15 kpc. They tested their method on simulated galaxies ([Eadie et al. 2018](#)) and found that it may underestimate the enclosed mass (see Figures 4 and 12 in that paper).

Of course, a more elaborate approach would take into account other dynamical constraints on the potential, for instance, from the motion of satellite galaxies, stars in the halo, or tidal streams. The goal of this section was to demonstrate that globular clusters also provide a useful dataset to work with, and their constraints on the potential seem reasonable (although not very tight).

5 SUMMARY

- We provide the catalogue of PM for nearly all Milky Way globular clusters, with estimated uncertainties less than 0.1 mas yr⁻¹ for most objects (dominated by systematic errors in *Gaia* PM, which are fully taken into account by our approach). This catalogue complements the measurements provided by the *Gaia* collaboration ([H18](#)), the independent

Gaia-based catalogue of [Baumgardt et al. \(2019\)](#), and various *HST*-based determinations (e.g., [Sohn et al. 2018](#)), and is in excellent agreement with these studies. By contrast, we find that existing ground-based measurements are not only much less precise than the space-based ones, but often deviate from them by a far larger amount than implied by their quoted uncertainties.

- By analyzing the 6d spatial and velocity distribution of galactic globular clusters, we confirm that their population in the inner Galaxy has a significant rotation, with mean azimuthal velocity in the range 50 – 80 km s⁻¹ within 10 kpc. The velocity dispersion is largely isotropic in this region, with $\sigma \simeq 100 - 120$ km s⁻¹. At large galactocentric distances, the distribution becomes radially anisotropic, with the value of anisotropy parameter $\beta_a \gtrsim 0.6$ similar to that of the stellar halo.

- We also explore the 6d distribution of clusters in the action/angle space. It illustrates more clearly several kinematically distinct populations, for instance, the 6 clusters associated with the Sagittarius stream (confirming some of the candidate members suggested in [Law & Majewski 2010](#)), or the group of outer halo clusters with little net rotation and high radial action, identified in [Myeong et al. \(2018\)](#).

- We find that the distribution of clusters in phase angles deviates from a uniform one, with a deficit of clusters at the opposite side of the Galaxy. Since a dynamically relaxed population is expected to be randomly spread in orbital phases, this hints at a possible observational selection bias, naturally arising from the dust obscuration within the galactic plane.

- We model the observed 6d phase-space distribution of clusters by a combination of an action-space DF $f(\mathbf{J})$ and the total gravitational potential Φ , using a likelihood-based approach with full account of observational errors. By exploring the parameters of the DF and the potential in an MCMC simulation, we find a range of acceptable models, producing a rotation curve that stays at a level 210 – 240 km s⁻¹ in the range 8 – 50 kpc. This is consistent with our default choice of potential from [McMillan \(2017\)](#); however, potentials with a lower circular velocity in this range of radii, such as `MWPotential2014` from [Bovy \(2015\)](#) are disfavoured by the data.

I thank J. Binney, V. Belokurov, D. Erkal, T. Fritz, S. Koposov, G. Myeong, J. Sanders, and the anonymous referee for valuable comments. This work uses the data from the European Space Agency mission *Gaia* (<https://www.cosmos.esa.int/gaia>), processed by the *Gaia* Data Processing and Analysis Consortium (<https://www.cosmos.esa.int/web/gaia/dpac/consortium>). This work was supported by the European Research Council under the 7th Framework programme (grant No. 308024).

REFERENCES

- Babusiaux C., van Leeuwen F., Barstow M., et al. (*Gaia* Collaboration), 2018, *A&A*, 616, 10
 Baumgardt H., Hilker M., Sollima A., Bellini A., 2019, *MNRAS*, 482, 5138
 Belokurov V., Irwin M., Koposov S., et al., 2014, *MNRAS*, 441, 2124

- Belokurov V., Erkal D., Evans N.W., Koposov S., Deason A., 2018, *MNRAS*, 478, 611
- Bianchini P., van der Marel R., del Pino A., et al., 2018, *MNRAS*, 481, 2125
- Binney J., 2012, *MNRAS*, 426, 1324
- Binney J., 2014, *MNRAS*, 440, 787
- Binney J., Wong L.K., 2017, *MNRAS*, 467, 2446
- Bird S., Xue X., Lio C., et al., 2018, arXiv:1805.04503
- Bland-Hawthorn J., Gerhard O., 2016, *ARA&A*, 54, 529
- Bovy J., 2015, *ApJS*, 216, 29
- Bovy J., Hogg D., Roweis S., 2011, *Ann. Appl. Stat.*, 5, 1657
- Bressan A., Marigo P., Girardi L., et al., 2012, *MNRAS*, 427, 127
- Brown A., Vallenari A., Prusti T., et al. (*Gaia* Collaboration), 2018, *A&A*, 616, 1
- Cadelano M., Dalessandro E., Ferraro F., et al., 2017, *ApJ*, 836, 170
- Carballo-Bello J., Ramírez Alegria S., Borissova J., et al., 2016, *MNRAS*, 462, 501
- Casetti-Dinescu D., Girard T., Herrera D., et al., 2007, *AJ*, 134, 195
- Casetti-Dinescu D., Girard T., Korchagin V., et al., 2010, *AJ*, 140, 1282
- Casetti-Dinescu D., Girard T., Jilková L., et al., 2013, *AJ*, 146, 33
- Chemel A., Glushkova E., Dambis A., et al., 2018, *Astrophysical Bulletin*, 72, 162
- Chen S., Richer H., Caiazzo I., Heyl J., 2018, *ApJ*, 867, 132
- Choi J., Dotter A., Conroy C., et al., 2016, *ApJ*, 823, 102
- Chun S.-H., Kim J.-W., Sohn T., et al., 2010, *AJ*, 139, 606
- Cunningham E., Deason A., Sanderson R., et al., 2018, arXiv:1810.12201
- Das P., Williams A., Binney J., 2016, *MNRAS*, 463, 3169
- Deason A., Belokurov V., Evans N.W., An J., 2012, *MNRAS*, 424, L44
- Dias B., Barbuy B., Saviane I., et al., 2016, *A&A*, 590, A9
- Dinescu D., Girard T., van Altena W., 1999, *AJ*, 117, 1792
- Eadie G., Jurić M., 2018, arXiv:1810.10036
- Eadie G., Springford A., Harris W., 2017, *ApJ*, 835, 167
- Eadie G., Keller B., Harris W., 2018, *ApJ*, 865, 72
- Fattahi A., Belokurov V., Deason A., 2018, arXiv:1810.07779
- Forbes D., Bridges T., 2010, *MNRAS*, 404, 1203
- Foreman-Mackey D., Hogg D., Lang D., Goodman J., 2013, *PASP*, 125, 306
- Frank M., Hilker M., Baumgardt H., et al., 2012, *MNRAS*, 423, 2917
- Fritz T., Kallivayalil N., 2015, *ApJ*, 811, 123
- Fritz T., Battaglia G., Pawlowski M., et al., 2018, *A&A* 619, 103
- Green P., Silverman B., 1994, *Nonparametric regression and generalized linear models: a roughness penalty approach*, Chapman & Hall.
- Harris W., 1996, *AJ*, 112, 1487
- Harris W., 2010, arXiv:1012.3224
- Hattori K., Valluri M., Loebman S., Bell E., 2017, *ApJ*, 841, 91
- Helmi A., van Leeuwen F., McMillan P., et al. (*Gaia* Collaboration), 2018a, *A&A*, 616, 12 (H18)
- Helmi A., Babusiaux C., Koppelman H., et al., 2018b, *Nature*, 563, 85
- Hilker M., 2006, *A&A*, 448, 171
- Hogg D., Bovy J., Lang D., 2010, arXiv:1008.4686
- Kaffe P., Sharma S., Lewis G., Bland-Hawthorn J., 2014, *ApJ*, 794, 59
- Kirby E., Simon J., Cohen J., 2015, *ApJ*, 810, 56
- Kharchenko N., Piskunov A., Schilbach E., et al., 2013, *A&A*, 558, 53
- Kruijssen D., Pfeffer J., Reina-Campos M., Crain R., Bastian N., 2018, *MNRAS* (in press), arXiv:1806.05680
- Laevens B., Martin N., Sesar B., et al., 2014, *ApJL*, 786, L3
- Law D., Majewski S., 2010, *ApJ*, 718, 1128
- Libralato M., Bellini A., Bedin L., et al., 2018a, *ApJ*, 854, 45
- Libralato M., Bellini A., van der Marel R., et al., 2018b, *ApJ*, 861, 99
- Lindegren L., 2018, technical note GAIA-C3-TN-LU-LL-124-01
- Lindegren L., Hernandez J., Bombrun A., et al. (*Gaia* Collaboration), 2018, *A&A*, 616, 2
- Mackereth T., Schiavon R., Pfeffer J., et al., 2019, *MNRAS*, 482, 3426
- Magorrian J., 2014, *MNRAS*, 437, 2230
- Massari D., Bellini A., Ferraro F., et al., 2013, *ApJ*, 779, 81
- Massari D., Dalessandro E., Ferraro F., et al., 2015, *ApJ*, 810, 69
- Merritt D., 1997, *AJ*, 114, 228
- Milone A., Villanova S., Bedin L., et al., 2006, *A&A*, 456, 517
- Minniti D., Palma T., Dékány I., et al., 2017, *ApJL*, 838, L14
- Myeong G.C., Evans N.W., Belokurov V., Sanders J., Koposov S., 2018, *ApJL*, 863, L28
- McMillan P., 2017, *MNRAS*, 465, 76
- McMillan P., Binney J., 2013, *MNRAS*, 433, 1411
- Ortolani S., Nardiello D., Pérez-Villegas A., Bica E., Barbuy B., *A&A* (in press); arXiv:1901.03574
- Pace A., Li T., 2018, arXiv:1806.02345
- Pancino E., Bellazzini M., Giuffrida G., Marinoni S., 2017, *MNRAS*, 467, 412
- Pawlowski M., Pflamm-Altenburg J., Kroupa P., 2012, *MNRAS*, 423, 1109
- Perryman M., Lindegren L., Kovalevsky J., et al., 1997, *A&A*, 323, L49
- Posti L., Helmi A., 2019, *A&A*, 621, 56
- Posti L., Binney J., Nipoti C., Ciotti L., 2015, *MNRAS*, 447, 3060
- Press W., Teukolsky S., Vetterling W., Flannery B., 2007, *Numerical recipes* (3rd edition), Cambridge Univ. Press
- Sanders J., Binney J., 2016, *MNRAS*, 457, 2107
- Sohn S.T., van der Marel R., Carlin J., et al., 2015, *ApJ*, 803, 56
- Sohn S.T., Watkins L., Fardal M., et al., 2018, *ApJ*, 862, 52
- Vasiliev E., 2018a, arXiv:1802.08255
- Vasiliev E., 2018b, *MNRAS* (submitted); arXiv:1811.05345
- Vasiliev E., 2019, *MNRAS*, 482, 1525
- Voggel K., Hilker M., Baumgardt H., et al., 2016, *MNRAS*, 460, 3384
- Walker M., Mateo M., Olszewski E., Sen B., Woodroffe M., 2009, *AJ*, 137, 3109
- Watkins L., van der Marel R., 2017, *ApJ*, 839, 79
- Watkins L., van der Marel R., Sohn S.T., Evans N.W., 2018, arXiv:1804.11348
- Wegg C., Gerhard O., Bieth M., 2018, arXiv:1806.09635
- Williams A., Evans N.W., 2015, *MNRAS*, 448, 1360
- Zhao H.-S., 1996, *MNRAS*, 278, 488
- Zinn R., 1985, *ApJ*, 293, 424
- Zonoozi, A.H., Haghi H., Kroupa P., Küpper A., Baumgardt H., 2017, *MNRAS*, 467, 758

APPENDIX A: GAUSSIAN MIXTURE MODELLING

In this section we describe our method for deriving membership probabilities and parameters of the distribution from a mixture of cluster and field stars in the PM space, which is used in Section 2.2. We specialize to the case of two components (members and contaminants, with $c = 1$ being the cluster and $c = 2$ the field population) and two dimensions (μ_α, μ_δ), but present the approach more universally.

We assume that the intrinsic (noise-free) distribution of each component c in the mixture is a Gaussian with some mean value $\bar{\mu}_c$ and a symmetric covariance matrix Σ_c (in this section, vectors are denoted by boldface and matrices

– by sans-serif font). The D -dimensional multivariate Gaussian probability distribution is

$$\mathcal{N}(\boldsymbol{\mu} | \overline{\boldsymbol{\mu}}_c, \boldsymbol{\Sigma}_c) \equiv \frac{\exp\left[-\frac{1}{2}(\boldsymbol{\mu} - \overline{\boldsymbol{\mu}}_c)^T \boldsymbol{\Sigma}_c^{-1} (\boldsymbol{\mu} - \overline{\boldsymbol{\mu}}_c)\right]}{(2\pi)^{D/2} \sqrt{\det \boldsymbol{\Sigma}_c}}. \quad (\text{A1})$$

The overall distribution function of the mixture is a weighted sum of K Gaussian components:

$$f(\boldsymbol{\mu}) = \sum_{c=1}^K q_c \mathcal{N}(\boldsymbol{\mu} | \overline{\boldsymbol{\mu}}_c, \boldsymbol{\Sigma}_c), \quad q_c \geq 0, \quad \sum_{c=1}^K q_c = 1. \quad (\text{A2})$$

The actual values of μ_i for each i -th star are not measured exactly, but with some observational error, which we assume to be normally distributed with a zero mean and an uncertainty covariance matrix \mathbf{E}_i (different for each star). Thus the probability of drawing a value μ_i from the mixture distribution is a convolution of f with the error distribution for this datapoint. For the Gaussian distribution, the convolution is trivial and produces another Gaussian with the same mean and a covariance matrix $\boldsymbol{\Sigma}_c + \mathbf{E}_i$ for each component c .

The total log-likelihood of this Gaussian mixture model, given the set of N measured values μ_i and their error estimates \mathbf{E}_i , is given by

$$\ln \mathcal{L} = \sum_{i=1}^N \ln \left[\sum_{c=1}^K q_c \mathcal{N}(\mu_i | \overline{\boldsymbol{\mu}}_c, \boldsymbol{\Sigma}_c + \mathbf{E}_i) \right]. \quad (\text{A3})$$

The elements of matrices $\boldsymbol{\Sigma}_c$ and vectors $\overline{\boldsymbol{\mu}}_c$, and $K - 1$ weights q_c , are all varied during the fit to maximize the total log-likelihood of the entire ensemble of stars. These quantities may have the same value for all stars, or more generally, be some functions of other attributes of each star besides μ_i and \mathbf{E}_i , with parameters being optimized during the fit. For instance, the intrinsic PM dispersion of cluster stars (the matrix $\boldsymbol{\Sigma}_c$ for $c = 1$), or the prior probability of membership $q_{c;i}$ of each i -th star, may depend on the distance R_i of the given star from the cluster centre.

After the best-fit parameters that maximize the total log-likelihood (A3) are determined, one may compute the posterior probability of i -th star to belong to the k -th component:

$$p_{k;i} = \frac{q_{k;i} \mathcal{N}(\mu_i | \overline{\boldsymbol{\mu}}_{k;i}, \boldsymbol{\Sigma}_{k;i} + \mathbf{E}_i)}{\sum_{c=1}^K q_{c;i} \mathcal{N}(\mu_i | \overline{\boldsymbol{\mu}}_{c;i}, \boldsymbol{\Sigma}_{c;i} + \mathbf{E}_i)}. \quad (\text{A4})$$

Here we made explicit that the parameters of the Gaussian mixture model (means, dispersions and weights) may be different for each star.

The standard approach for finding the maximum of (A3) is the iterative expectation–maximization (EM) algorithm (e.g., Press et al. 2007, Chapter 16.1). It proceeds by repeating the following two steps:

- The probability $p_{c;i}$ of each datapoint to belong to each Gaussian component (Equation A4) is computed from the current parameters of the model, treating them as fixed quantities (expectation step).

- The parameters of the mixture model are updated to maximize the log-likelihood (Equation A3), treating the current membership probabilities as fixed quantities (maximization step). When these parameters are the same for all stars, this amounts to computing the mean values and covariance matrices of each component from the data points,

weighting each data point in accordance to its expected membership probability.

This process is guaranteed to converge to a stationary point, although it may well be a local, not the global maximum of likelihood. This EM algorithm was generalized by Bovy et al. (2011) to the case of noisy data, under the name Extreme Deconvolution. However, we find that the convergence of the EM algorithm is often slow, especially when it is close to a strongly degenerate maximum. Moreover, the maximization step is far more complicated when the parameters of the model are not identical for all stars, but are nonlinear functions of other free parameters and additional attributes of each star. Therefore, we use the standard Nelder–Mead (AMOEBa) algorithm (Press et al. 2007, Chapter 10.5) for locating the maximum of Equation A3 directly.

We adopt a fixed functional form for the distance-dependent prior membership probability, assuming that the surface density of the cluster members follows a spherical Plummer profile, but allow its scale radius R_{scale} to be adjusted during the fit. Recently Pace & Li (2018) used a similar mixture model to determine the mean PM and membership of ultrafaint dwarf satellites from *Gaia* DR2, but they fixed the parameters of their (elliptical) Plummer profiles to the literature values. Of course, structural parameters are also known for most globular clusters, but we do not rely on these data, as the density profile of stars in the *Gaia* data (after applying all quality cutoffs) is quite different from the overall density profile (usually the former has a significantly larger scale radius). Hence we do not attach any physical significance to the inferred scale radius, treating it simply as a nuisance parameter that enhances the contrast between members (more numerous in the central parts) and non-members (uniformly spread across the field of view). As another example, Walker et al. (2009) used a two-component mixture model for the line-of-sight velocity distribution, with the surface density profile of cluster stars represented non-parametrically as an arbitrary non-increasing function of the distance R_i , which was determined during the fit.

We also assume that the intrinsic PM dispersion of cluster members is an isotropic Gaussian, with a diagonal matrix $\boldsymbol{\Sigma}_{1;i} = \text{diag}[\sigma^2(R_i)]$. Here $\sigma(R)$ is a distance-dependent one-dimensional PM dispersion profile, for which we adopt a form that corresponds to a spherical isotropic Plummer model with a scale radius R_σ : $\sigma(R) = \sigma(0) / [1 + (R/R_\sigma)^2]^{1/4}$. As mentioned above, the spatial density of member stars is also approximated by a Plummer profile, but we found that their scale radii are typically different. Instead of using two independent free parameters, we fix $R_\sigma = 0.5 R_{\text{scale}}$, which adequately represents the intrinsic PM dispersion profiles computed from *a posteriori* cluster members. The amplitude $\sigma(0)$ remains a free parameter during the fit, but we add a penalty term to the total likelihood (A3) that discourages $\sigma(0)$ from exceeding the central line-of-sight velocity dispersion as quoted in the catalogue of Baumgardt et al. (2019). In the present study, we use a single value of $\overline{\mu}_1$ (mean PM of the cluster) and a fixed functional form of $\sigma(R)$, but a more general model for the intrinsic kinematics (flexible rotation and PM dispersion profiles) is explored in the companion paper (Vasiliev 2018b).

After the maximum-likelihood solution has been found,

we need to estimate the uncertainties on the derived parameters, in particular, $\overline{\boldsymbol{\mu}}_1$. Since the log-likelihood function (A3) is quadratic near its maximum, we compute its Hessian matrix $\mathbf{H} \equiv \text{d}^2 \ln \mathcal{L} / \text{d}\xi_\alpha \text{d}\xi_\beta$, where the vector $\boldsymbol{\xi}$ contains all model parameters. The inverse of the Hessian (with negative sign) is the covariance matrix of parameter uncertainties, of which we are only interested in the 2×2 fragment corresponding to $\overline{\boldsymbol{\mu}}_1$. The uncertainties on the mean values of each component in a Gaussian mixture are larger than in the case of a single Gaussian (when they could be computed from data error estimates \mathbf{E}_i), because they also encompass the uncertainty of attributing each data point to either component. We also experimented with inferring the uncertainties from a MCMC simulation, and the results were similar.

The above procedure computes the statistical uncertainties, but for the majority of clusters, these are smaller than the systematic errors in *Gaia* PM. Unfortunately, it seems impossible to combine the probabilistic membership determination with a proper treatment of spatially correlated systematic errors. Hence we estimate the latter with the method described in the Appendix of the companion paper, using only stars with membership probability $p > 0.8$, and list the larger of the two uncertainty estimates (statistical or systematic) in the final catalogue.

The Gaussian mixture modelling is superior to the more conventional techniques such as σ -clipping, not only because it is a statistically well-defined inference procedure and not just a prescription (cf. Hogg et al. 2010), but also because it can more robustly isolate a not-too-narrow peak in a crowded background population. However, for it to work correctly, one must include a sufficient number of non-member stars in the input sample. The probability of each data point to belong to either cluster or field component depends on several factors: the geometric distance from the cluster centre, the distance from each component's centre in the PM space (normalized by the inverse of $\boldsymbol{\Sigma}_c + \mathbf{E}_i$), and the total weight of each component. Consider an example where the PM distribution of both populations are centered at origin, cluster stars have intrinsic PM dispersion 0.1, and field stars ~ 5 . If the fraction of field stars is 10^{-3} , then a star with a unit measurement error would need to be at a distance $\gtrsim 4.2$ from the origin, in order for its membership probability to drop below 0.5; however, if the fraction of contaminants is 50%, then this star will be classified as a likely field star already when it is 1.8σ off. Hence, somewhat counter-intuitively, a larger contaminant fraction leads to a cleaner sample. In addition, the implicit assumption is that the field population has a broad enough distribution to capture any non-compliant measurements; however, if there are very few truly non-member stars, the parameters of the field distribution cannot be reliably determined, again distorting the classification. This is why we sometimes had to consider a rather large area on the sky compared to the cluster half-mass radius, especially for clusters in very sparsely populated regions in the halo.

We provide a PYTHON script that implements our approach for membership determination, measures the mean PM and computes various auxiliary quantities (such as actions and peri/apocentre distances) at <https://github.com/GalacticDynamics-Oxford/GaiaTools>.

APPENDIX B: NON-PARAMETRIC ESTIMATES OF 1D DISTRIBUTIONS

This section explains the method for estimating 1d distributions of various quantities from the observed cluster positions and velocities, taking into account both their measurement uncertainties and finite-sample effects, which is used in Section 3. We employ a non-parametric approach similar to the one from Merritt (1997), and described in detail in Vasiliev (2018a, Section A.2). The function $f(x; \mathbf{c})$ to be estimated is represented as a cubic spline with a sufficient number M of pre-defined control points $\{x_m\}_{m=1}^M$, and the same number of free parameters $\{c_m\}$ specifying its value at these points, or by some other linear combination of basis functions. The parameters are chosen to maximize the cost function

$$F(\mathbf{c}) \equiv \ln \mathcal{L}(\text{data}; \mathbf{c}) + \mathcal{P}(\mathbf{c}), \quad (\text{B1})$$

which consists of two terms: one describes the log-likelihood of the observed data, and the other is the penalty for non-smoothness, introduced to prevent overfitting (e.g., Green & Silverman 1994).

For the purpose of probability density estimation (e.g., distribution of particles in velocity space or in log-radius, as in side panels of Figure 4), it is convenient to let $f(x)$ be the logarithm of the probability density $p(x)$: in this way its positiveness is ensured by construction, and the maximum-likelihood solution is found by unconstrained minimization. Of course, $p(x)$ must be normalized to unity, which may be ensured by adding a normalization term to \mathcal{L} :

$$\ln \mathcal{L} \equiv \sum_{i=1}^{N_{\text{data}}} f(x_i; \mathbf{c}) - N_{\text{data}} \int \exp[f(x; \mathbf{c})] dx. \quad (\text{B2})$$

Because of the normalization constraint, only $M - 1$ of parameters c_m are independent; the remaining one may be fixed e.g. to zero. Note that for a spline function f , the first term is linear in \mathbf{c} , but the normalization condition is not.

For estimating the distribution function $f(\theta)$ in phase angle (Figure 7), it is more convenient to represent it a Fourier series with free parameters $\{c_m, s_m\}_{m=1}^M$:

$$\ln \mathcal{L} \equiv \sum_{i=1}^{N_{\text{data}}} \ln \left[\frac{1}{2\pi} + \sum_{m=1}^M (c_m \cos m\theta + s_m \sin m\theta) \right]. \quad (\text{B3})$$

This automatically ensures correct normalization, but the non-negativity constraint must be imposed explicitly in the fitting procedure.

Finally, for a non-parametric recovery of mean velocity \bar{v} and its dispersion σ as functions of radius (Figure 3), they are represented as cubic splines in $\ln r$, and the log-likelihood is written as

$$\ln \mathcal{L} \equiv \sum_{i=1}^{N_{\text{data}}} \left(-\ln [\sqrt{2\pi} \sigma(\ln r_i)] - \frac{[v_i - \bar{v}(\ln r_i)]^2}{2\sigma(\ln r_i)^2} \right). \quad (\text{B4})$$

In this case the probability function for data points is a Gaussian, i.e., already normalized, but we need to impose a non-negativity constraint on $\sigma(r)$.

In all these cases, the uncertainties in the data are dealt with in the same way: instead of taking the likelihood of a single data point at a time, we take the average likelihood over all Monte Carlo samples representing its measurement errors.

The penalty term prevents the solution from becoming too wiggly; a standard choice is

$$\mathcal{P}(\mathbf{c}) = -\lambda \int [f''(x; \mathbf{c})]^2 dx, \quad (\text{B5})$$

where f are spline functions for the log-density, or the distribution function in angles, or the radial profile of velocity dispersion. The smoothing parameter λ is determined by the leave-one-out cross-validation procedure. For each value of λ , we perform N_{data} separate maximizations of F for all data points except i -th one, and then compute the likelihood of this omitted data point, using the best-fit parameters $\mathbf{c}^{(-i)}$ inferred from the remaining points. The cross-validation score is the sum of these likelihoods for all data points, and it typically depends on the parameter λ in a non-monotonic way: zero or very small smoothing produces too wiggly fitting functions $f(x; \mathbf{c}^{(-i)})$, which are poor predictors for the omitted data points, and conversely too much smoothing ignores the data altogether. Therefore, there is an optimal value of λ that maximizes the cross-validation score. For this optimal choice, the best-fit function will be rather smooth and nearly independent of the number of free parameters M (terms in the Fourier series or control points in splines), provided that M is large enough to represent all significant variations (not driven by noise). For our 150 clusters, 10 terms are enough in all estimators.

After fixing the value of λ , we finally find the best-fit parameters \mathbf{c} from the entire dataset. The uncertainties due to the finite number of data points are estimated by computing the Hessian matrix $d^2F/dc_m dc_n$, the inverse of which (with negative sign) is the covariance matrix of fit parameters \mathbf{c} . As these parameters are not of much physical relevance themselves, we instead plot the median value of the fit function $f(x)$ and its 68% uncertainty intervals. Namely, we sample the parameters \mathbf{c} from a multivariate Gaussian distribution with the given mean (best-fit values) and covariance matrix, plot $f(x; \mathbf{c})$ for each choice of \mathbf{c} , and at each value of coordinate x take the interval of values of f containing 16% to 84% percentile of plotted curves as the confidence interval. Alternatively, we computed the uncertainties by running a MCMC simulation and taking the ensemble of parameters \mathbf{c} from the chain, instead of sampling them from the inverse Hessian; the results are very similar.

We stress that these non-parametric estimates are used to visualize the trends in the data and the significance of various features, but in comparing the parametric models of Section 4 to the data, we again use the original measurements and their uncertainties represented by Monte Carlo samples, not the fitted non-parametric curves.

APPENDIX C: THE CATALOGUE

Table C1 lists the mean PM and other parameters for all 150 globular clusters in this study, which are discussed in Section 2.3. The rest of this section contains notes on several individual objects with some particular features.

AM 1, Pal 3 and Pal 4 are very distant halo clusters ($D \simeq 100$ kpc) in sparsely populated regions on the sky. *Gaia* detects several dozen stars in each of them, mostly belonging to the horizontal branch (G magnitudes around 20.5 – 21, with correspondingly large PM errors), and a few

brighter ones in the upper red giant branch. Almost all of them are also identified as possible member stars by Hilker (2006) for the first two clusters, based on photometry, and by Frank et al. (2012) for the last one, based on line-of-sight velocities. The large distance and small number of member stars mean that the statistical errors in transverse velocities are quite large, of order 100 km s^{-1} . Interestingly, Zonoozi et al. (2017) predicted an eccentric orbit for Pal 4, based on evolutionary N -body simulations, and their prediction for PM is consistent with the actual measurement.

BH 176 did not have line-of-sight velocity listed in either Harris (2010) or Baumgardt et al. (2019) catalogues; we took the value from Dias et al. (2016).

Crater (Laevens 1), discovered independently by Belokurov et al. (2014) and Laevens et al. (2014), is the most distant globular cluster in our sample, not listed in the Harris (2010) catalogue. Follow-up spectroscopic studies of Kirby et al. (2015) and Voggel et al. (2016) determined the line-of-sight velocity ($\sim 149 \pm 1.5 \text{ km s}^{-1}$) and provided the list of likely members, of which 5 are found in *Gaia* data with PM close to zero (as could be expected for such a distant object). We identified several more candidate members based on their PM, but the estimate of the statistical uncertainty for the mean PM is still very large, corresponding to an error of 200 km s^{-1} in the transverse velocity. Our PM agree fairly well with the measurement of Fritz et al. (2018), which is also based on *Gaia*.

Djorg 1 and Terzan 10 are strongly extincted clusters in the direction of Galactic centre. The distances listed in the Harris catalogue are replaced with values measured by Ortolani et al. (2019), and the line-of-sight velocity for the latter cluster is taken from Geisler et al. (in prep.).

FSR 1716 is another object not present in the Harris (2010) catalogue, which was classified as a globular cluster by Minniti et al. (2017). It is also located in a strongly extincted region but is firmly detected in the PM space.

FSR 1735 (2MASS-GC03) is a strongly extincted cluster close to the plane of the Galaxy. Carballo-Bello et al. (2016) measured the metallicity $[\text{Fe}/\text{H}] = -0.9 \pm 0.2$ and line-of-sight velocity $V_{\text{los}} = -78 \pm 12 \text{ km s}^{-1}$ from near-infrared spectroscopy of 10 candidate member stars. These stars are also detected in *Gaia*. However, the five candidate members suggested in that paper have very disparate PM, hence cannot belong to the cluster. Instead, another four stars (numbered 04, 05, 09 and 10 in their Table 1) are clustered both in the PM space (around $\mu_\alpha = -5, \mu_\delta = 0$) and in the colour-magnitude diagram near the tip of the red giant branch; three of them have measured line-of-sight velocities consistent with $V_{\text{los}} = 5 \pm 10 \text{ km s}^{-1}$, which we take as the mean value for the cluster. The Gaussian mixture analysis picks up a dozen more stars which likely belong to the cluster and have PM consistent with that tentative value; they also line up nicely in the image plane.

Table C1. Catalog of PM for the Milky Way globular clusters.

Names of clusters with no previous space-based PM measurements (except the independent catalogue of [Baumgardt et al. 2019](#)) are highlighted in italic. Coordinates α , δ and the distance D are taken mostly from the [Harris \(2010\)](#) catalogue, with modifications highlighted in italic. The line-of-sight velocity V_{los} and its error estimate $\epsilon_{V_{\text{los}}}$ are taken from [Baumgardt et al. \(2019\)](#) or other recent papers. Mean PM $\overline{\mu_\alpha} \equiv [d\alpha/dt] \cos \delta$, $\overline{\mu_\delta} \equiv d\delta/dt$ are derived in this work. Their uncertainty estimates $\epsilon_{\overline{\mu_\alpha}}$, $\epsilon_{\overline{\mu_\delta}}$ already take into account systematic errors, and $r_{\overline{\mu_\alpha} \overline{\mu_\delta}}$ is the correlation coefficient (normalized non-diagonal element in the error covariance matrix). Last two columns list the angular scale radius R_{scale} of the best-fit Plummer profile of member stars in the filtered *Gaia* catalogue, and their number.

Name	α deg	δ	D kpc	V_{los} km s $^{-1}$	$\epsilon_{V_{\text{los}}}$	$\overline{\mu_\alpha}$ mas yr $^{-1}$	$\overline{\mu_\delta}$ mas yr $^{-1}$	$\epsilon_{\overline{\mu_\alpha}}$ mas yr $^{-1}$	$\epsilon_{\overline{\mu_\delta}}$ mas yr $^{-1}$	$r_{\overline{\mu_\alpha} \overline{\mu_\delta}}$	R_{scale} arcmin	N_\star
NGC 104 (47 Tuc)	6.024	-72.081	4.5	-17.21	0.18	5.237	-2.524	0.039	0.039	-0.002	18.3	23917
NGC 288	13.188	-26.583	8.9	-44.83	0.13	4.267	-5.636	0.054	0.053	0.018	6.0	2555
NGC 362	15.809	-70.849	8.6	223.26	0.28	6.730	-2.535	0.053	0.052	-0.004	7.8	1741
<i>Whiting 1</i>	30.738	-3.253	30.1	-130.41	1.79	-0.234	-1.782	0.115	0.094	-0.050	0.5	11
<i>NGC 1261</i>	48.068	-55.216	16.3	71.36	0.24	1.632	-2.038	0.057	0.057	0.009	4.1	541
<i>Pal 1</i>	53.334	79.581	11.1	-75.41	0.21	-0.171	0.070	0.074	0.081	0.003	0.7	51
<i>E 1 (AM 1)</i>	58.760	-49.615	123.3	118.00	14.14	0.357	-0.424	0.128	0.169	-0.108	0.4	39
<i>Eridanus</i>	66.185	-21.187	90.1	-23.79	1.07	0.493	-0.402	0.084	0.087	-0.133	0.8	15
<i>Pal 2</i>	71.525	31.381	27.2	-135.97	1.55	1.034	-1.557	0.075	0.068	0.009	1.5	76
NGC 1851	78.528	-40.047	12.1	320.30	0.25	2.120	-0.589	0.054	0.054	-0.007	5.5	786
NGC 1904 (M 79)	81.046	-24.525	12.9	205.84	0.19	2.467	-1.573	0.057	0.058	-0.001	4.5	583
NGC 2298	102.248	-36.005	10.8	146.18	0.71	3.316	-2.186	0.061	0.061	0.001	3.2	444
NGC 2419	114.535	38.882	82.6	-20.67	0.34	-0.011	-0.557	0.064	0.061	0.010	3.2	131
<i>Pyxis</i>	136.991	-37.221	39.4	40.46	0.21	1.078	0.212	0.068	0.071	0.025	2.0	64
NGC 2808	138.013	-64.864	9.6	103.90	0.30	1.005	0.274	0.051	0.051	-0.006	8.4	1837
<i>E 3 (ESO 37-1)</i>	140.238	-77.282	8.1	4.93	0.42	-2.695	7.115	0.064	0.064	-0.009	1.9	191
<i>Pal 3</i>	151.383	0.072	92.5	94.04	0.80	0.055	-0.085	0.146	0.171	-0.515	0.7	34
NGC 3201	154.403	-46.412	4.9	494.34	0.14	8.324	-1.991	0.044	0.044	0.001	12.5	7021
<i>Pal 4</i>	172.320	28.974	108.7	72.40	0.24	-0.135	-0.518	0.106	0.176	-0.471	0.5	32
<i>Crater (Laevens 1)</i>	174.067	-10.877	145.0	148.30	0.93	0.001	-0.130	0.308	0.190	-0.181	0.4	10
<i>NGC 4147</i>	182.526	18.543	19.3	179.52	0.33	-1.705	-2.114	0.065	0.063	-0.014	2.2	248
NGC 4372	186.439	-72.659	5.8	75.59	0.30	-6.378	3.358	0.050	0.050	0.001	7.8	2189
<i>Rup 106</i>	189.667	-51.150	21.2	-38.42	0.30	-1.263	0.399	0.064	0.063	0.027	2.1	119
NGC 4590 (M 68)	189.867	-26.744	10.3	-92.99	0.22	-2.752	1.762	0.054	0.053	-0.027	6.7	1479
NGC 4833	194.891	-70.876	6.6	201.99	0.40	-8.361	-0.949	0.055	0.054	0.006	7.1	1861
NGC 5024 (M 53)	198.230	18.168	17.9	-62.85	0.26	-0.148	-1.355	0.053	0.052	-0.025	7.7	1924
NGC 5053	199.113	17.700	17.4	42.77	0.25	-0.366	-1.248	0.058	0.056	-0.021	4.0	657
NGC 5139 (ω Cen)	201.697	-47.480	5.2	234.28	0.24	-3.234	-6.719	0.039	0.039	-0.002	25.2	23635
NGC 5272 (M 3)	205.548	28.377	10.2	-147.28	0.34	-0.142	-2.647	0.045	0.043	-0.006	9.5	3924
NGC 5286	206.612	-51.374	11.7	62.38	0.40	0.207	-0.111	0.059	0.059	-0.002	4.1	431
NGC 5466	211.364	28.534	16.0	106.93	0.18	-5.412	-0.800	0.053	0.053	0.010	4.8	988
NGC 5634	217.405	-5.976	25.2	-16.07	0.60	-1.724	-1.507	0.064	0.064	-0.002	2.3	188
<i>NGC 5694</i>	219.901	-26.539	35.0	-139.55	0.49	-0.486	-1.071	0.069	0.068	-0.060	2.1	100
<i>IC 4499</i>	225.077	-82.214	18.8	38.41	0.31	0.491	-0.485	0.059	0.059	0.006	3.4	387
<i>NGC 5824</i>	225.994	-33.068	32.1	-25.24	0.52	-1.170	-2.226	0.060	0.058	0.012	5.0	373
<i>Pal 5</i>	229.022	-0.112	23.2	-58.60	0.21	-2.736	-2.646	0.064	0.064	-0.048	3.3	203
NGC 5897	229.352	-21.010	12.5	101.31	0.22	-5.427	-3.438	0.057	0.056	-0.014	4.8	1002
NGC 5904 (M 5)	229.638	2.081	7.5	53.70	0.25	4.078	-9.854	0.047	0.047	-0.008	10.0	4502
NGC 5927	232.003	-50.673	7.7	-104.07	0.28	-5.049	-3.231	0.055	0.055	-0.003	11.0	1829
NGC 5946	233.869	-50.660	10.6	137.41	1.42	-5.331	-1.614	0.065	0.064	-0.008	2.9	217
<i>BH 176 (ESO 224-8)</i>	234.781	-50.053	18.9	-6.00	14.00	-4.002	-3.064	0.071	0.067	0.019	2.3	115
NGC 5986	236.512	-37.786	10.4	101.18	0.43	-4.186	-4.604	0.060	0.059	-0.011	5.6	812
<i>FSR 1716</i>	242.625	-53.748	9.5	-33.14	1.01	-4.527	-8.639	0.066	0.064	-0.028	2.3	67
<i>Pal 14 (Arp 1)</i>	242.752	14.958	76.5	72.30	0.14	-0.504	-0.461	0.081	0.078	0.167	1.8	61
<i>BH 184 (Lynga 7)</i>	242.765	-55.318	8.0	17.86	0.83	-3.844	-7.039	0.064	0.063	-0.007	2.2	154
NGC 6093 (M 80)	244.260	-22.976	10.0	10.93	0.39	-2.931	-5.578	0.061	0.060	0.001	4.3	474
NGC 6121 (M 4)	245.897	-26.526	2.2	71.05	0.08	-12.490	-19.001	0.044	0.044	-0.001	8.6	7526
<i>NGC 6101</i>	246.451	-72.202	15.4	366.33	0.32	1.757	-0.223	0.053	0.054	0.005	6.1	1260
NGC 6144	246.808	-26.023	8.9	195.74	0.74	-1.772	-2.626	0.061	0.060	0.002	2.0	122
<i>NGC 6139</i>	246.918	-38.849	10.1	24.41	0.95	-6.184	-2.648	0.062	0.061	0.006	3.6	426
<i>Terzan 3</i>	247.167	-35.353	8.2	-135.76	0.57	-5.602	-1.690	0.063	0.062	0.006	2.9	365
NGC 6171 (M 107)	248.133	-13.054	6.4	-34.68	0.19	-1.924	-5.968	0.057	0.056	0.000	4.8	1304
<i>ESO 452-11 (1636-283)</i>	249.856	-28.399	8.3	16.27	0.48	-1.540	-6.418	0.070	0.068	-0.016	0.9	28
NGC 6205 (M 13)	250.422	36.460	7.1	-244.49	0.43	-3.164	-2.588	0.047	0.047	0.011	10.3	3982
<i>NGC 6229</i>	251.745	47.528	30.5	-138.64	0.77	-1.192	-0.440	0.062	0.064	0.009	2.2	123
NGC 6218 (M 12)	251.809	-1.949	4.8	-41.35	0.20	-0.141	-6.802	0.052	0.051	0.019	6.8	3356
<i>FSR 1735 (2MASS-GC03)</i>	253.044	-47.058	10.8	5.00	10.00	-5.015	-0.141	0.112	0.103	-0.134	0.8	16

Table C1 – *continued* Catalog of PM for the Milky Way globular clusters

Name	α	δ	D	V_{los}	$\epsilon_{V_{\text{los}}}$	$\overline{\mu}_{\alpha}$	$\overline{\mu}_{\delta}$	$\epsilon_{\overline{\mu}_{\alpha}}$	$\epsilon_{\overline{\mu}_{\delta}}$	$r_{\overline{\mu}_{\alpha} \overline{\mu}_{\delta}}$	R_{scale}	N_{\star}
NGC 6235	253.355	-22.177	11.5	126.68	0.33	-3.973	-7.624	0.064	0.063	0.009	2.1	168
NGC 6254 (M 10)	254.288	-4.100	4.4	74.02	0.31	-4.759	-6.554	0.049	0.048	0.012	8.2	5285
NGC 6256	254.886	-37.121	10.3	-101.37	1.19	-3.664	-1.493	0.068	0.066	0.005	1.9	126
Pal 15	254.963	-0.539	45.1	72.27	1.74	-0.580	-0.861	0.076	0.070	0.027	1.8	60
NGC 6266 (M 62)	255.303	-30.114	6.8	-73.49	0.70	-5.041	-2.952	0.057	0.057	0.004	6.9	1169
NGC 6273 (M 19)	255.657	-26.268	8.8	145.54	0.59	-3.232	1.669	0.057	0.056	0.010	6.2	1059
NGC 6284	256.119	-24.765	15.3	28.26	0.93	-3.196	-2.008	0.065	0.064	0.009	2.5	141
NGC 6287	256.288	-22.708	9.4	-294.74	1.65	-4.977	-1.882	0.063	0.062	0.003	2.8	338
NGC 6293	257.543	-26.582	9.5	-143.66	0.39	0.890	-4.338	0.064	0.063	0.007	2.4	182
NGC 6304	258.634	-29.462	5.9	-108.62	0.39	-4.051	-1.073	0.063	0.063	0.004	2.8	159
NGC 6316	259.155	-28.140	10.4	99.81	0.82	-4.945	-4.608	0.066	0.065	0.012	2.5	114
NGC 6341 (M 92)	259.281	43.136	8.3	-120.48	0.27	-4.925	-0.536	0.052	0.052	0.010	7.4	1847
NGC 6325	259.497	-23.766	7.8	29.54	0.58	-8.426	-9.011	0.068	0.067	0.008	1.7	147
NGC 6333 (M 9)	259.797	-18.516	7.9	310.75	2.12	-2.228	-3.214	0.059	0.058	0.009	4.7	526
NGC 6342	260.292	-19.587	8.5	116.56	0.74	-2.932	-7.101	0.064	0.064	0.004	2.2	195
NGC 6356	260.896	-17.813	15.1	38.93	1.88	-3.814	-3.381	0.060	0.059	0.010	4.7	547
NGC 6355	260.994	-26.353	9.2	-194.13	0.83	-4.657	-0.522	0.066	0.065	0.014	1.6	93
NGC 6352	261.371	-48.422	5.6	-125.63	1.01	-2.172	-4.398	0.056	0.056	0.003	5.4	2064
IC 1257	261.785	-7.093	25.0	-137.97	2.04	-0.928	-1.407	0.087	0.081	0.037	0.8	16
Terzan 2 (HP 3)	261.888	-30.802	7.5	128.96	1.18	-2.237	-6.210	0.081	0.075	0.086	0.8	25
NGC 6366	261.934	-5.080	3.5	-120.65	0.19	-0.363	-5.115	0.053	0.053	0.015	6.2	2226
Terzan 4 (HP 4)	262.663	-31.596	7.2	-39.93	3.76	-5.386	-3.361	0.088	0.080	0.020	0.6	26
BH 229 (HP 1)	262.772	-29.982	8.2	40.61	1.29	2.462	-10.142	0.073	0.071	-0.001	1.4	35
NGC 6362	262.979	-67.048	7.6	-14.58	0.18	-5.510	-4.750	0.051	0.052	-0.000	6.5	2877
NGC 6380 (Ton 1)	263.617	-39.069	10.9	-6.54	1.48	-2.142	-3.107	0.067	0.066	-0.006	2.1	181
Terzan 1 (HP 2)	263.949	-30.481	6.7	57.55	1.61	-2.967	-4.811	0.083	0.080	0.026	1.1	65
Ton 2 (Pismis 26)	264.044	-38.553	8.2	-184.72	1.12	-5.912	-0.548	0.067	0.066	0.013	1.9	116
NGC 6388	264.072	-44.736	9.9	82.85	0.48	-1.331	-2.672	0.057	0.057	0.004	5.6	791
NGC 6402 (M 14)	264.400	-3.246	9.3	-60.71	0.45	-3.640	-5.035	0.058	0.058	0.008	4.8	718
NGC 6401	264.652	-23.910	10.6	-99.26	3.18	-2.849	1.476	0.070	0.069	-0.001	2.0	60
NGC 6397	265.175	-53.674	2.3	18.39	0.10	3.285	-17.621	0.043	0.043	0.001	11.1	11406
Pal 6	265.926	-26.223	5.8	176.28	1.53	-9.256	-5.330	0.078	0.076	0.038	1.3	47
NGC 6426	266.228	3.170	20.6	-210.51	0.51	-1.862	-2.994	0.064	0.064	0.019	2.1	144
Djorg 1	266.868	-33.066	9.3	-359.81	1.98	-5.158	-8.323	0.081	0.076	-0.006	0.9	28
Terzan 5 (Terzan 11)	267.020	-24.779	6.9	-81.40	1.36	-1.560	-4.724	0.106	0.102	0.072	2.0	59
NGC 6440	267.220	-20.360	8.5	-69.39	0.93	-1.070	-3.828	0.069	0.068	0.025	2.9	154
NGC 6441	267.554	-37.051	11.6	17.27	0.93	-2.568	-5.322	0.059	0.059	0.001	6.2	247
Terzan 6 (HP 5)	267.693	-31.275	6.8	137.15	1.70	-5.634	-7.042	0.186	0.156	0.155	1.1	24
NGC 6453	267.715	-34.599	11.6	-91.16	3.08	0.165	-5.895	0.071	0.070	0.006	1.8	30
NGC 6496	269.765	-44.266	11.3	-134.72	0.26	-3.037	-9.239	0.061	0.061	0.004	2.8	350
Terzan 9	270.412	-26.840	7.1	29.31	2.96	-2.197	-7.451	0.073	0.070	0.041	0.9	50
Djorg 2 (ESO 456-38)	270.455	-27.826	6.3	-148.05	1.38	0.515	-3.052	0.079	0.074	-0.036	0.9	9
NGC 6517	270.461	-8.959	10.6	-37.07	1.68	-1.498	-4.221	0.066	0.066	0.016	2.5	237
Terzan 10	270.742	-26.067	10.4	208.00	3.60	-6.912	-2.409	0.085	0.080	0.074	1.6	27
NGC 6522	270.892	-30.034	7.7	-13.90	0.71	2.618	-6.431	0.072	0.071	0.003	1.9	38
NGC 6535	270.960	-0.298	6.8	-214.85	0.46	-4.249	-2.900	0.064	0.064	0.007	2.2	318
NGC 6528	271.207	-30.056	7.9	210.31	0.75	-2.327	-5.527	0.074	0.071	0.018	0.9	17
NGC 6539	271.207	-7.586	7.8	35.69	0.55	-6.865	-3.477	0.061	0.061	0.009	3.2	563
NGC 6540 (Djorg 3)	271.536	-27.765	5.3	-17.98	0.84	-3.760	-2.799	0.077	0.076	0.029	0.8	15
NGC 6544	271.836	-24.997	3.0	-38.12	0.76	-2.349	-18.557	0.060	0.060	0.001	5.2	551
NGC 6541	272.010	-43.715	7.5	-163.97	0.46	0.349	-8.843	0.056	0.055	-0.007	6.3	1375
ESO 280-06	272.275	-46.423	21.4	93.20	0.34	-0.552	-2.724	0.082	0.075	0.085	1.1	33
NGC 6553	272.323	-25.909	6.0	0.72	0.40	0.246	-0.409	0.063	0.063	0.003	3.5	325
NGC 6558	272.573	-31.764	7.4	-195.70	0.70	-1.810	-4.133	0.067	0.066	0.003	1.1	42
Pal 7 (IC 1276)	272.684	-7.208	5.4	155.06	0.69	-2.577	-4.374	0.059	0.059	0.009	4.2	938
Terzan 12	273.066	-22.742	4.8	94.77	0.97	-6.151	-2.679	0.069	0.068	0.049	1.5	104
NGC 6569	273.412	-31.827	10.9	-49.83	0.50	-4.109	-7.267	0.062	0.062	0.005	2.7	169
BH 261 (ESO 456-78)	273.527	-28.635	6.5	-29.38	0.60	3.590	-3.573	0.077	0.076	0.037	0.5	13
NGC 6584	274.657	-52.216	13.5	260.64	1.58	-0.053	-7.185	0.061	0.061	-0.000	3.6	392
NGC 6624	275.919	-30.361	7.9	54.26	0.45	0.099	-6.904	0.065	0.064	0.002	2.0	162
NGC 6626 (M 28)	276.137	-24.870	5.5	11.11	0.60	-0.301	-8.913	0.061	0.061	-0.003	3.7	383
NGC 6638	277.734	-25.497	9.4	8.63	2.00	-2.550	-4.075	0.066	0.065	0.013	1.9	103
NGC 6637 (M 69)	277.846	-32.348	8.8	46.63	1.45	-5.113	-5.813	0.063	0.063	0.011	2.5	283
NGC 6642	277.975	-23.475	8.1	-33.23	1.13	-0.189	-3.898	0.065	0.065	0.004	1.8	93

Table C1 – *continued* Catalog of PM for the Milky Way globular clusters

Name	α	δ	D	V_{los}	$\epsilon_{V_{\text{los}}}$	$\overline{\mu}_{\alpha}$	$\overline{\mu}_{\delta}$	$\epsilon_{\overline{\mu}_{\alpha}}$	$\epsilon_{\overline{\mu}_{\delta}}$	$r_{\overline{\mu}_{\alpha} \overline{\mu}_{\delta}}$	R_{scale}	N_{\star}
<i>NGC 6652</i>	278.940	-32.991	10.0	-99.04	0.51	-5.506	-4.204	0.064	0.063	0.001	2.4	225
<i>NGC 6656</i> (M 22)	279.100	-23.905	3.2	-147.76	0.30	9.833	-5.557	0.047	0.047	0.008	11.8	4178
<i>Pal 8</i>	280.375	-19.826	12.8	-41.14	1.81	-2.031	-5.634	0.063	0.063	0.015	2.4	174
<i>NGC 6681</i> (M 70)	280.803	-32.292	9.0	216.62	0.84	1.458	-4.688	0.060	0.060	0.009	4.0	686
<i>NGC 6712</i>	283.268	-8.706	6.9	-107.45	0.29	3.341	-4.384	0.062	0.061	0.006	2.8	309
<i>NGC 6715</i> (M 54)	283.764	-30.480	26.5	143.06	0.56	-2.711	-1.355	0.058	0.058	0.009	7.9	854
<i>NGC 6717</i> (<i>Pal 9</i>)	283.775	-22.701	7.1	32.45	1.44	-3.106	-4.951	0.065	0.064	0.022	2.0	97
<i>NGC 6723</i>	284.888	-36.632	8.7	-94.18	0.26	1.033	-2.445	0.057	0.057	0.004	5.2	1824
<i>NGC 6749</i>	286.314	1.901	7.9	-58.44	0.96	-2.865	-5.987	0.061	0.061	0.011	4.3	395
<i>NGC 6752</i>	287.717	-59.985	4.0	-26.28	0.16	-3.170	-4.043	0.042	0.042	0.004	12.3	10850
<i>NGC 6760</i>	287.800	1.030	7.4	-0.42	1.63	-1.129	-3.561	0.060	0.059	0.009	4.2	572
<i>NGC 6779</i> (M 56)	289.148	30.183	9.4	-136.97	0.45	-2.020	1.644	0.059	0.059	0.004	4.5	811
<i>Terzan 7</i>	289.433	-34.658	22.8	159.45	0.14	-2.999	-1.586	0.068	0.067	0.032	1.5	93
<i>Pal 10</i>	289.509	18.572	5.9	-31.70	0.23	-4.250	-6.924	0.064	0.064	0.005	2.2	246
<i>Arp 2</i>	292.184	-30.356	28.6	123.01	0.33	-2.381	-1.510	0.067	0.066	0.013	1.9	137
<i>NGC 6809</i> (M 55)	294.999	-30.965	5.4	174.40	0.24	-3.420	-9.269	0.050	0.050	0.010	8.8	4224
<i>Terzan 8</i>	295.435	-33.999	26.3	148.53	0.17	-2.472	-1.556	0.062	0.060	-0.006	2.7	251
<i>Pal 11</i>	296.310	-8.007	13.4	-67.64	0.76	-1.821	-4.934	0.066	0.064	0.027	1.8	174
<i>NGC 6838</i> (M 71)	298.444	18.779	4.0	-22.27	0.19	-3.415	-2.614	0.054	0.054	0.005	5.1	2676
<i>NGC 6864</i> (M 75)	301.520	-21.921	20.9	-189.08	1.12	-0.559	-2.798	0.062	0.061	0.009	2.8	224
<i>NGC 6934</i>	308.547	7.404	15.6	-406.22	0.73	-2.636	-4.667	0.060	0.060	0.009	4.0	336
<i>NGC 6981</i> (M 72)	313.365	-12.537	17.0	-331.39	1.47	-1.233	-3.290	0.062	0.061	0.016	3.0	350
<i>NGC 7006</i>	315.372	16.187	41.2	-383.47	0.73	-0.102	-0.569	0.067	0.068	-0.013	2.0	137
<i>NGC 7078</i> (M 15)	322.493	12.167	10.4	-106.76	0.25	-0.643	-3.763	0.051	0.051	0.001	9.9	2198
<i>NGC 7089</i> (M 2)	323.363	-0.823	11.5	-3.72	0.34	3.518	-2.145	0.054	0.054	0.013	6.2	1369
<i>NGC 7099</i> (M 30)	325.092	-23.180	8.1	-185.19	0.17	-0.694	-7.271	0.055	0.054	0.031	5.8	1414
<i>Pal 12</i>	326.662	-21.253	19.0	27.91	0.28	-3.249	-3.303	0.067	0.067	0.034	1.5	99
<i>Pal 13</i>	346.685	12.772	26.0	25.87	0.27	1.615	0.142	0.101	0.089	0.016	0.8	34
<i>NGC 7492</i>	347.111	-15.611	26.3	-176.70	0.27	0.799	-2.273	0.065	0.064	0.009	1.5	125

Figure C1. Colour–magnitude diagrams (left column), spatial distribution (middle column) and PM distribution (right column) of stars in individual clusters. Membership probability is marked by colour (red – likely members, gray – field stars); the number of members and the total number of stars in the sample is given in brackets. Green crosses indicate likely member stars listed in other papers. Isochrone tracks for the assumed age, metallicity and distance are plotted in the left panel by blue dots (PARSEC, [Bressan et al. 2012](#)) and green dots (MIST, [Choi et al. 2016](#)), with extinction and reddening computed using the coefficients from Table 1 in [Babusiaux et al. \(2018\)](#). Cyan histogram in the central panel shows the distribution of membership probabilities p in 10 bins (leftmost – $p \leq 10\%$, rightmost – $p \geq 90\%$); a strongly bimodal distribution indicates a good separation of cluster and field stars in the PM space. Green dot-dashed circle shows the half-light radius from [Baumgardt et al. \(2019\)](#), and blue dashed circle – the scale radius R_{scale} of the Plummer profile of member stars in the filtered *Gaia* catalogue, which is typically larger than the true half-light radius because the catalogue is incomplete in the central regions. Blue ellipse in the right panel indicates the uncertainty on the mean PM, summed in quadrature with the internal PM dispersion σ_{μ} . Green crosses indicate the mean PM measured by *HST*, and pluses – by [H18](#). The plots for all 150 clusters are presented as supplementary material.

Figure C1 – continued

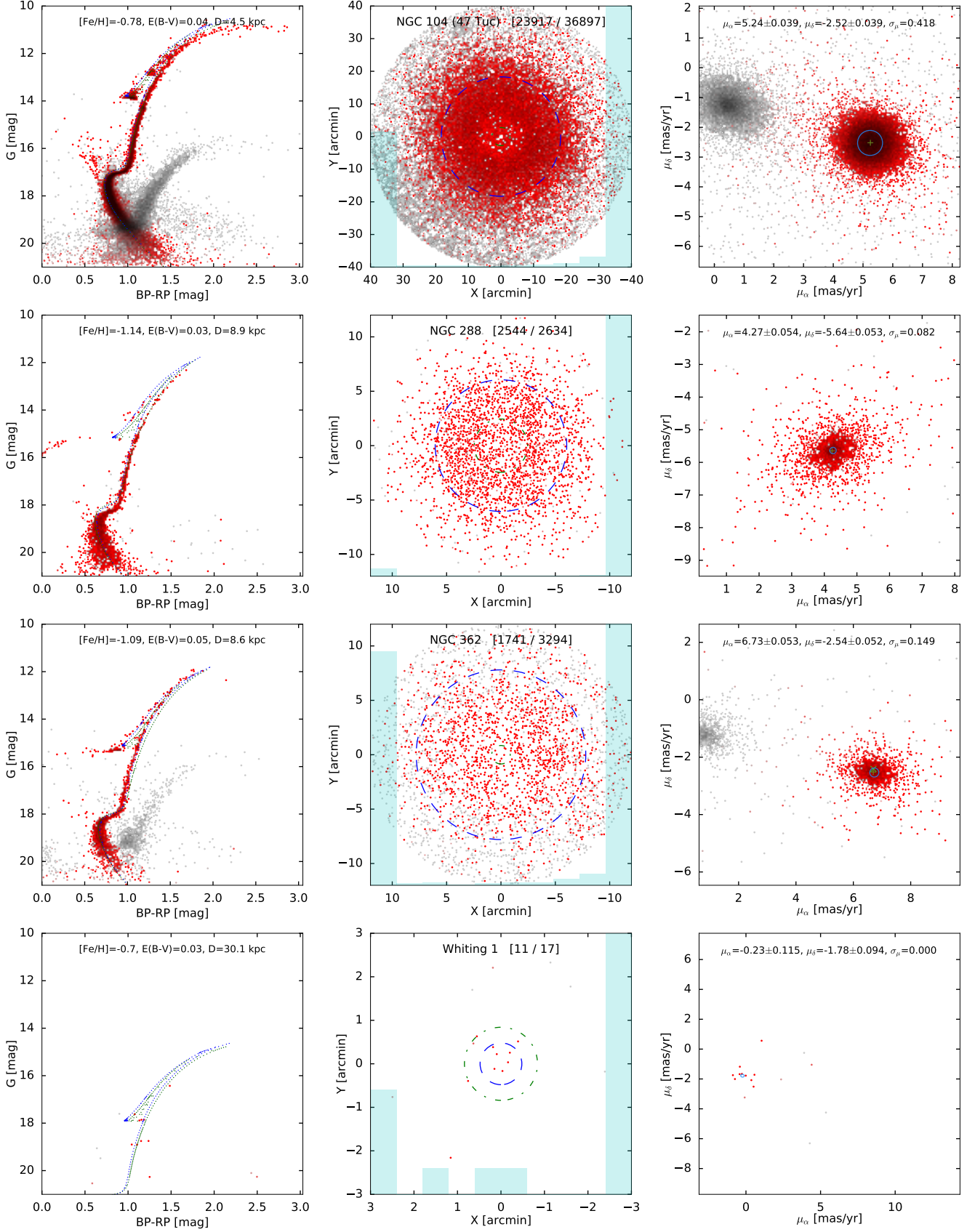


Figure C1 – *continued*

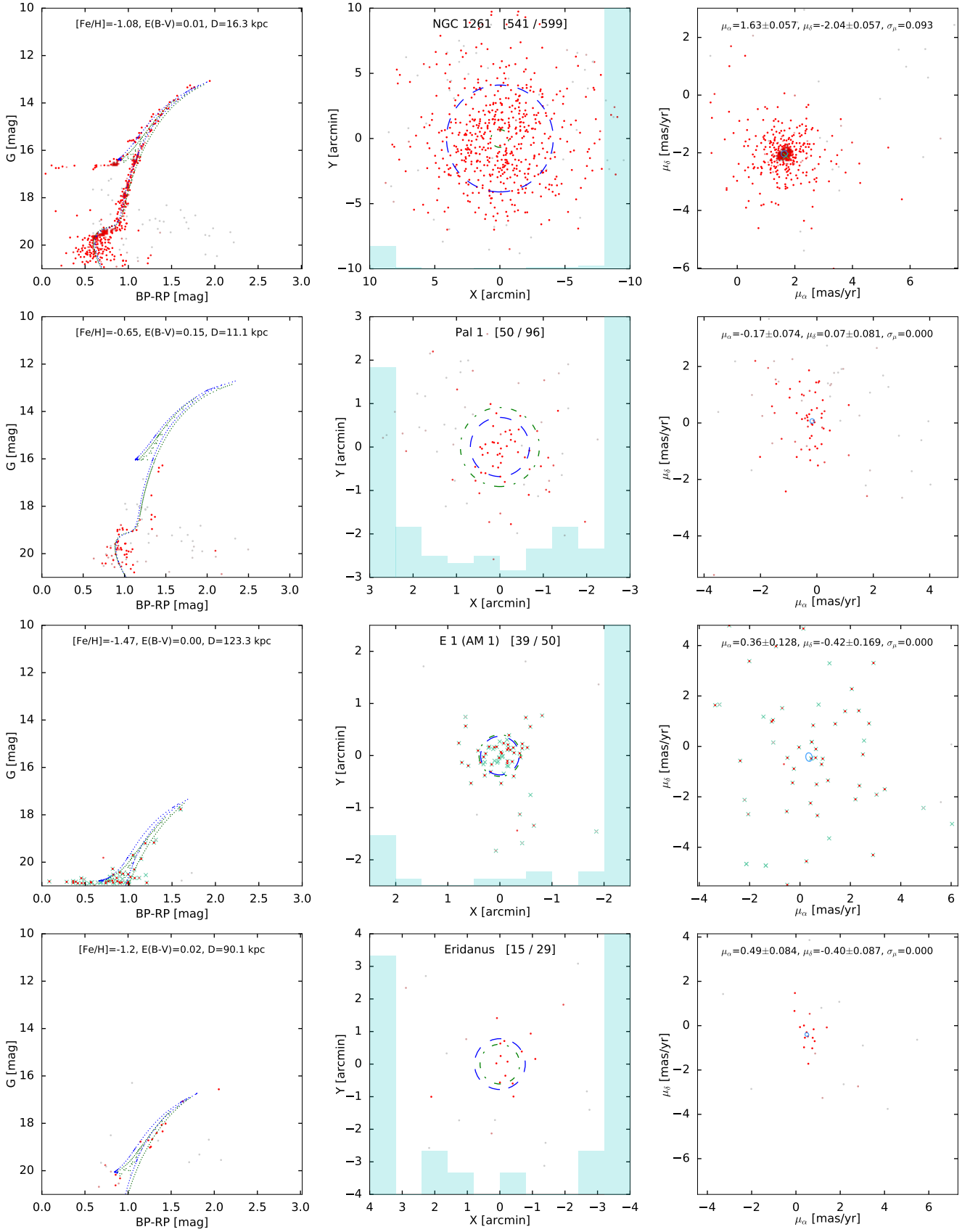


Figure C1 – continued

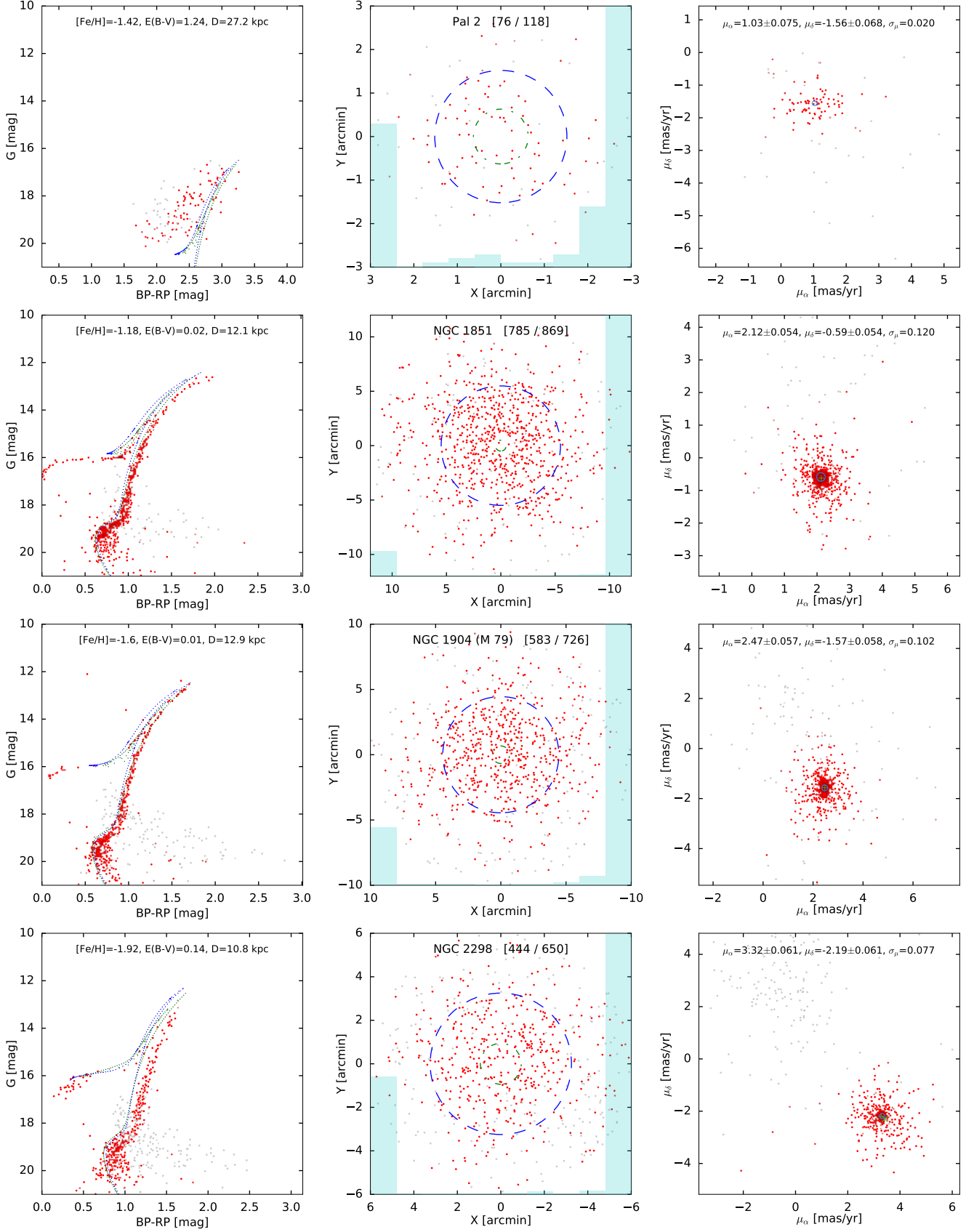


Figure C1 – *continued*

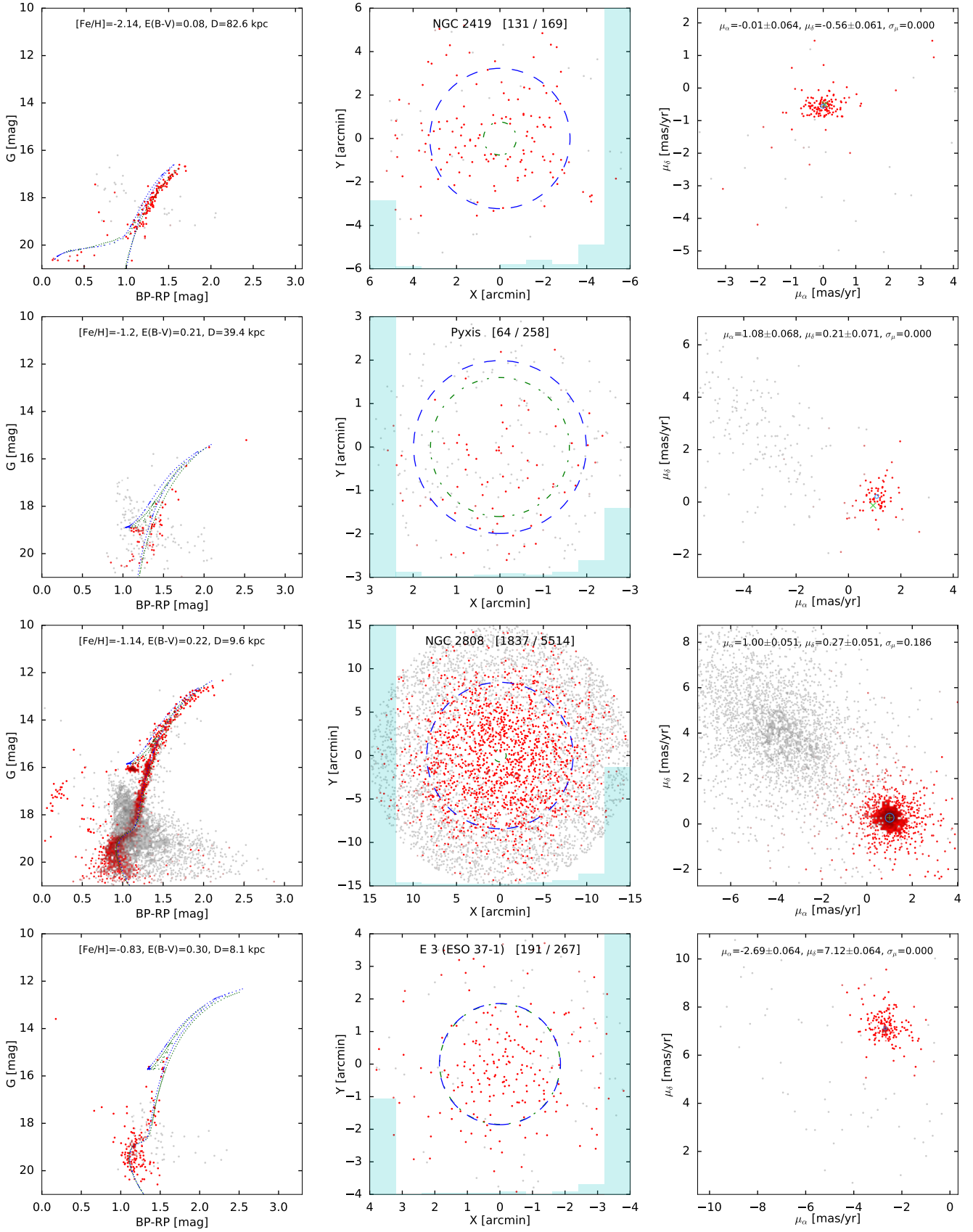


Figure C1 – continued

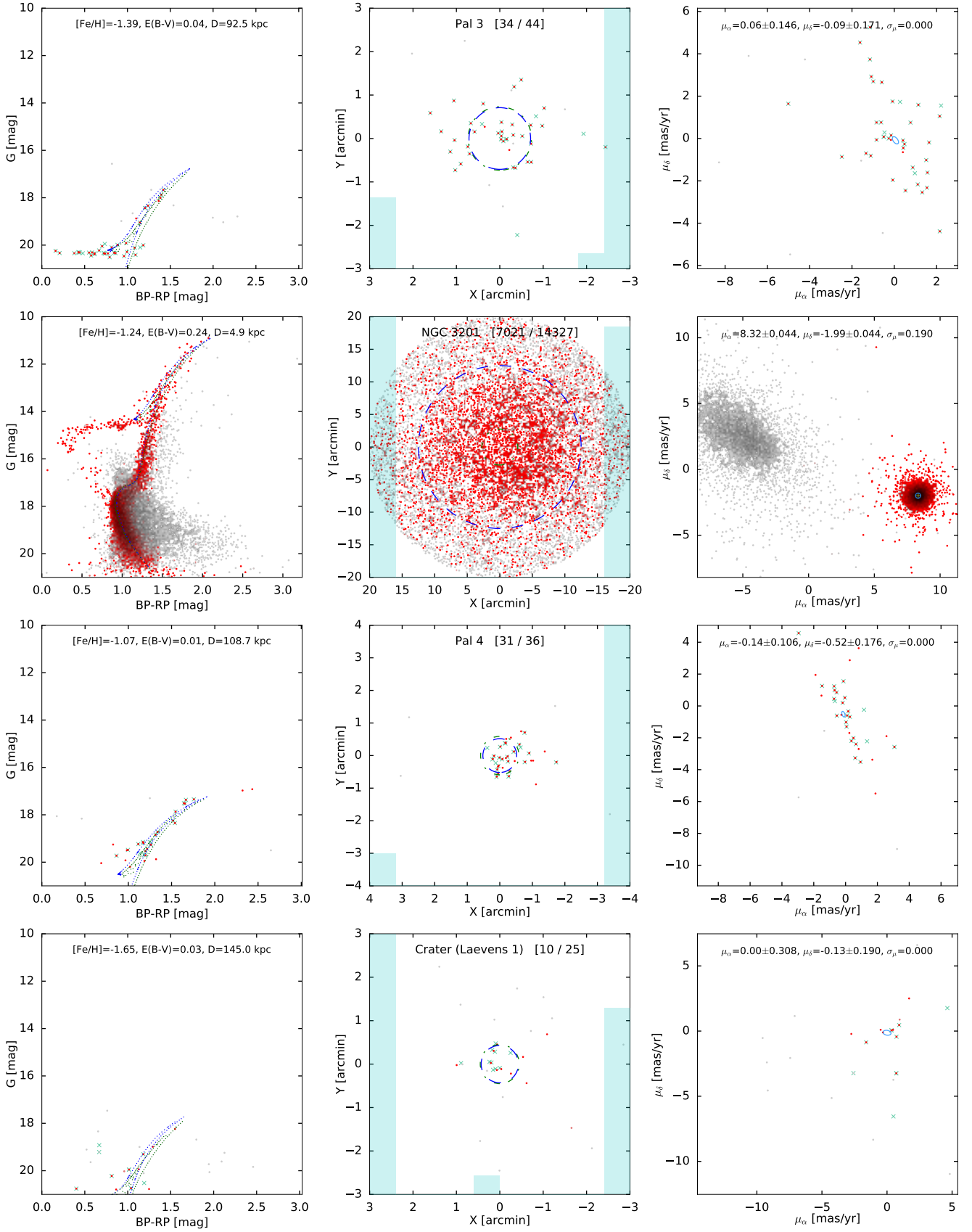


Figure C1 – *continued*

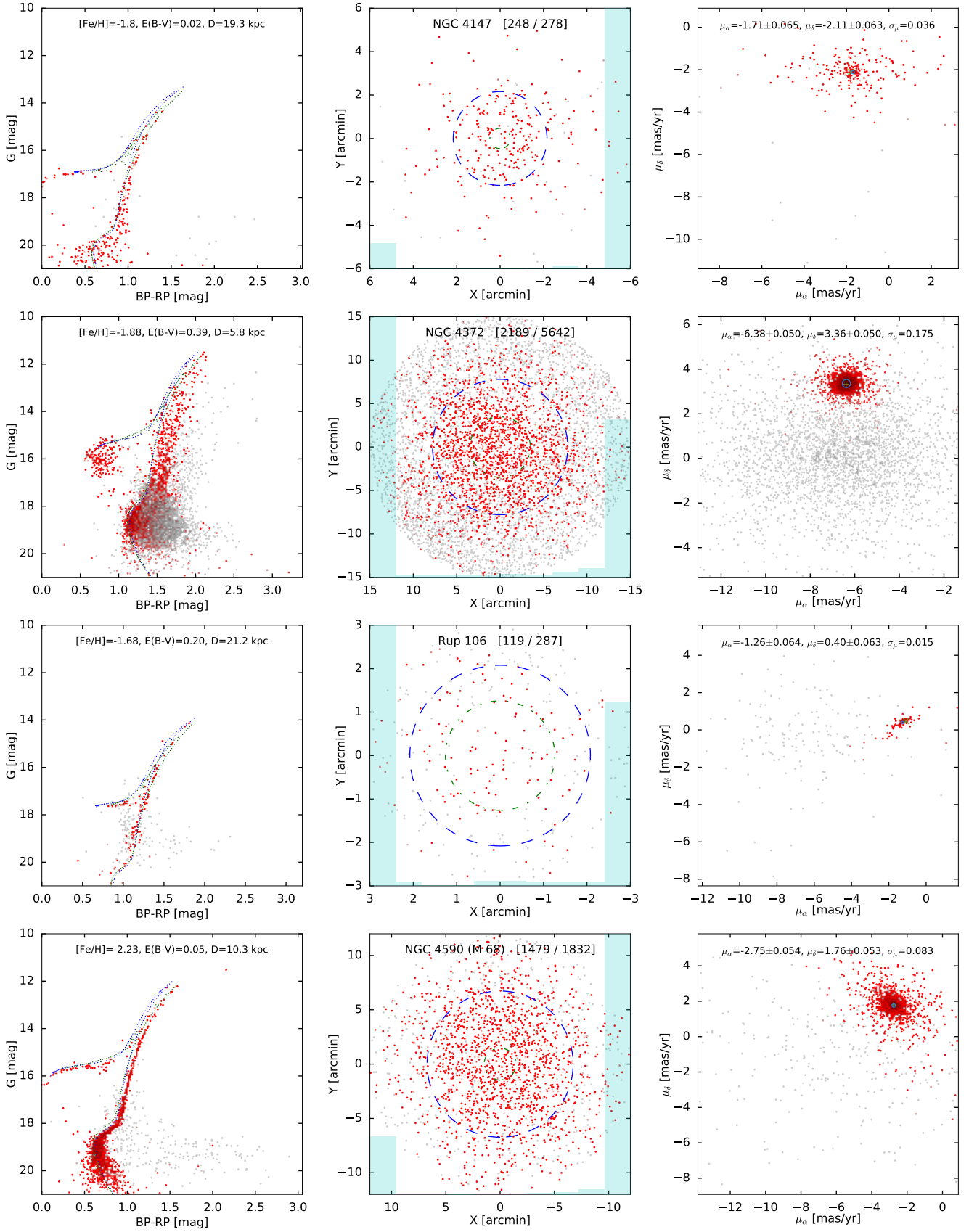


Figure C1 – continued

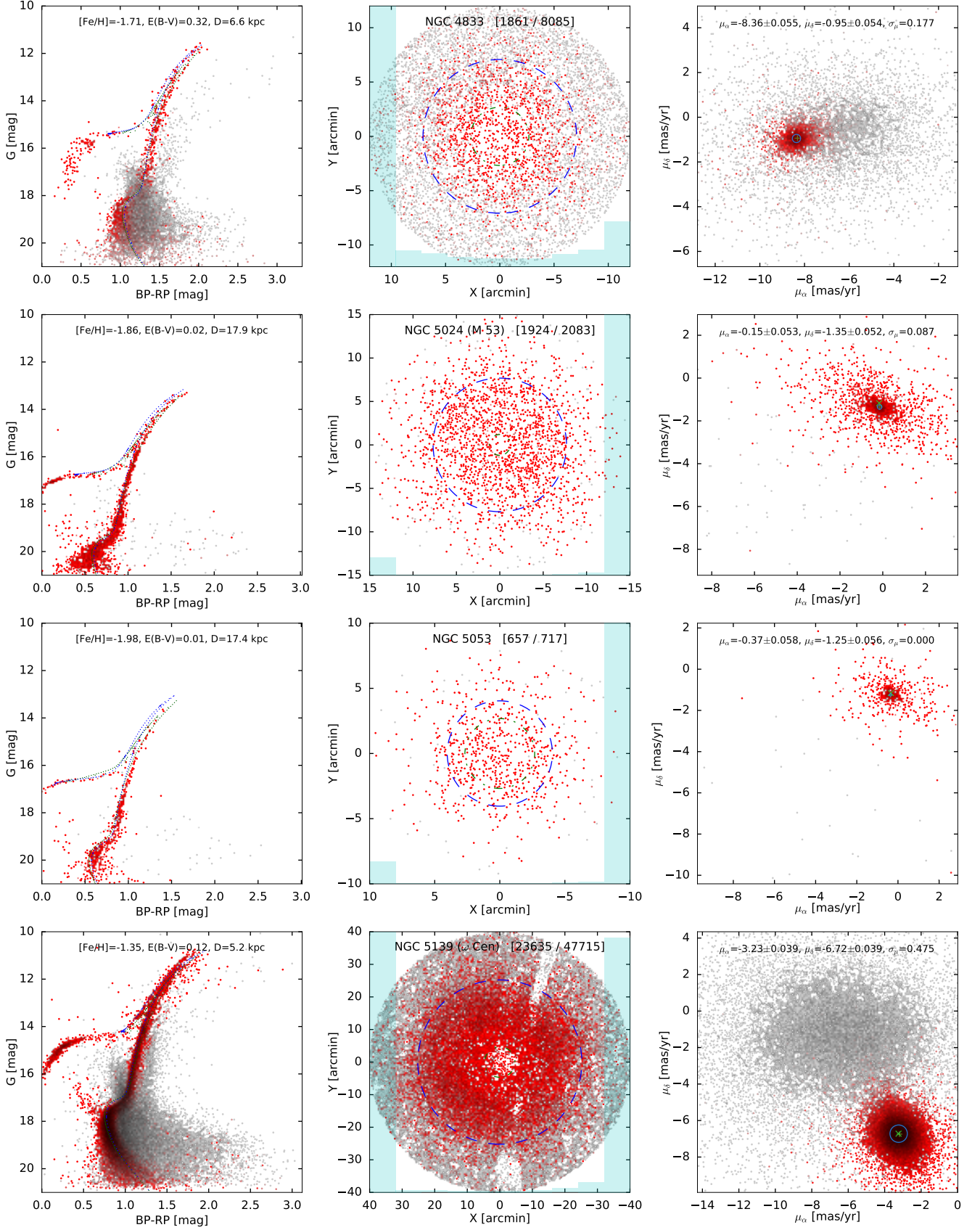


Figure C1 – *continued*

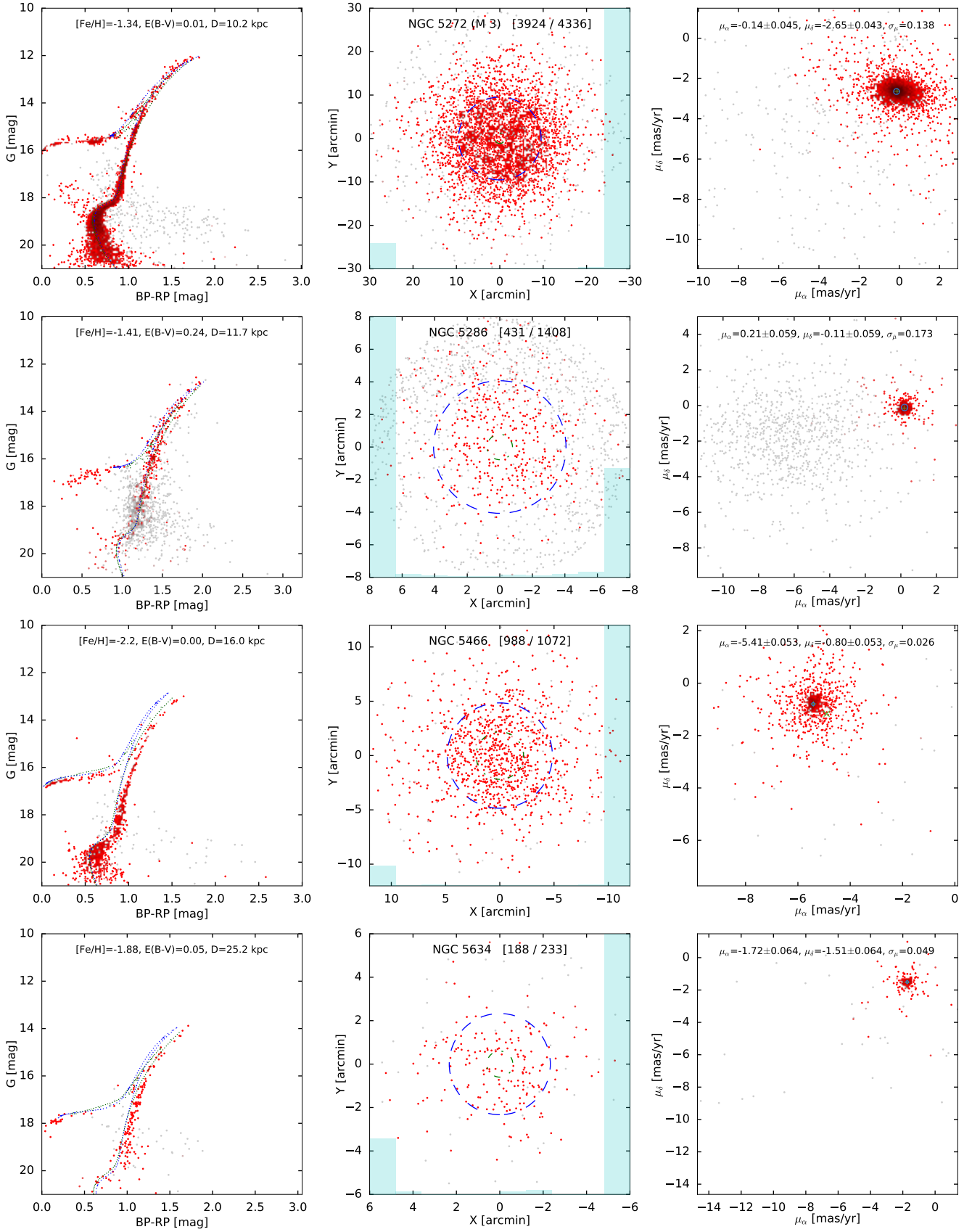


Figure C1 – continued

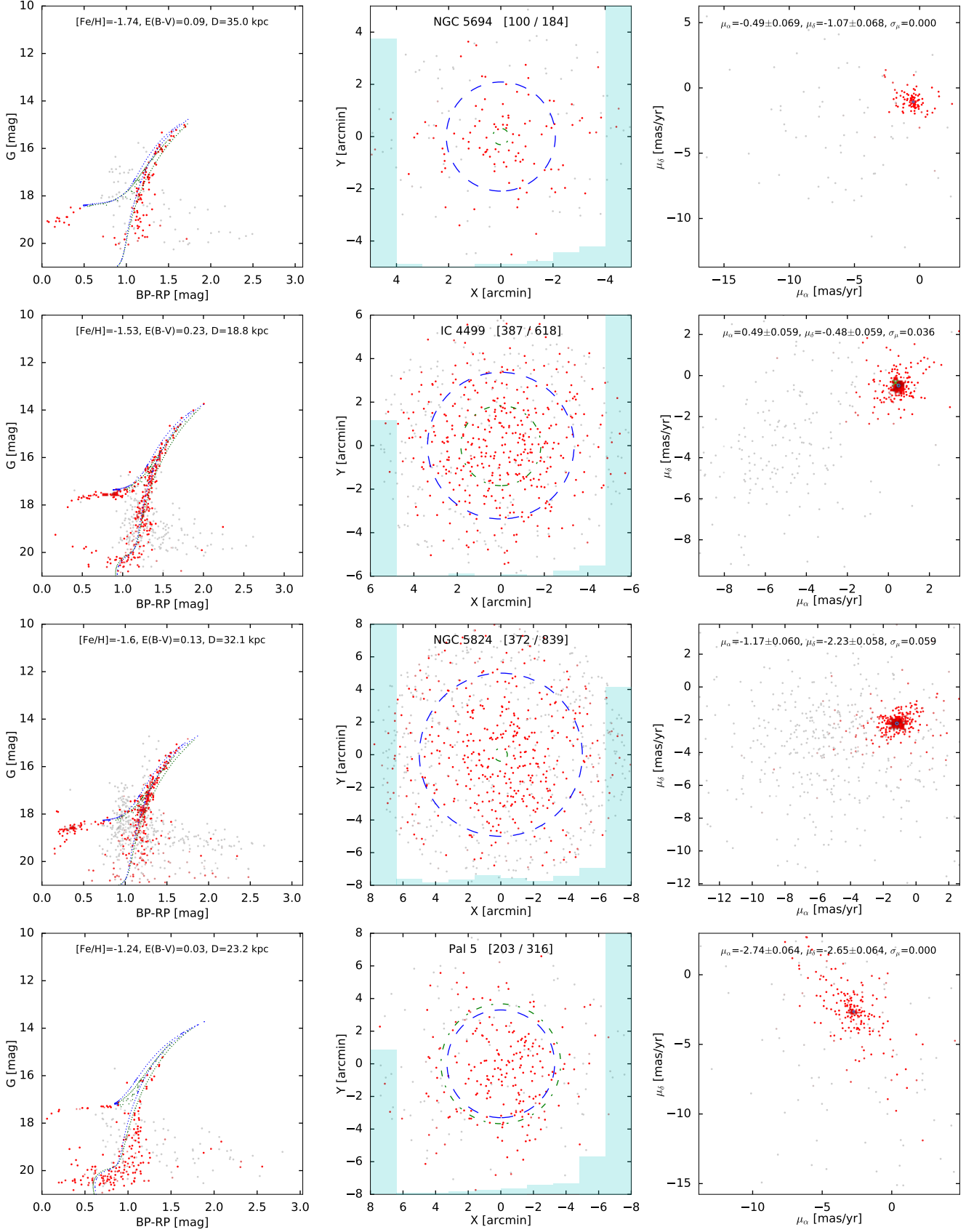


Figure C1 – *continued*

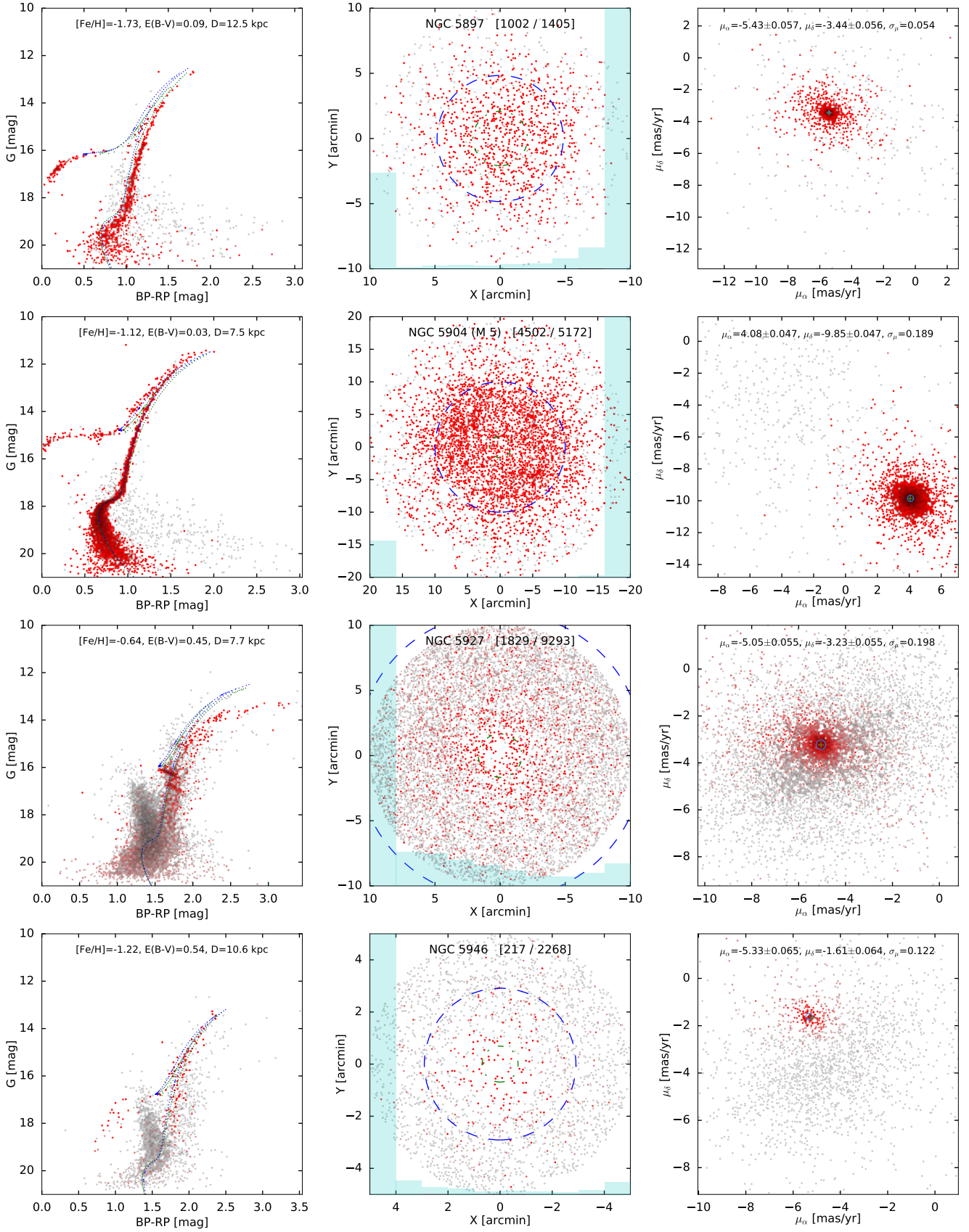


Figure C1 – continued

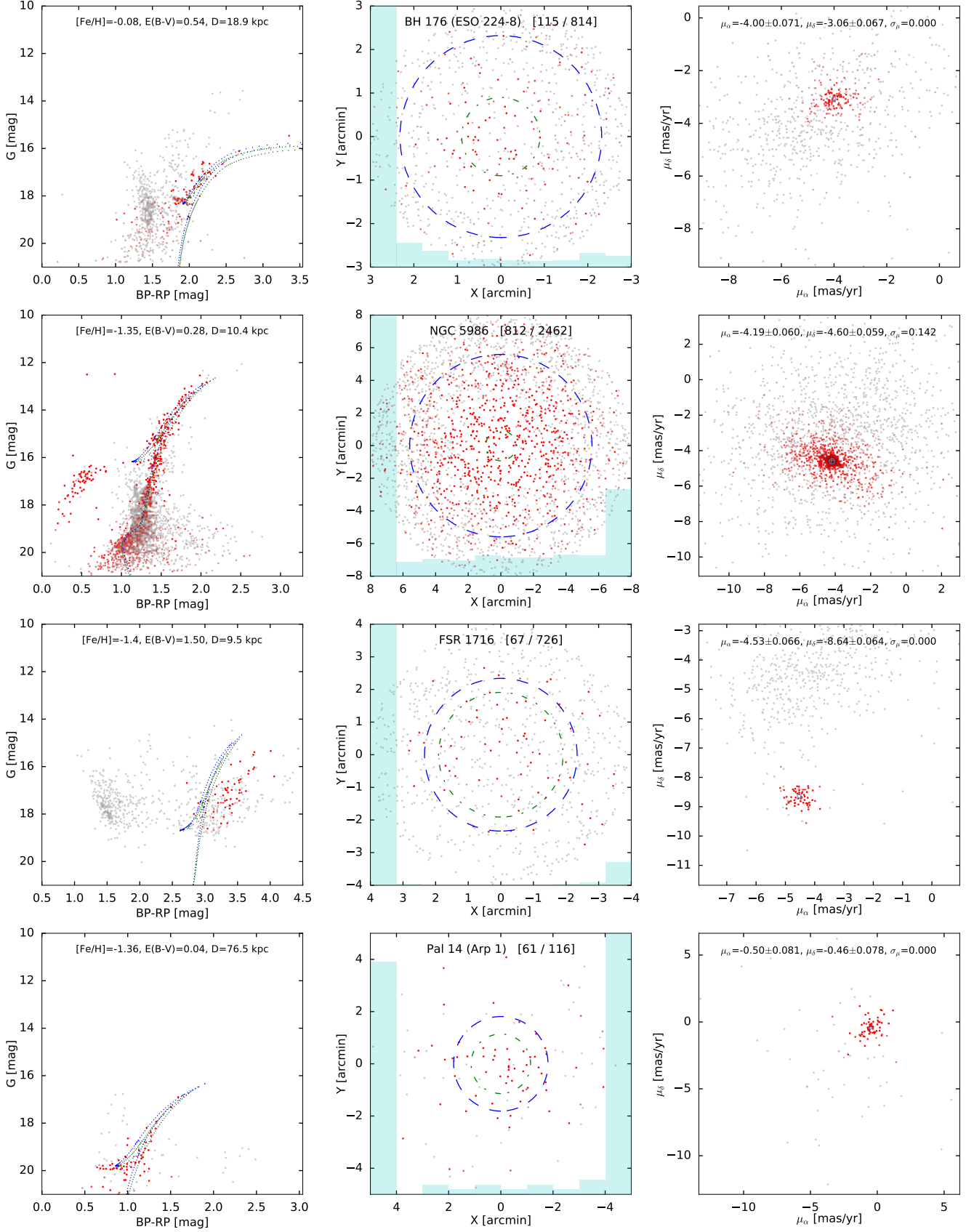


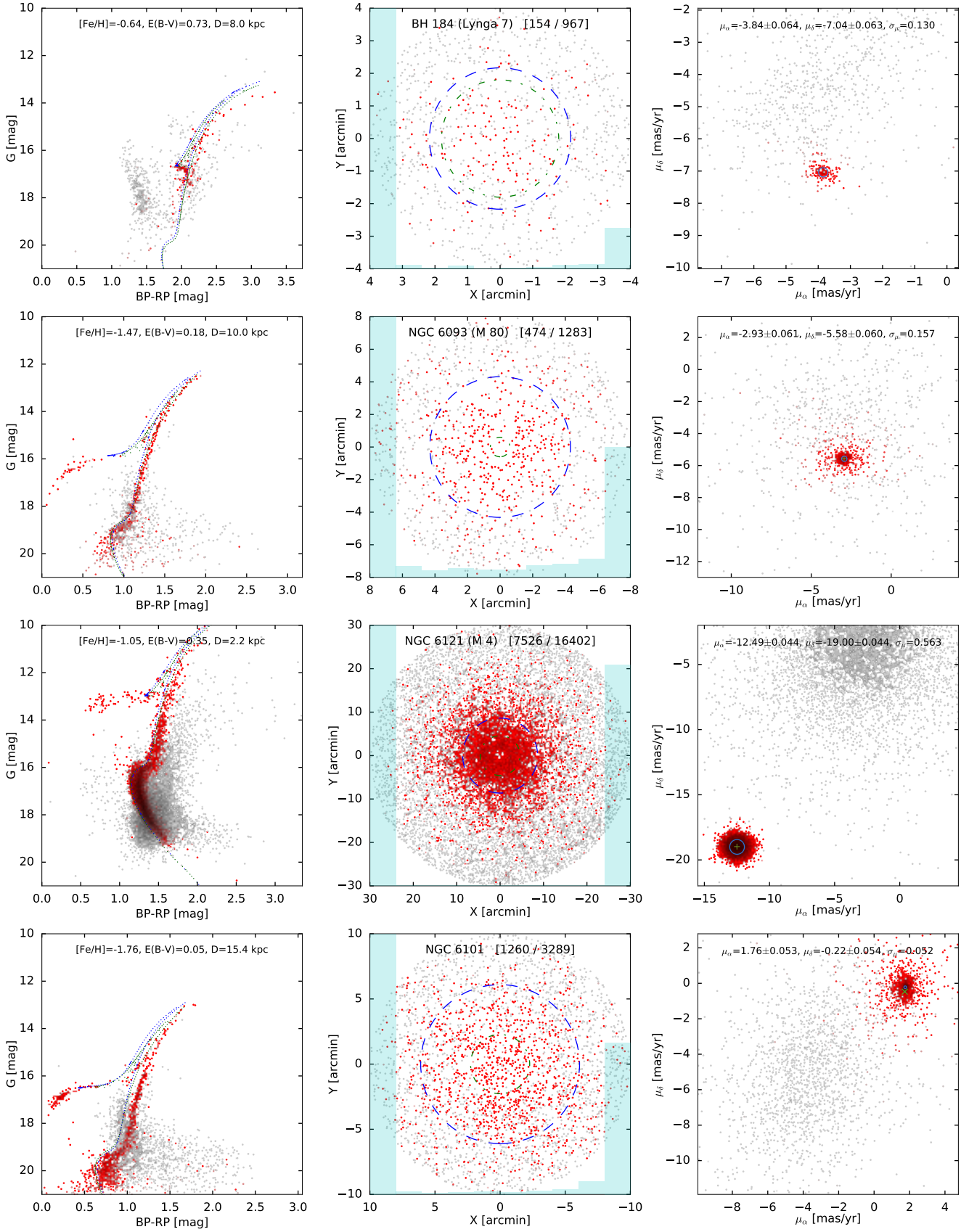
Figure C1 – *continued*

Figure C1 – continued

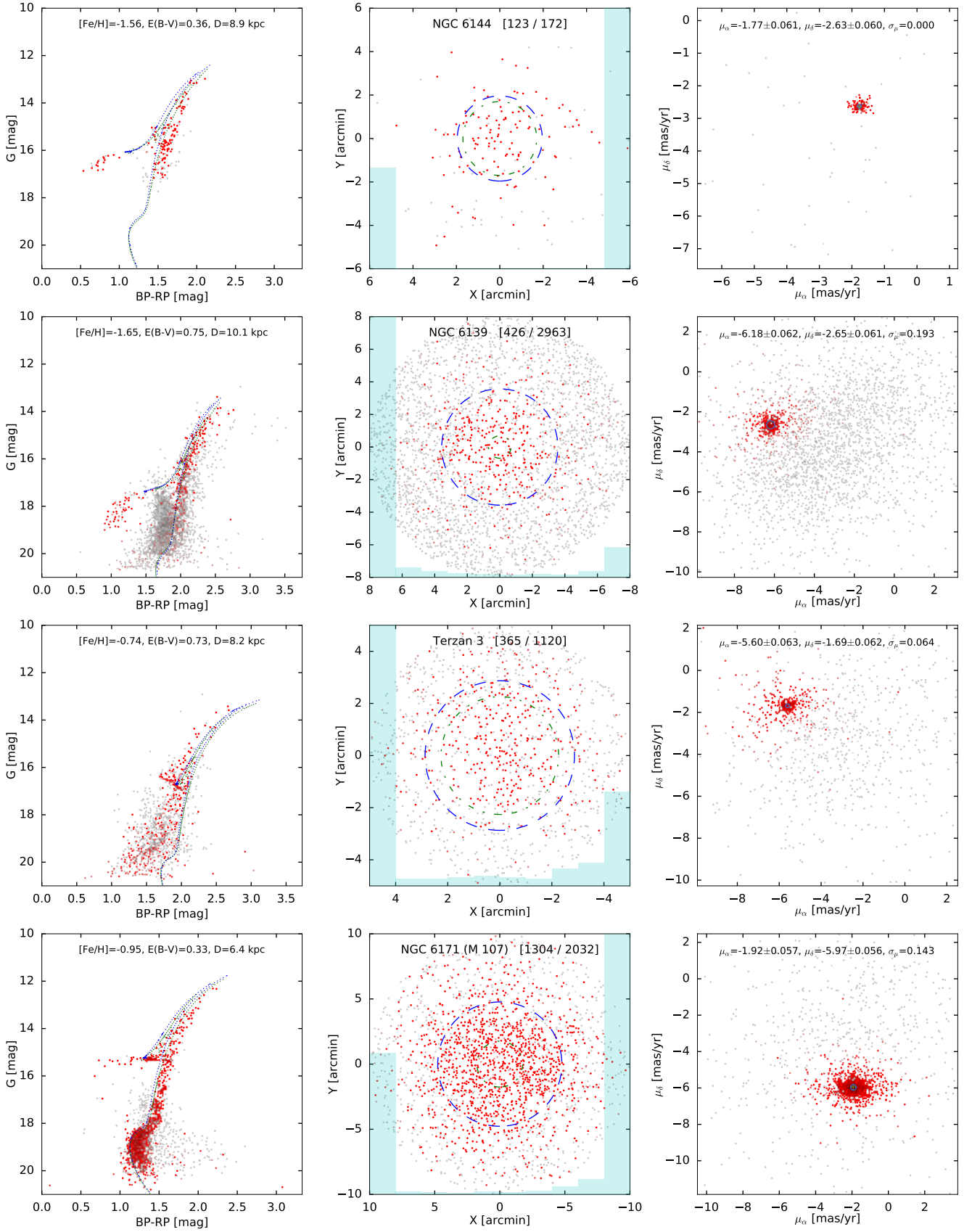


Figure C1 – *continued*

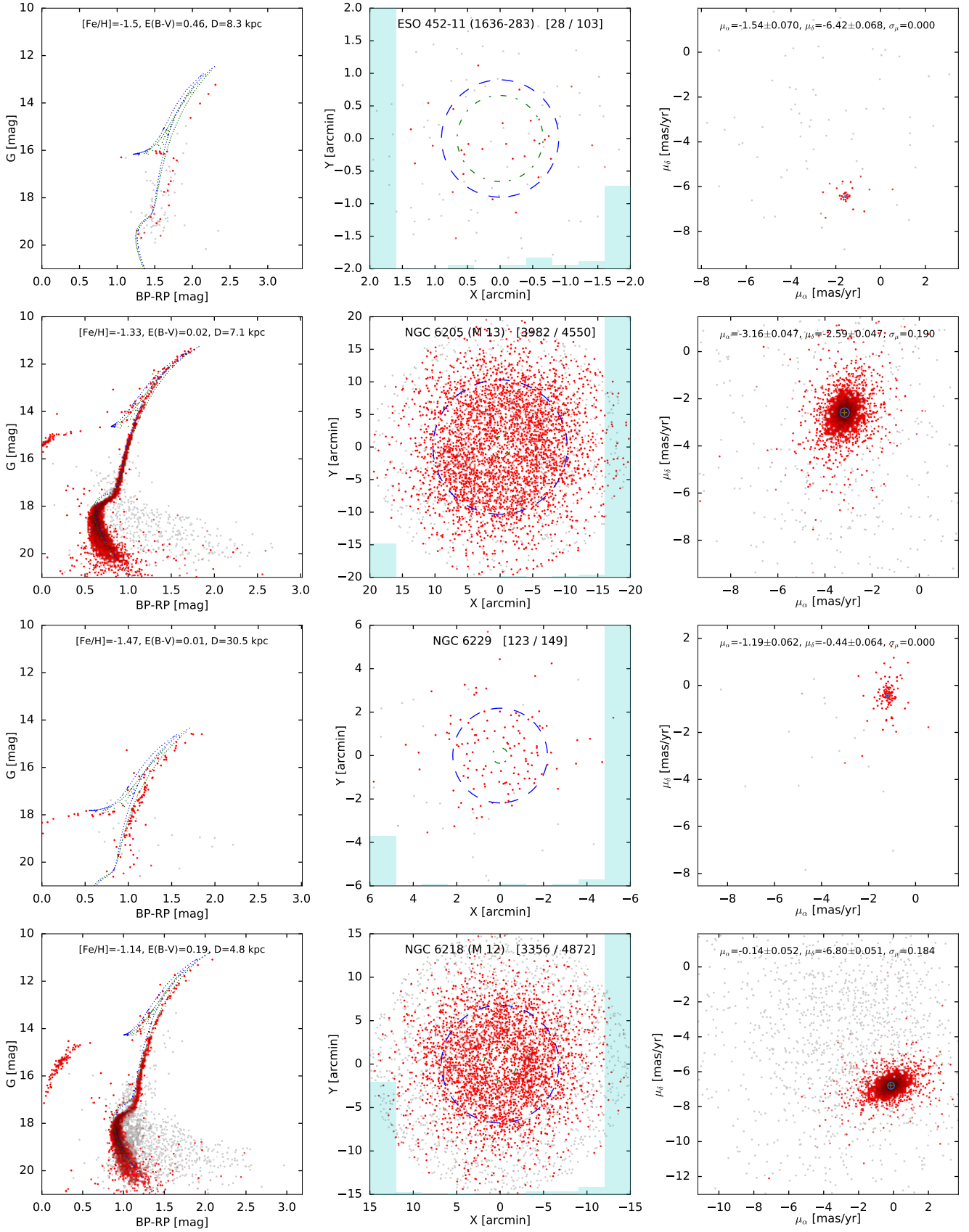


Figure C1 – continued

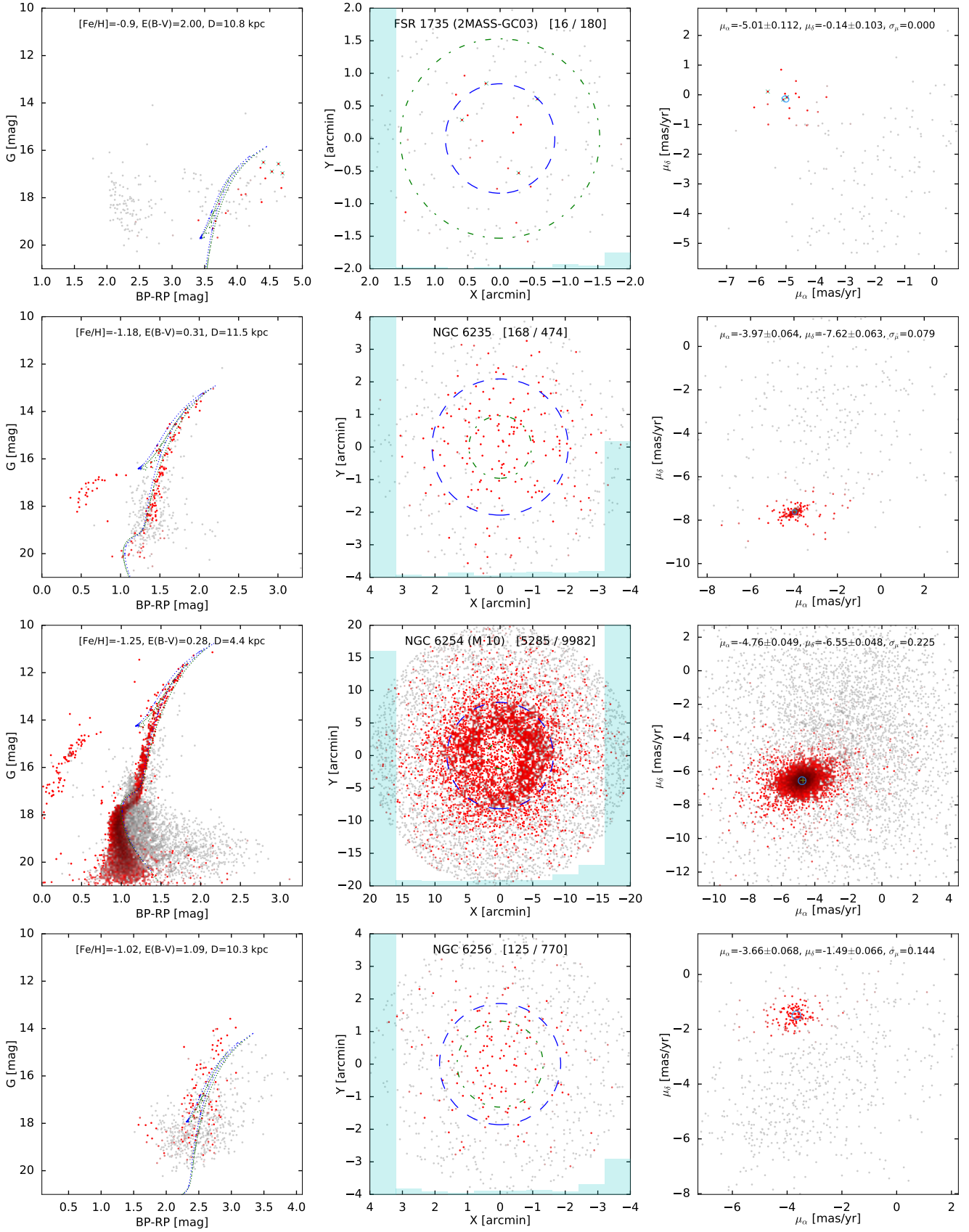


Figure C1 – *continued*

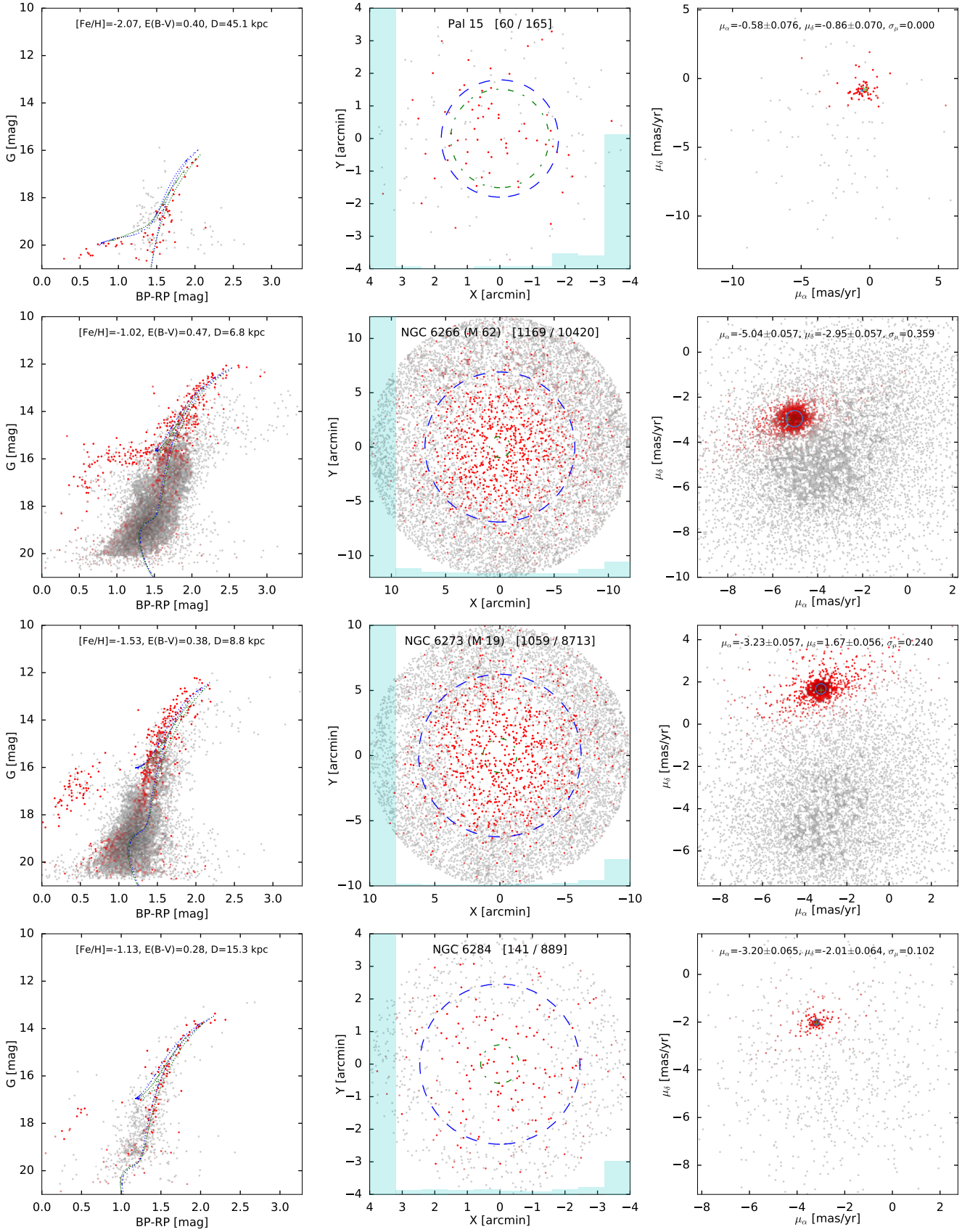


Figure C1 – continued

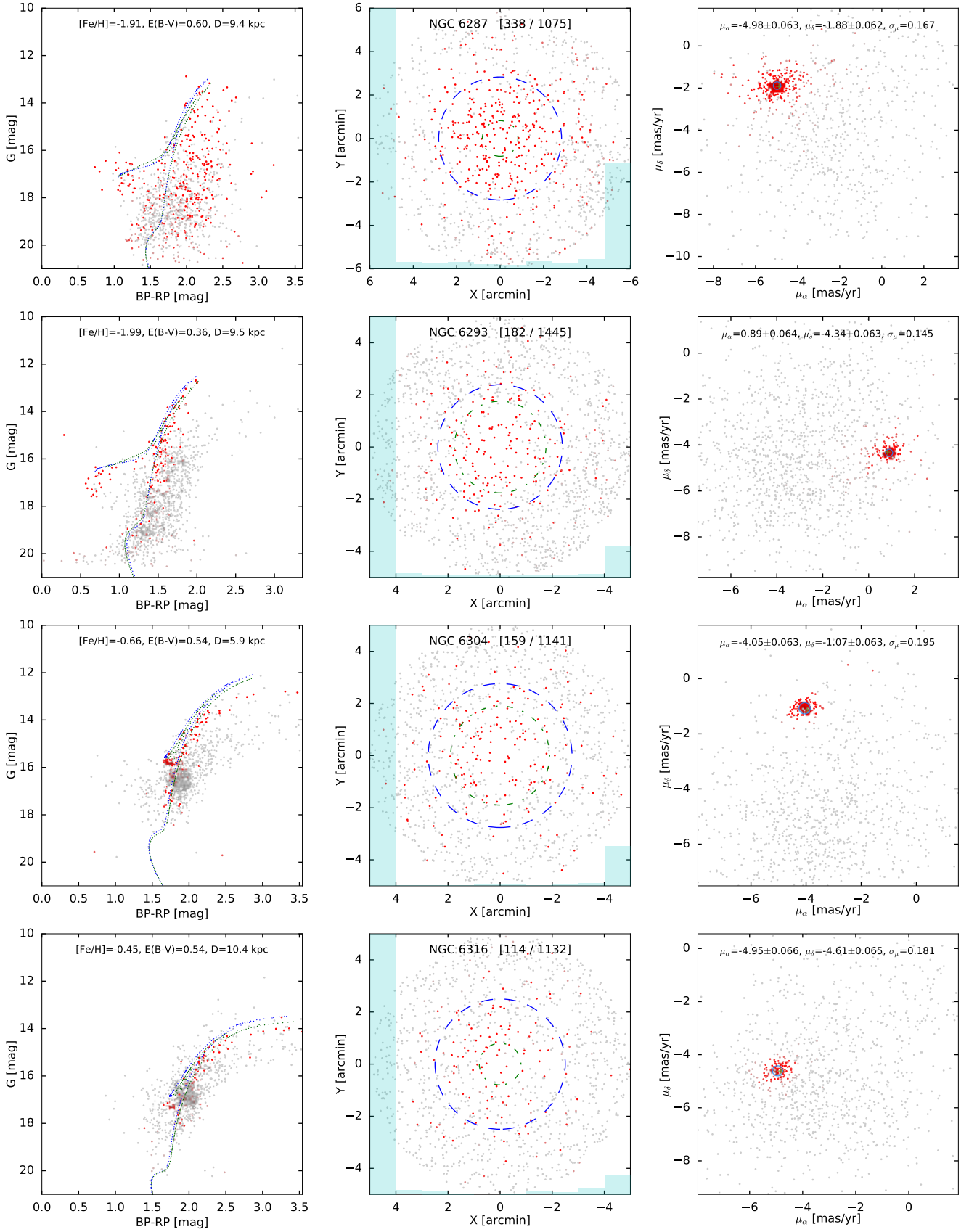


Figure C1 – *continued*

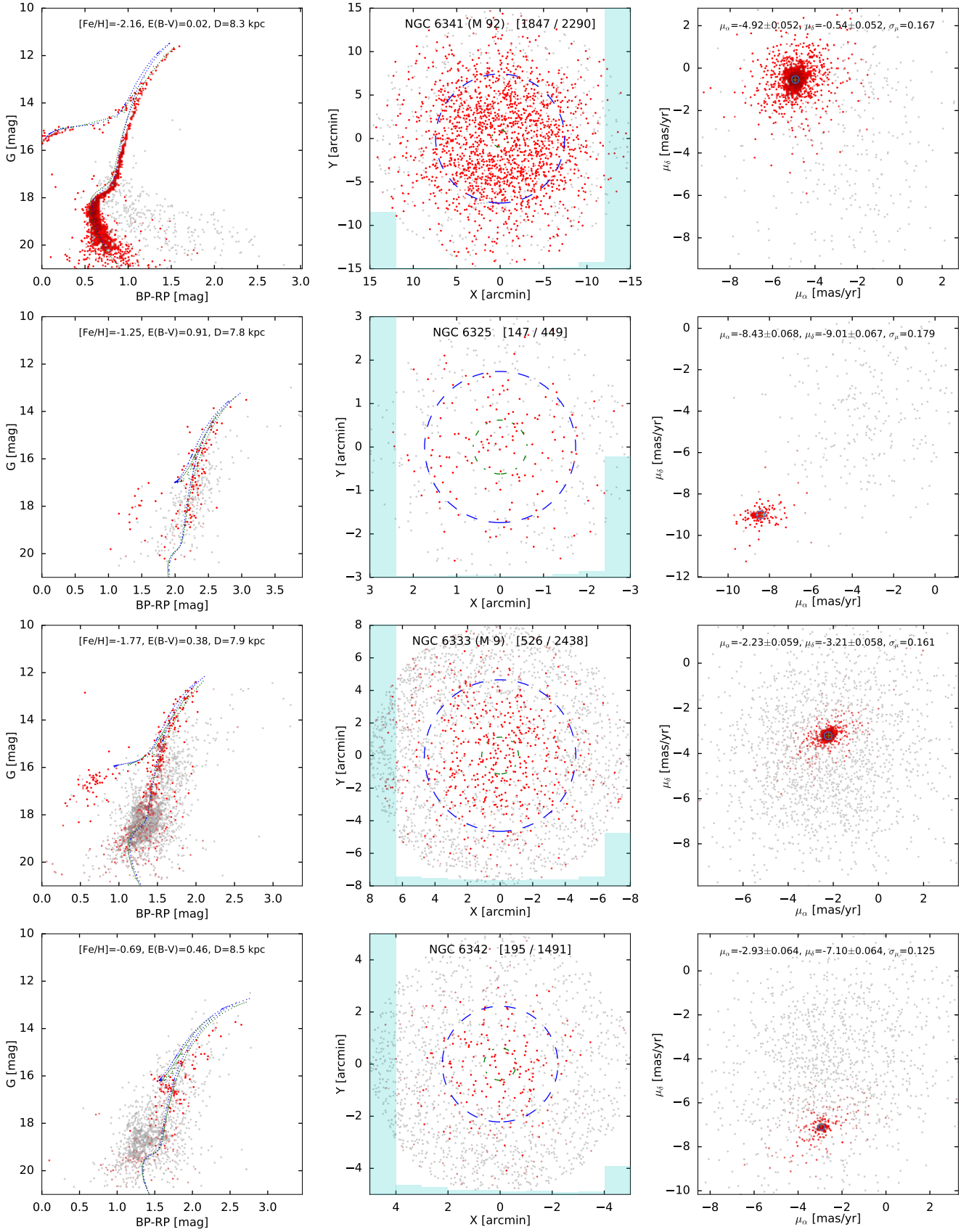


Figure C1 – continued

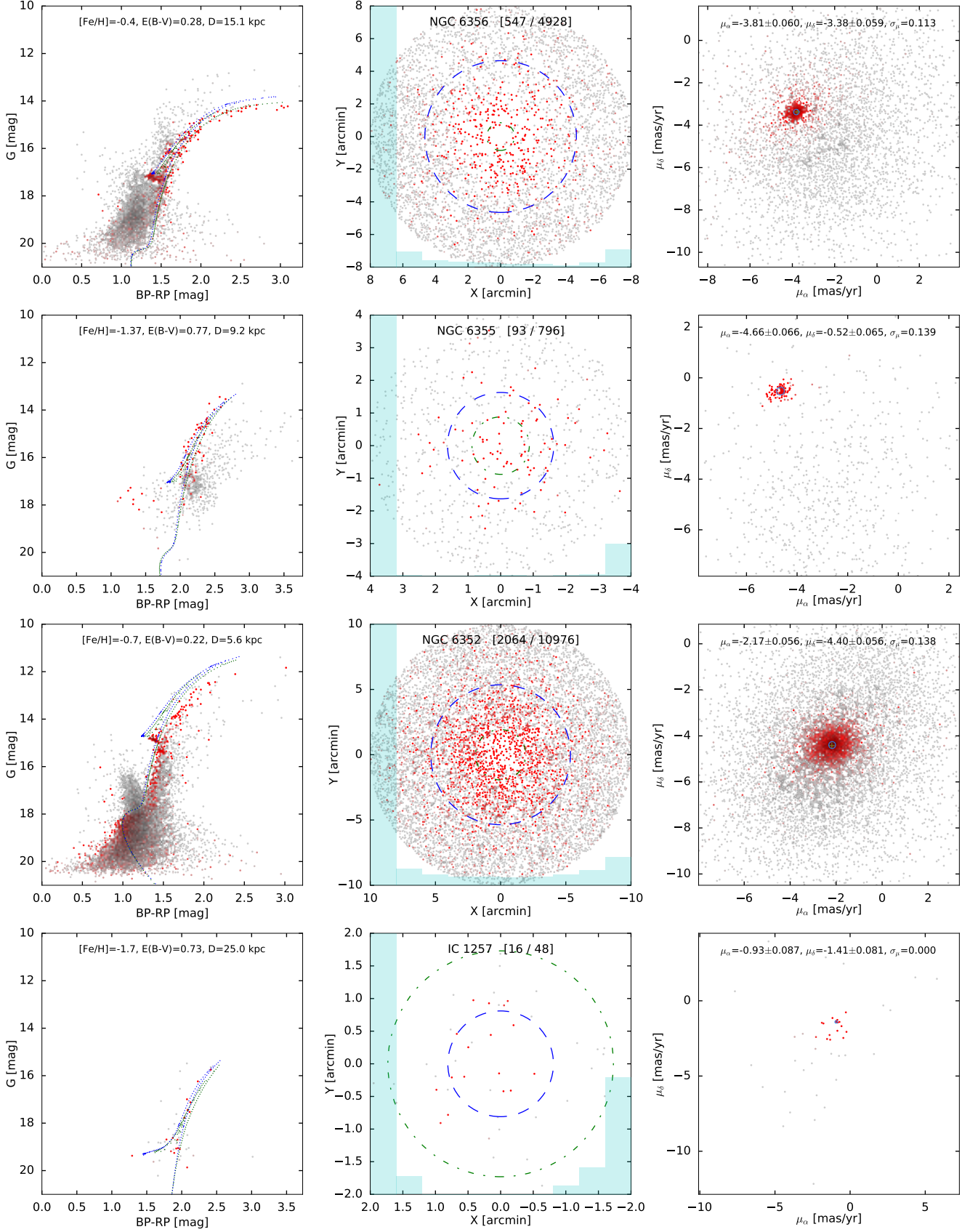


Figure C1 – *continued*

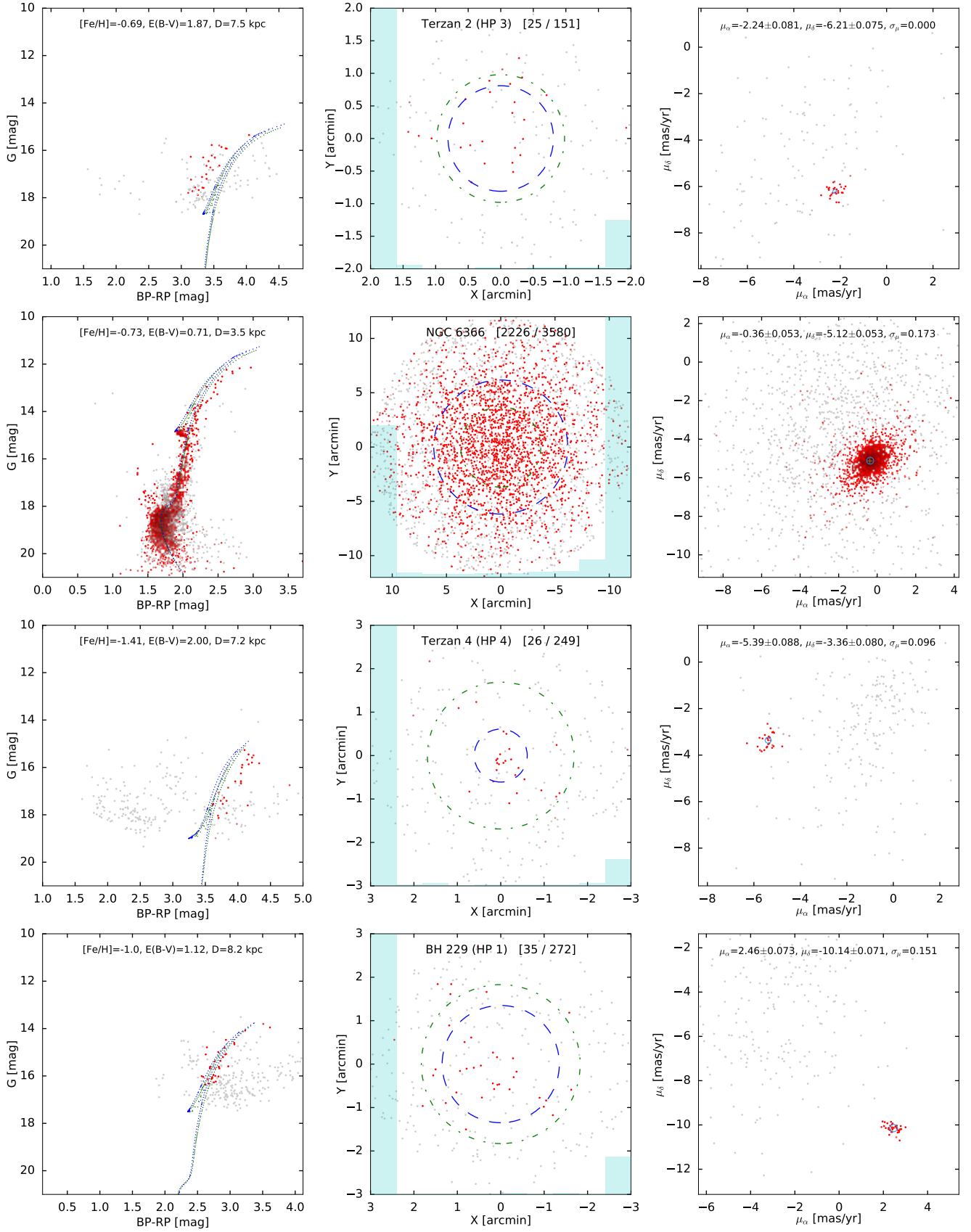


Figure C1 – continued

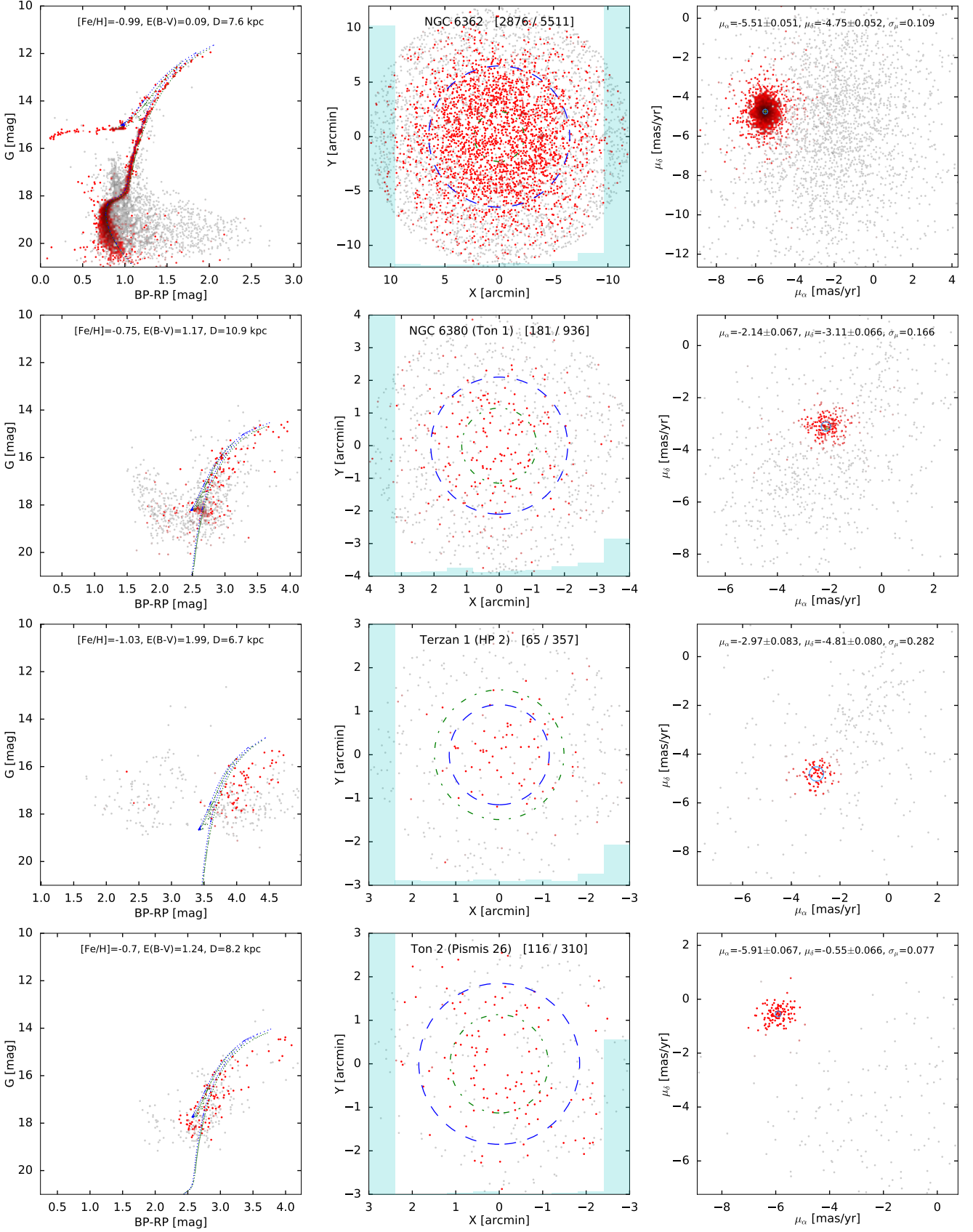


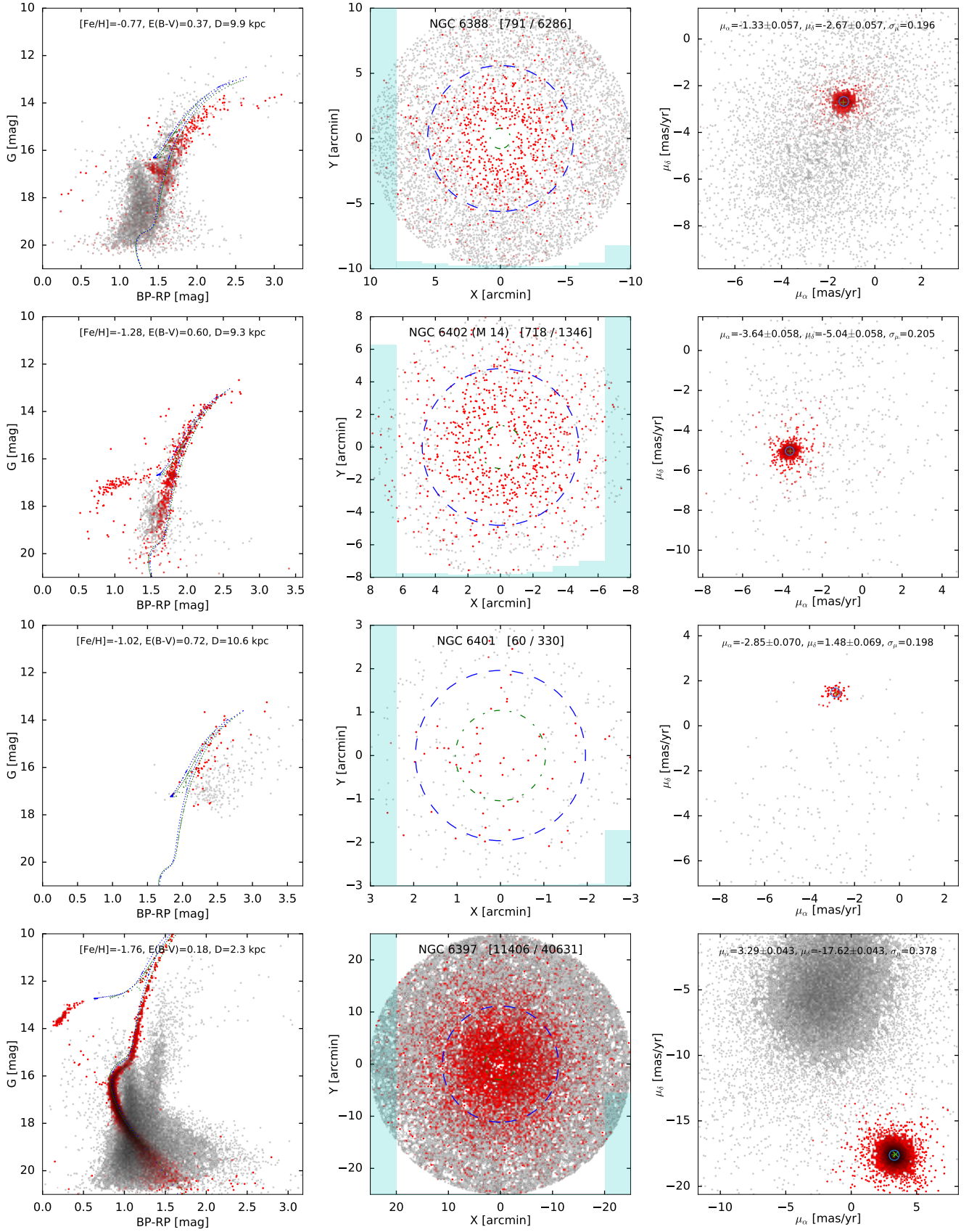
Figure C1 – *continued*

Figure C1 – continued

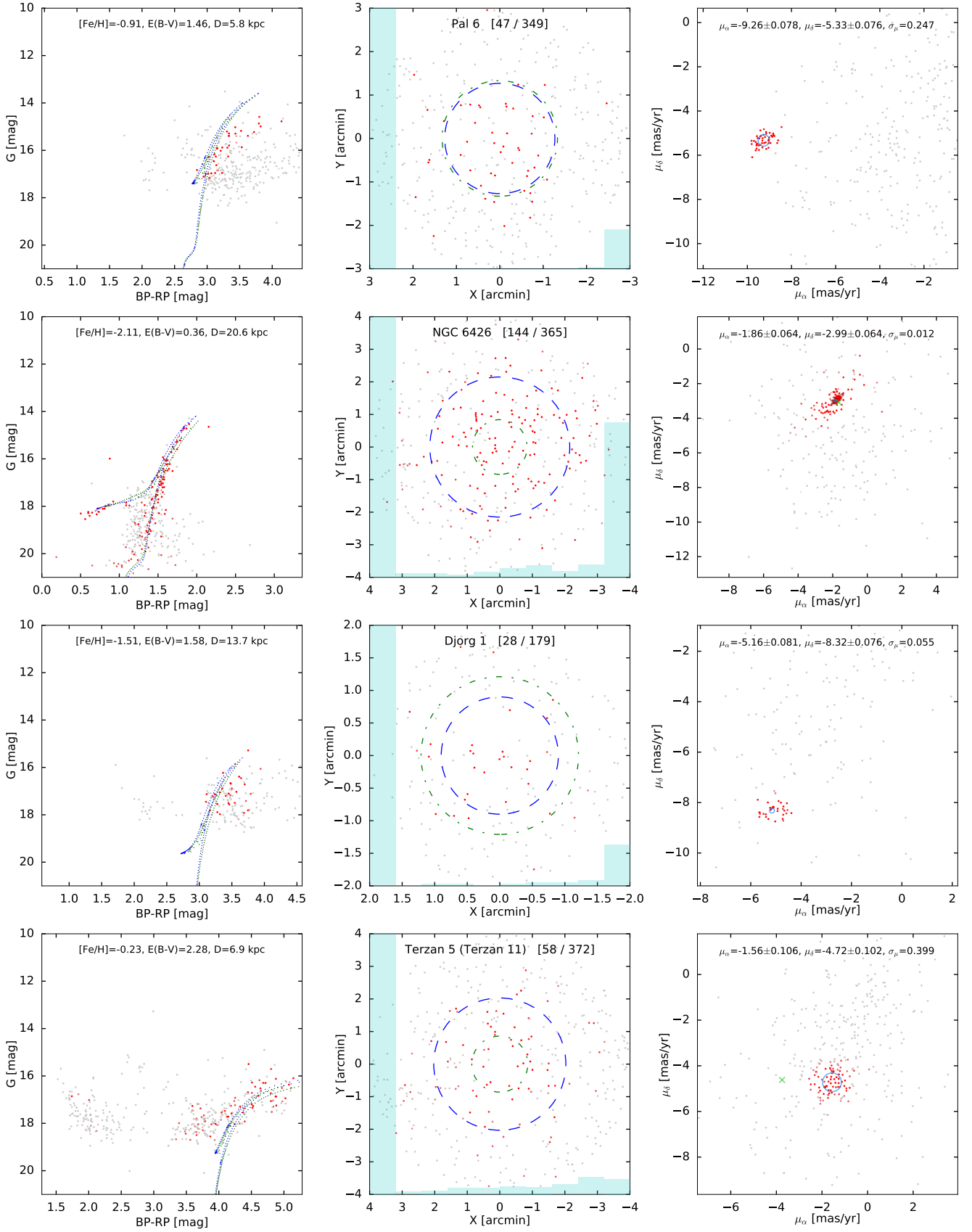


Figure C1 – *continued*

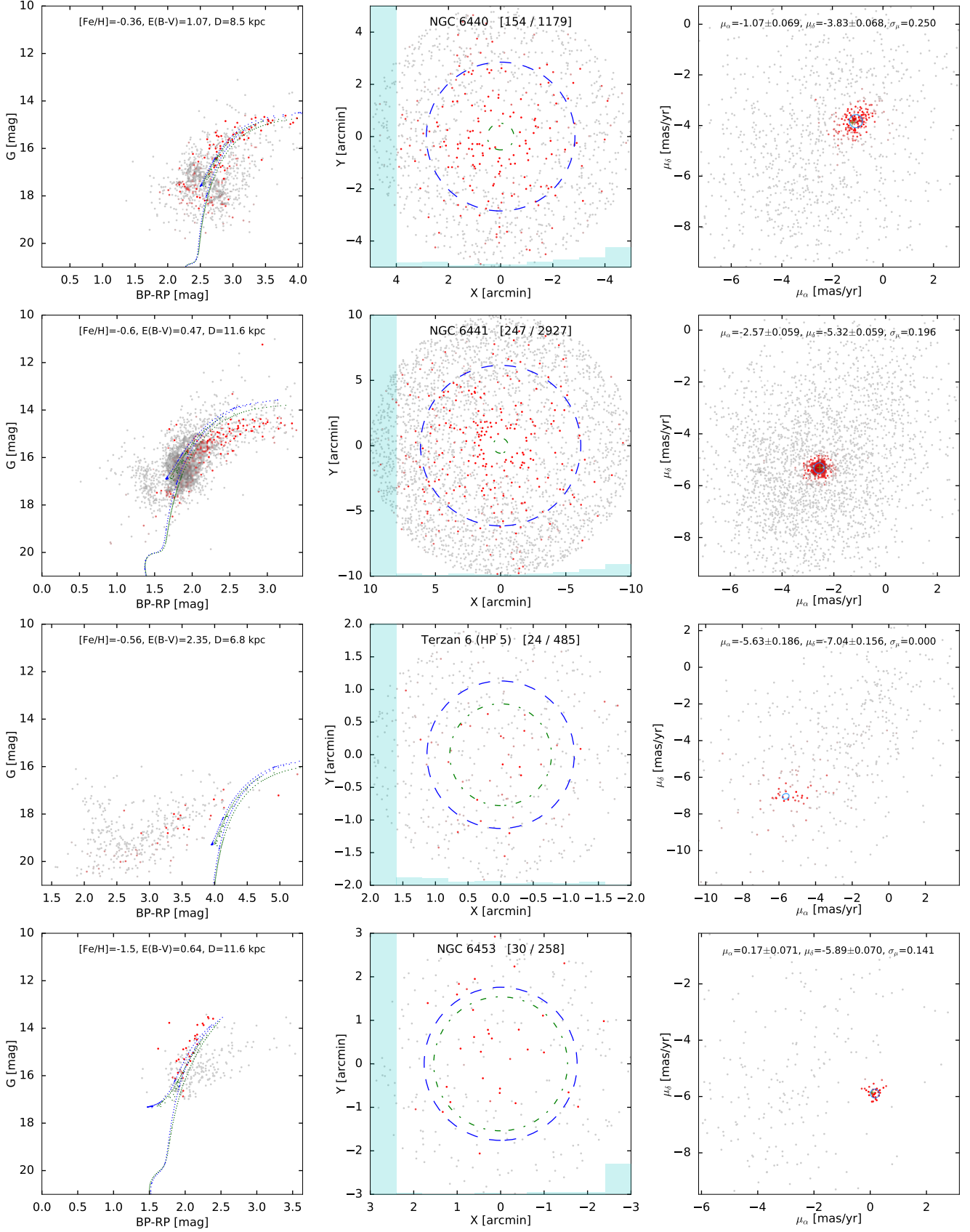


Figure C1 – continued

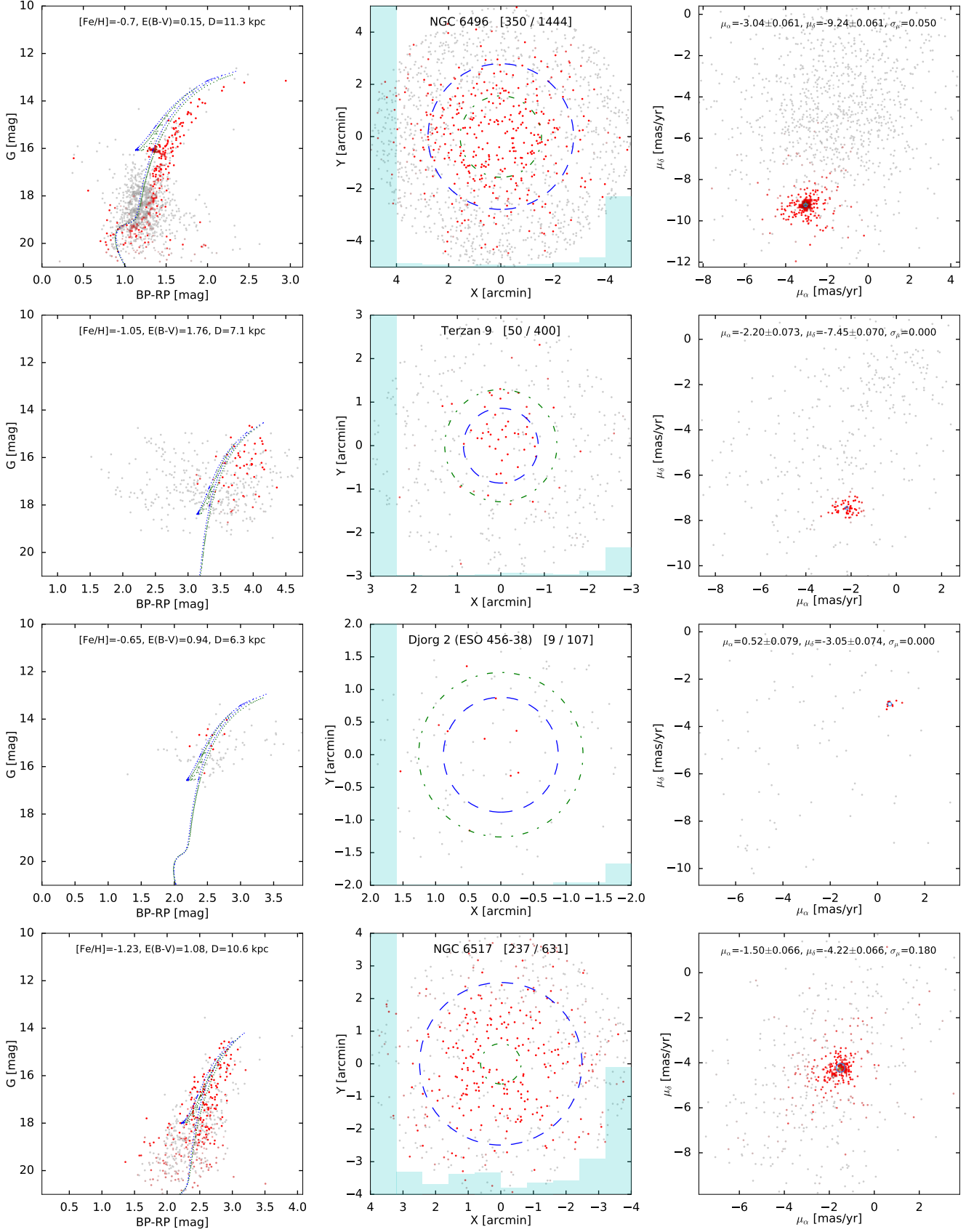


Figure C1 – *continued*

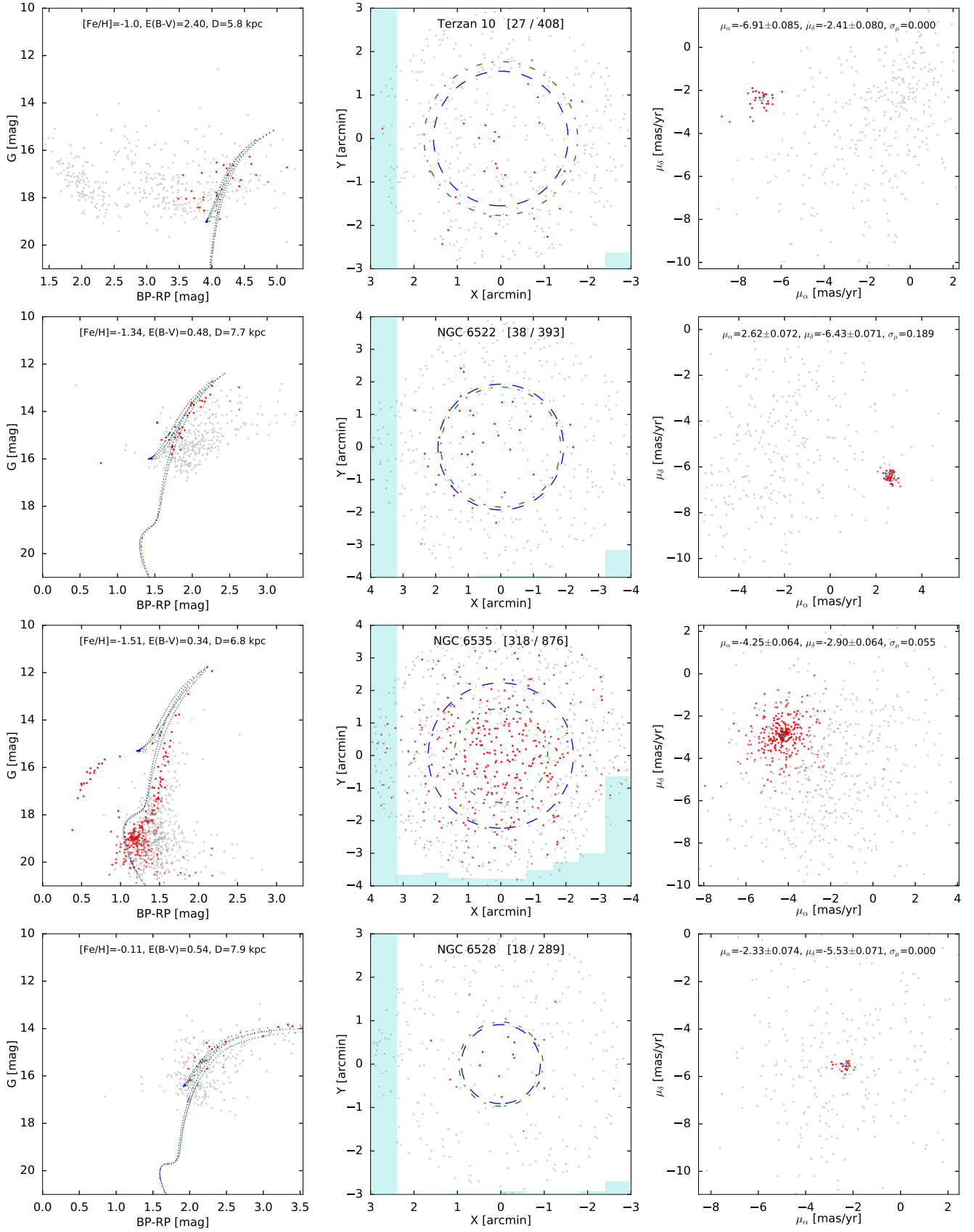


Figure C1 – continued

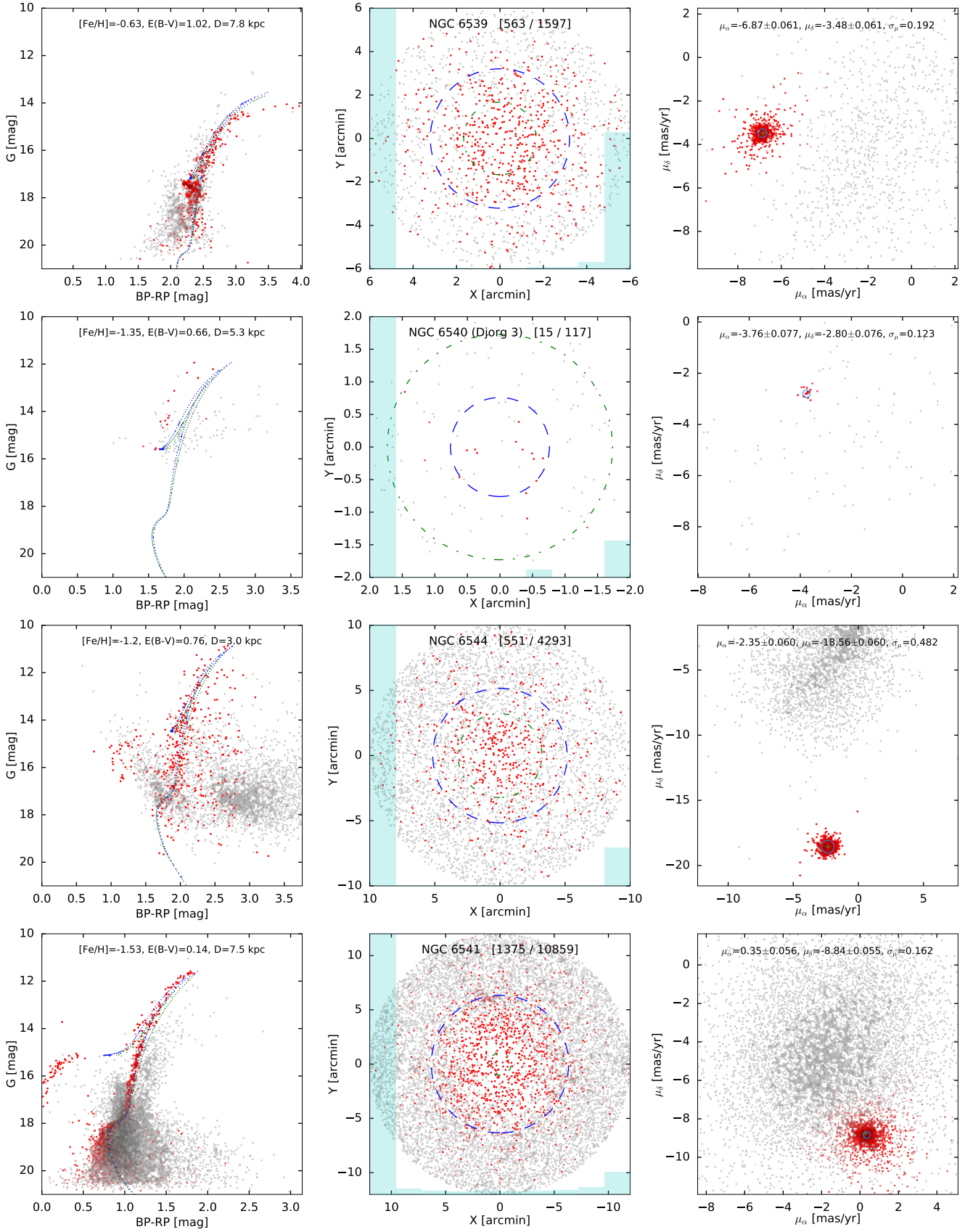


Figure C1 – *continued*

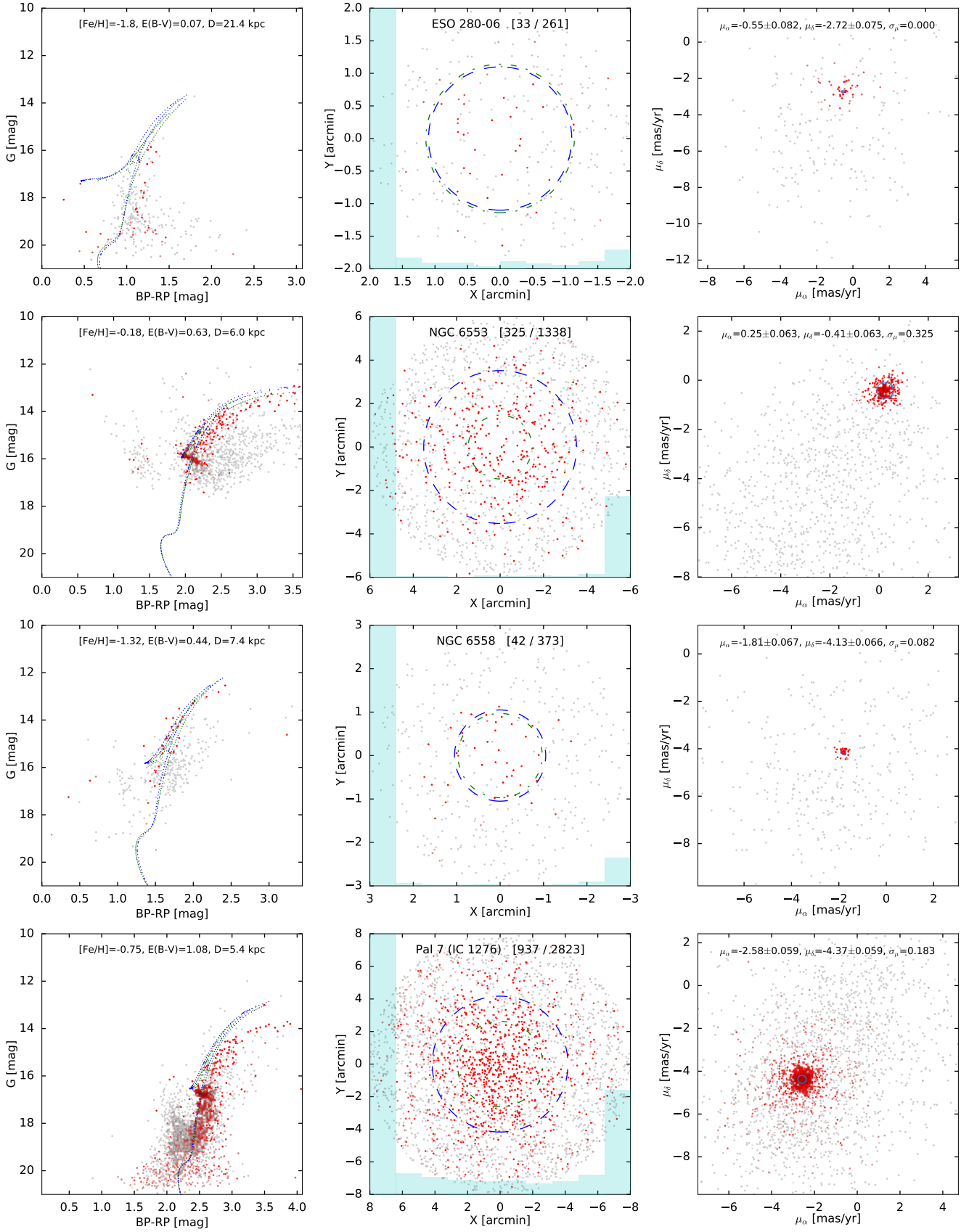


Figure C1 – continued

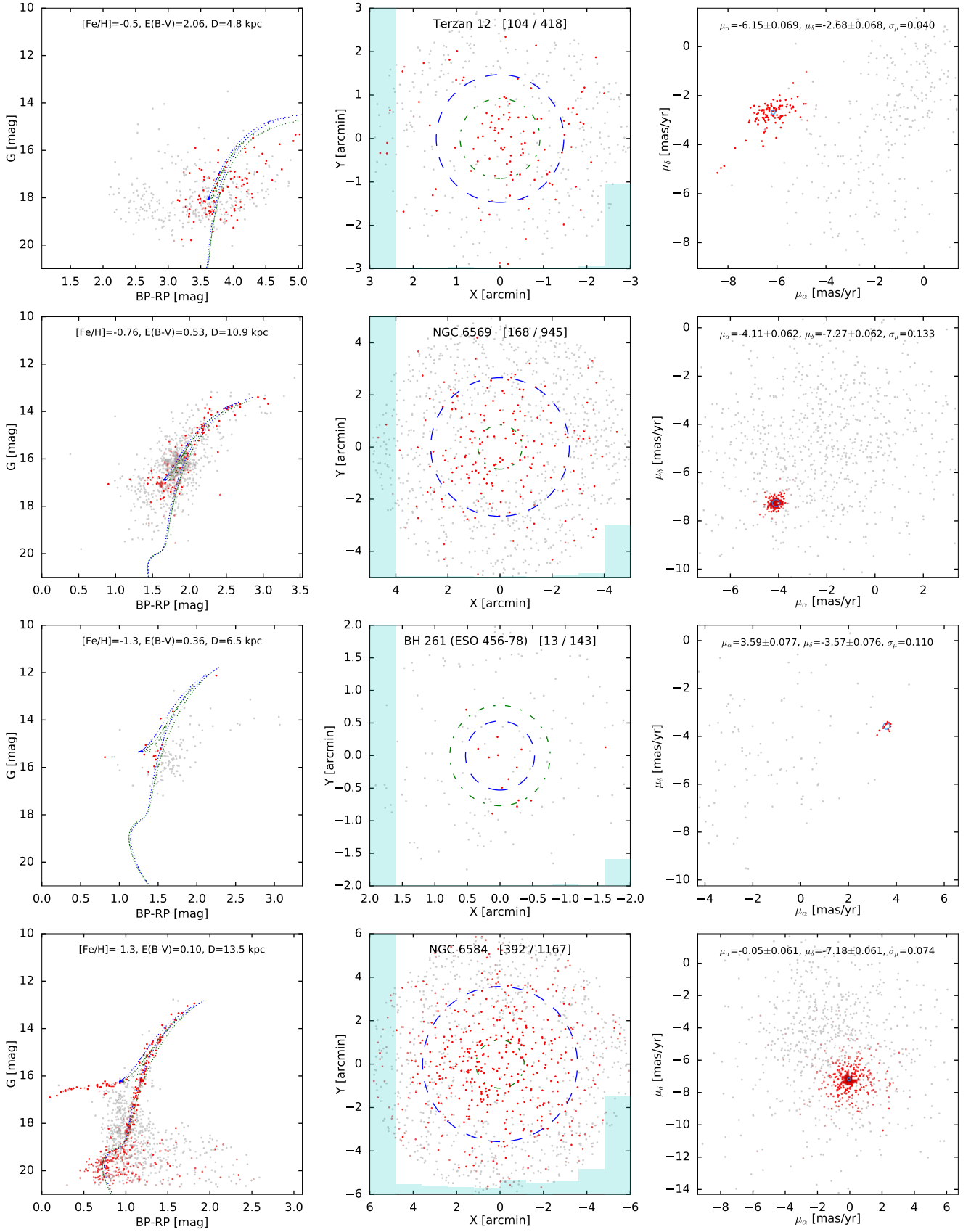


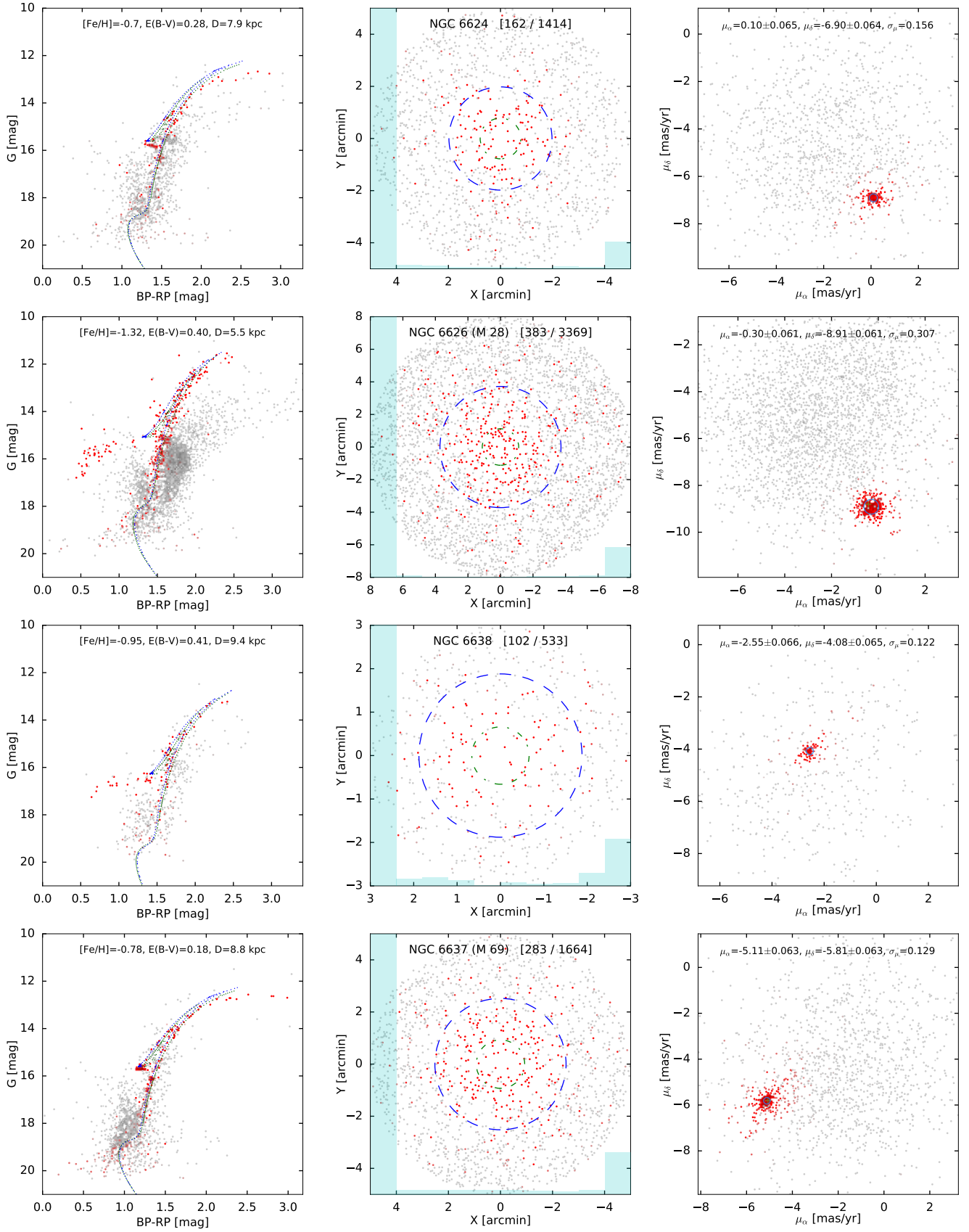
Figure C1 – *continued*

Figure C1 – continued

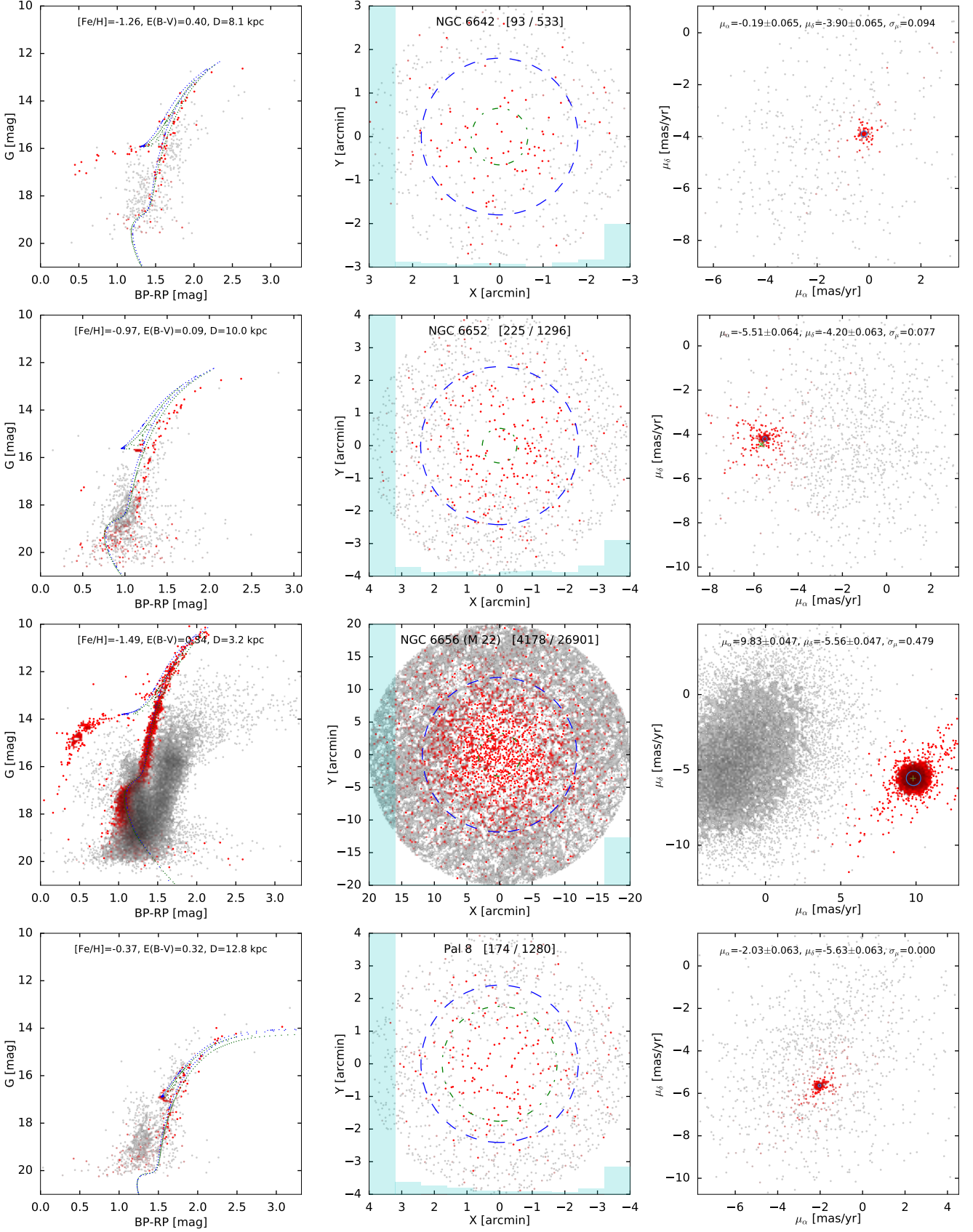


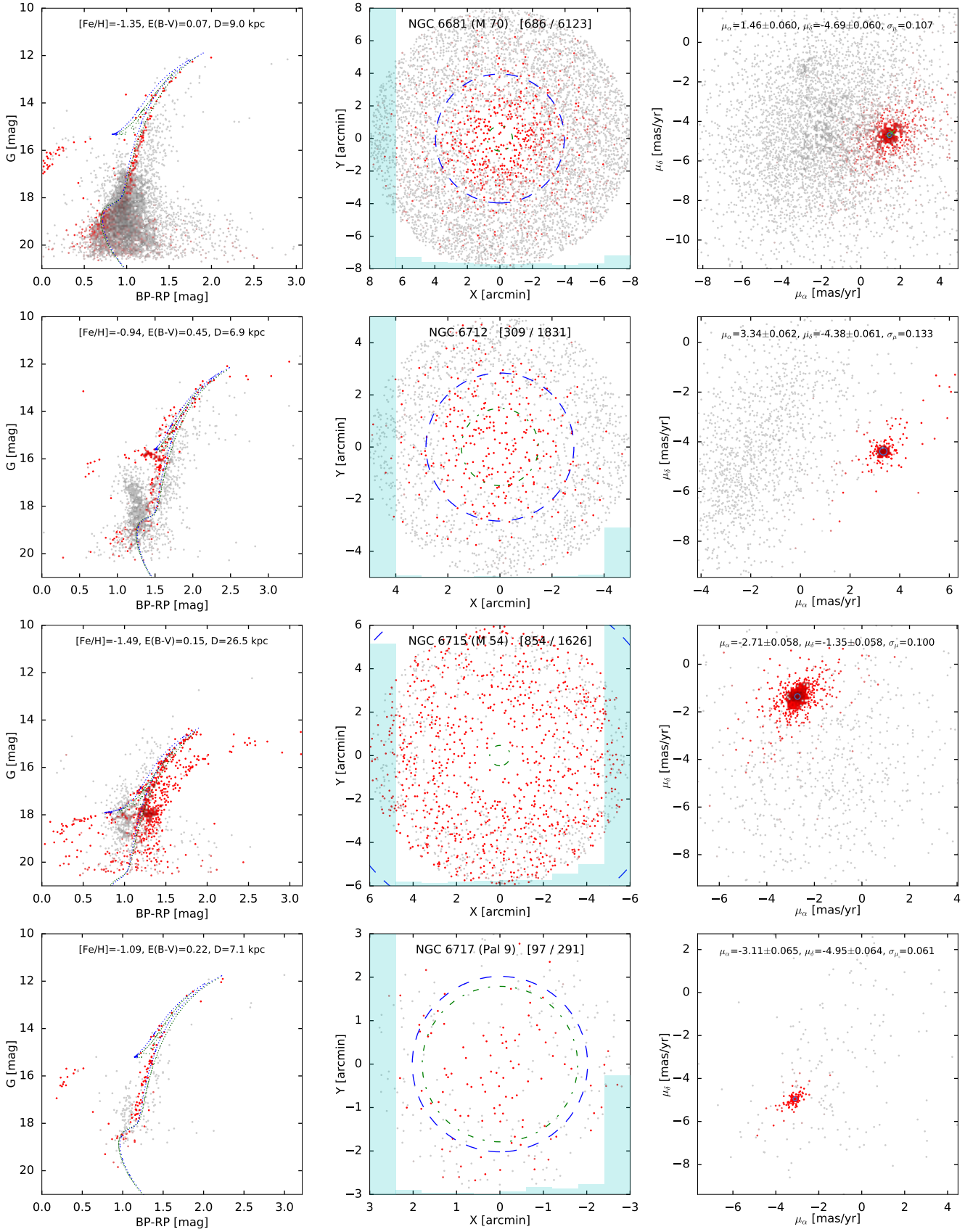
Figure C1 – *continued*

Figure C1 – continued

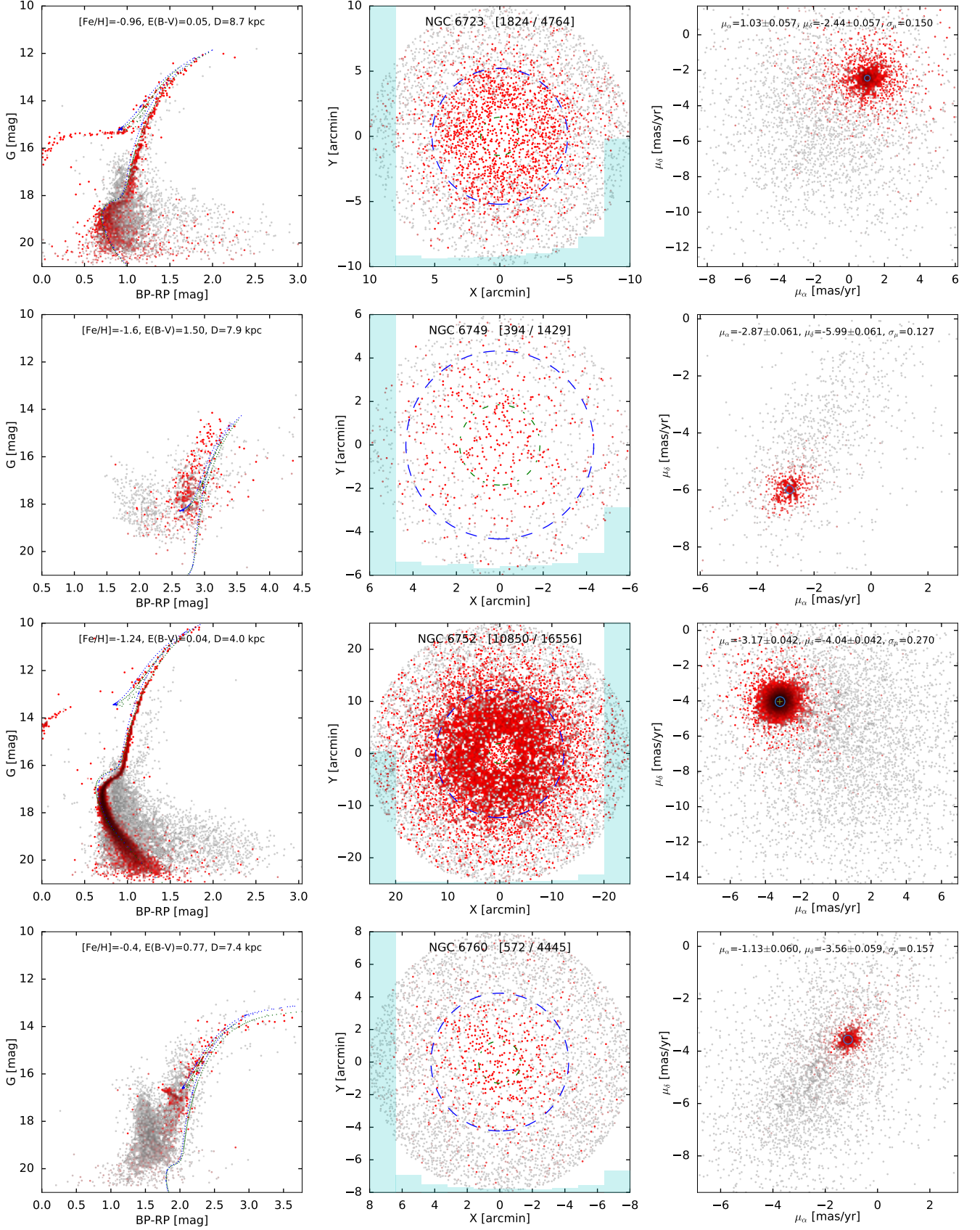


Figure C1 – *continued*

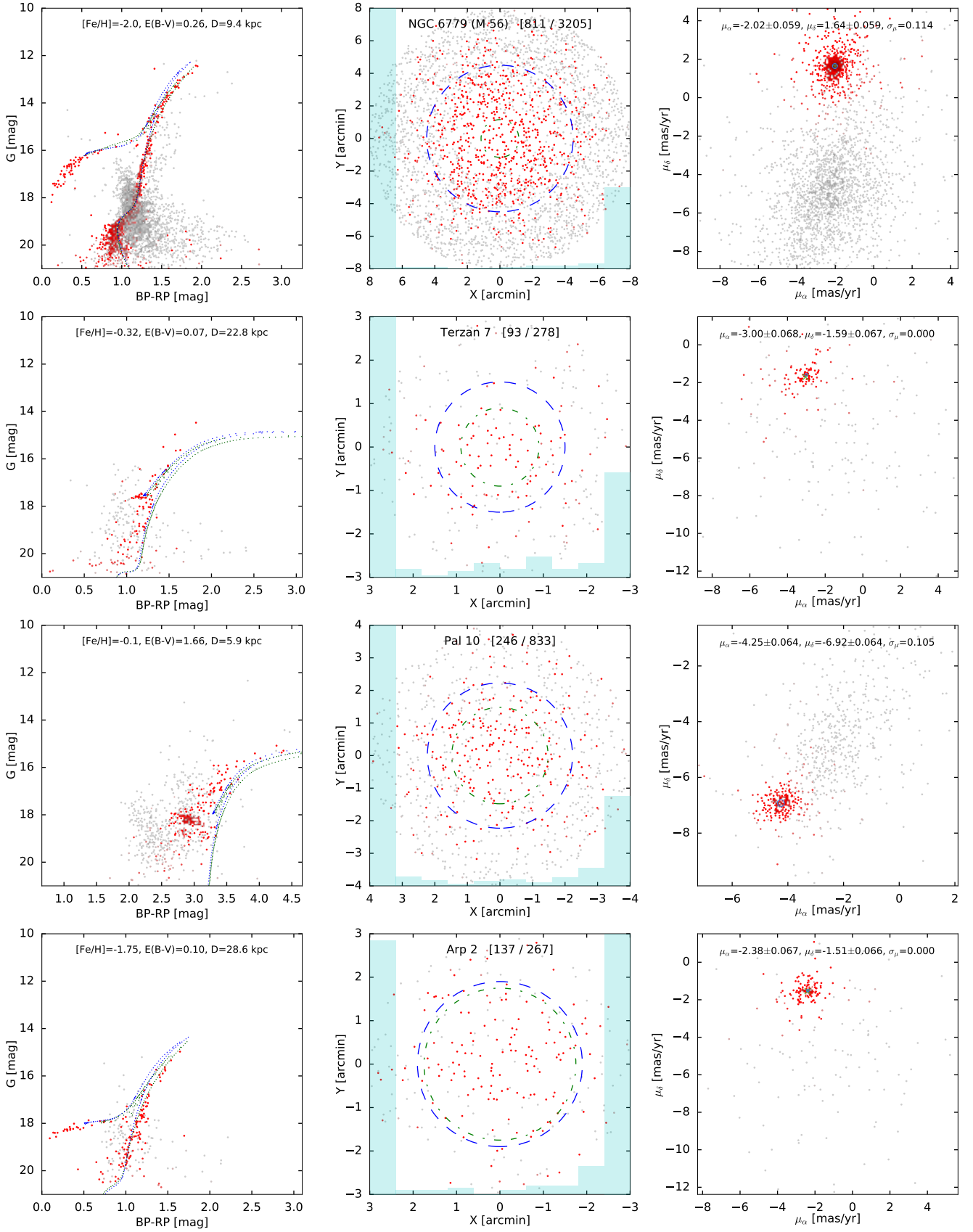


Figure C1 – continued

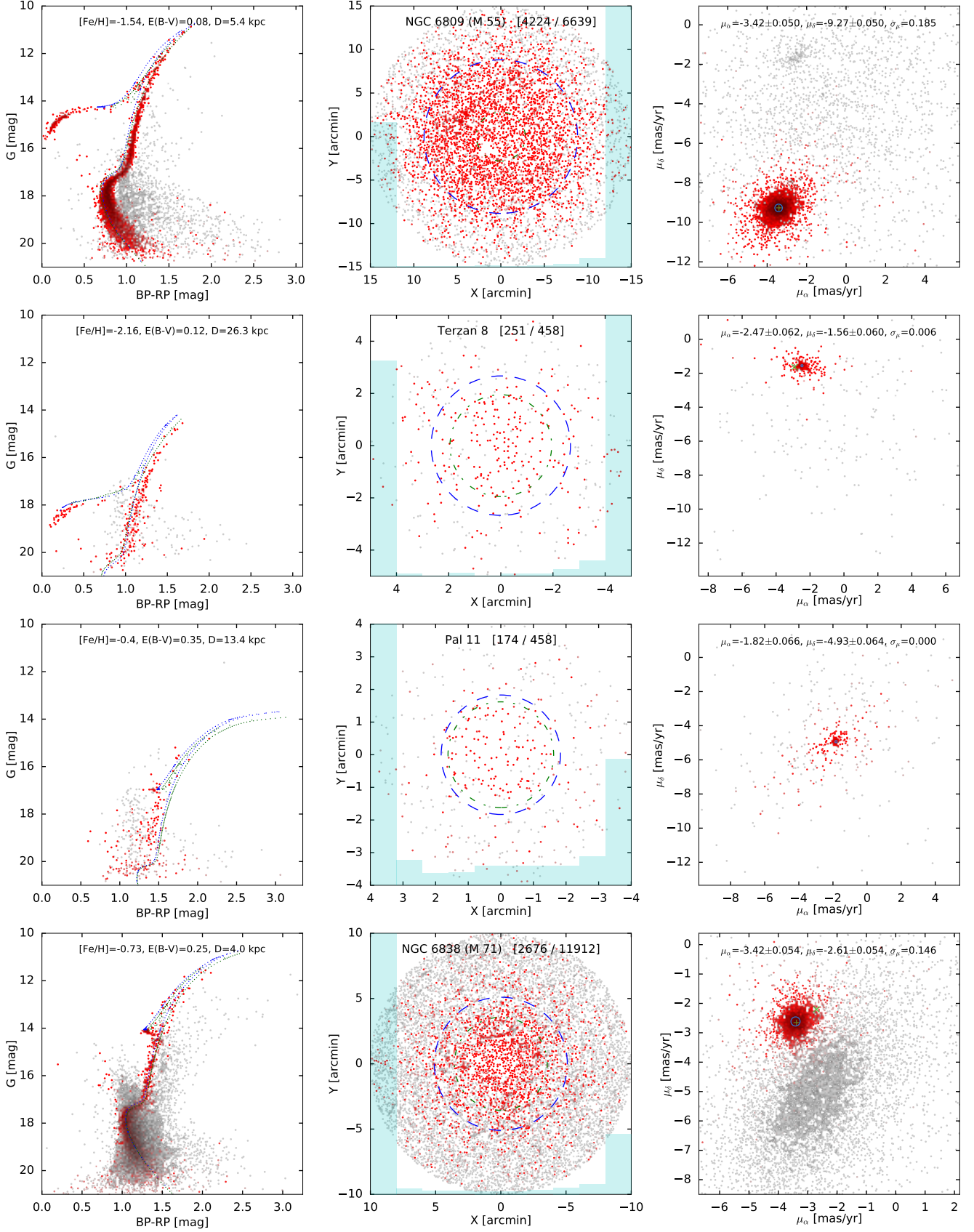


Figure C1 – *continued*

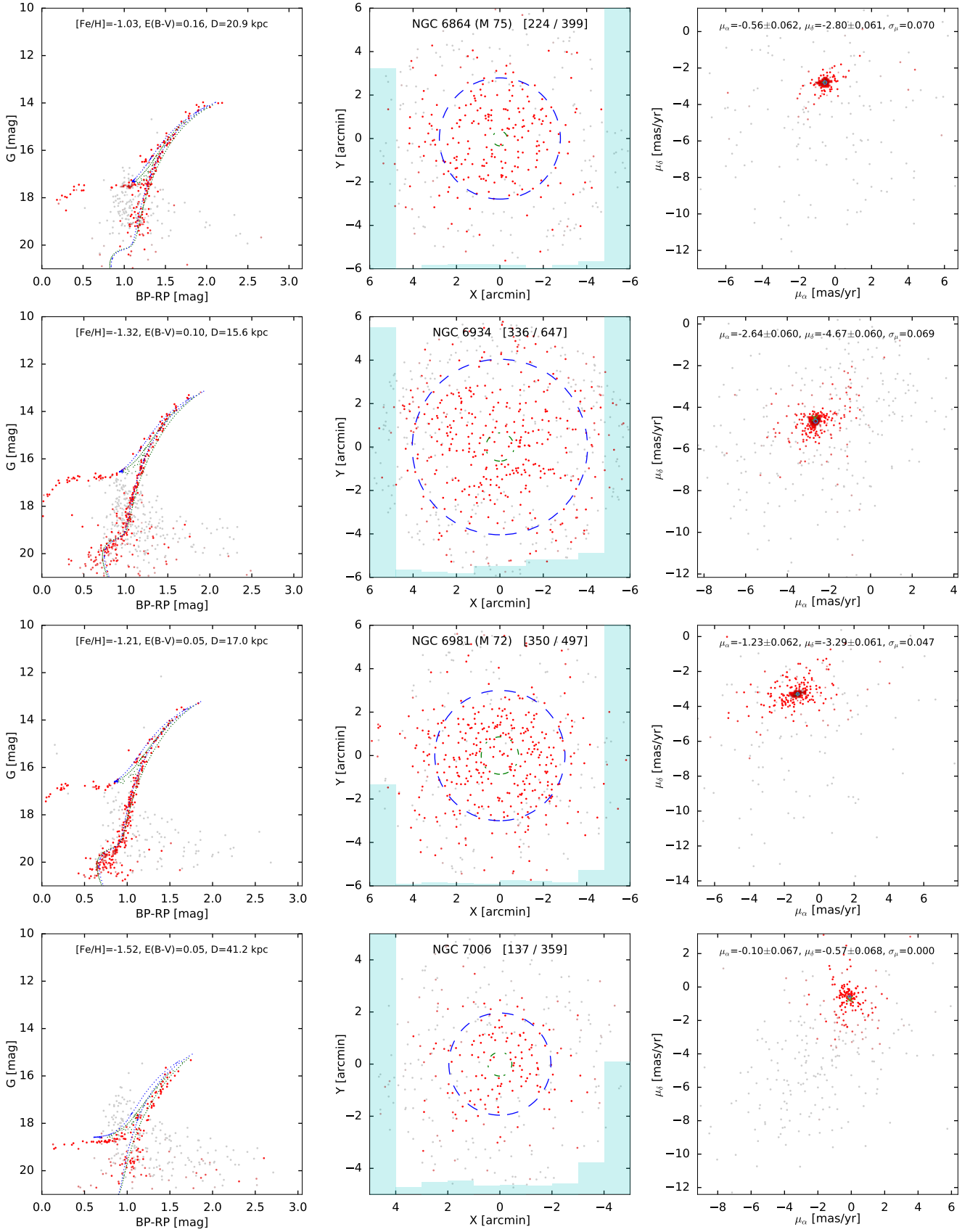


Figure C1 – continued

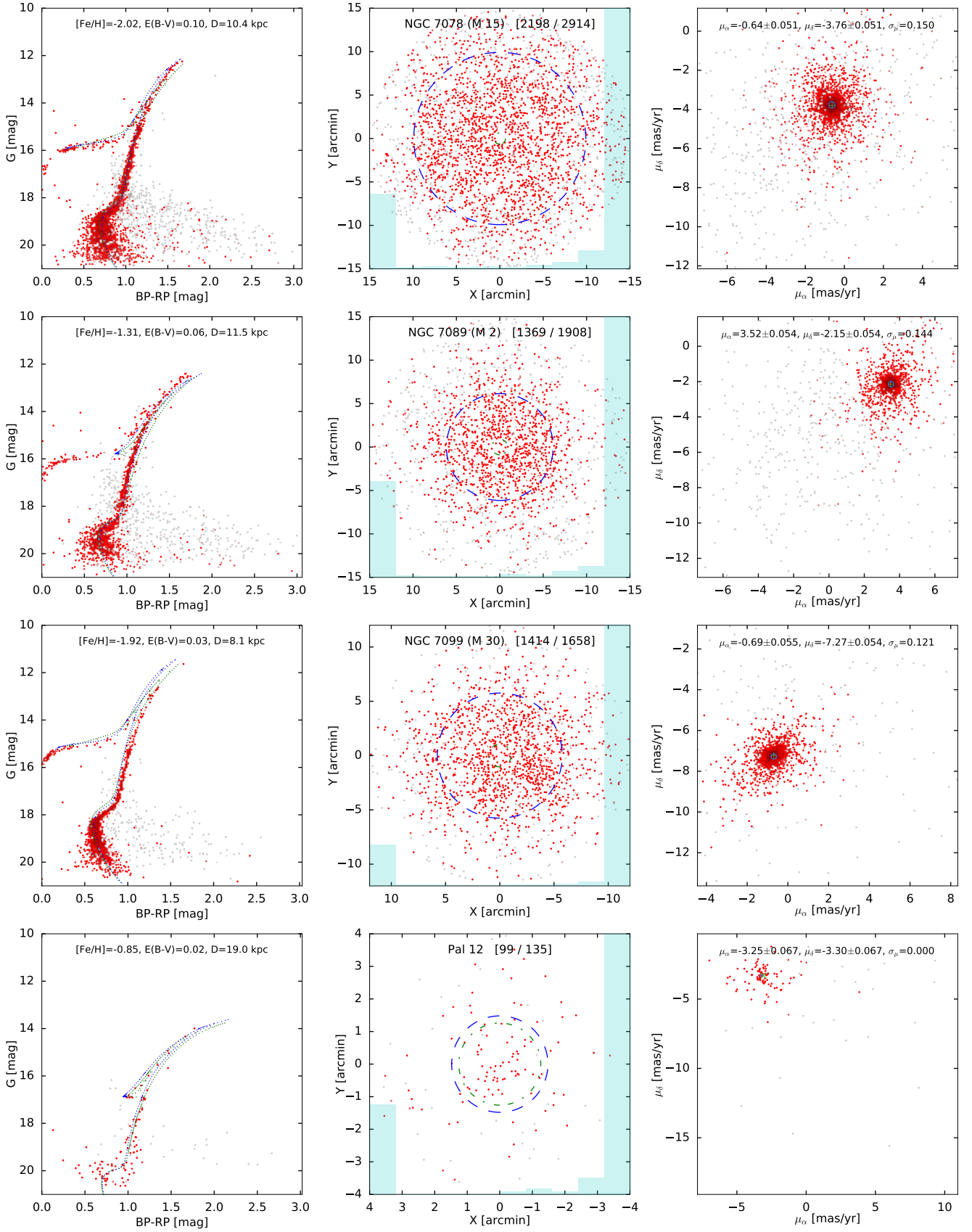


Figure C1 – *continued*